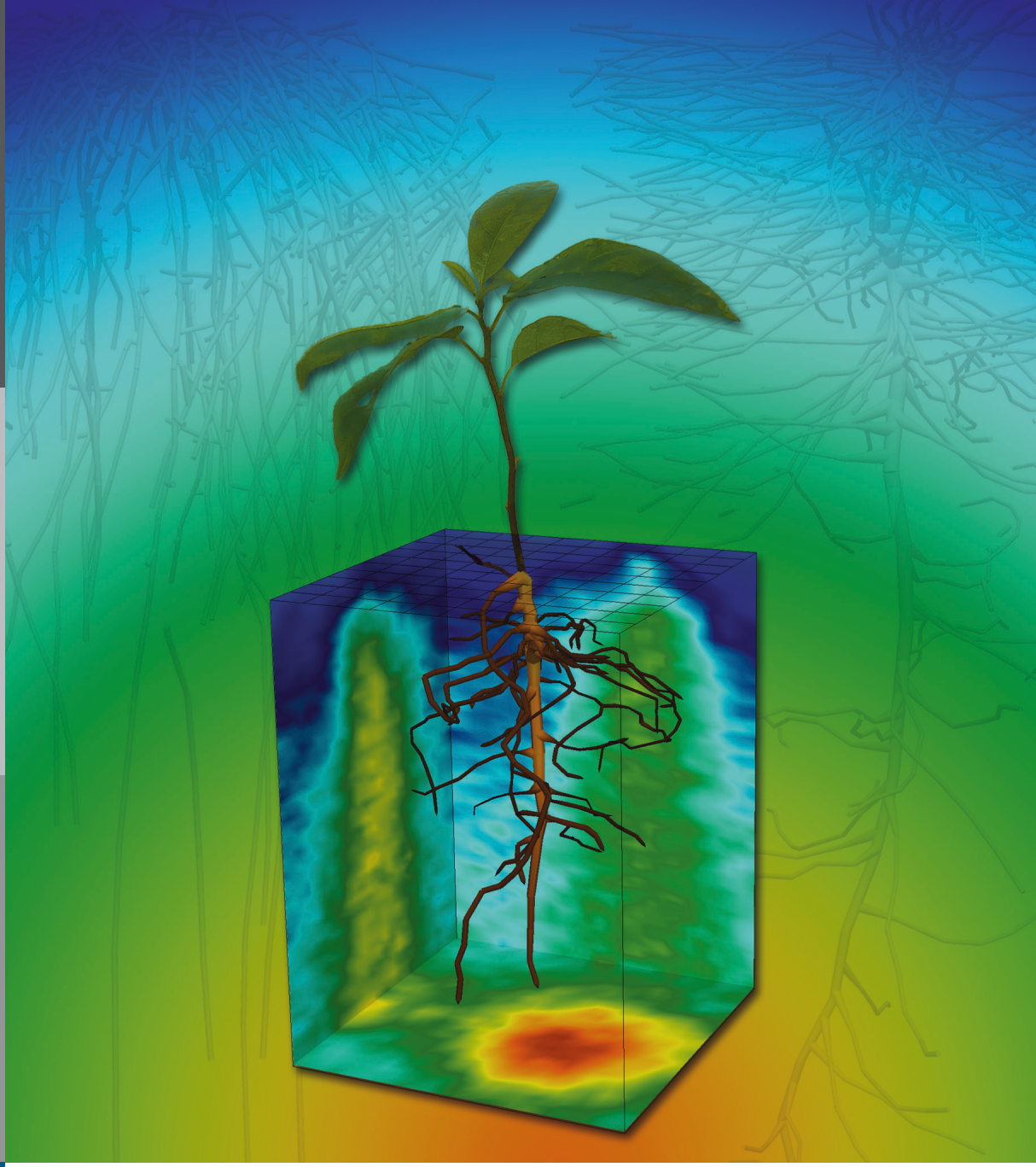

Three-dimensional Solute Transport Modeling in Coupled Soil and Plant Root Systems

Natalie Schröder

Member of the Helmholtz Association

JÜLICH
FORSCHUNGSZENTRUM

Schriften des Forschungszentrums Jülich

IAS Series Volume 22

Forschungszentrum Jülich GmbH
Institute for Advanced Simulation (IAS)
Jülich Supercomputing Centre (JSC)

Three-dimensional Solute Transport Modeling in Coupled Soil and Plant Root Systems

Natalie Schröder

Schriften des Forschungszentrums Jülich

IAS Series Volume 22

ISSN 1868-8489 ISBN 978-3-89336-923-2

Bibliographic information published by the Deutsche Nationalbibliothek.
The Deutsche Nationalbibliothek lists this publication in the Deutsche
Nationalbibliografie; detailed bibliographic data are available in the
Internet at http://dnb.d-nb.de.

Publisher and Distributor:	Forschungszentrum Jülich GmbH Zentralbibliothek 52425 Jülich Phone +49 (0) 24 61 61-53 68 · Fax +49 (0) 24 61 61-61 03 e-mail: zb-publikation@fz-juelich.de Internet: http://www.fz-juelich.de/zb
Cover Design:	Jülich Supercomputing Centre, Forschungszentrum Jülich GmbH
Printer:	Grafische Medien, Forschungszentrum Jülich GmbH
Copyright:	Forschungszentrum Jülich 2013

Schriften des Forschungszentrums Jülich
IAS Series Volume 22

ISSN 1868-8489
ISBN 978-3-89336-923-2

Persistent Identifier: urn:nbn:de:0001-2013112209
Resolving URL: http://www.persistent-identifier.de/?link=610

Thesis examining board:

Supervisor:	Prof. Mathieu Javaux (UCL, Belgium)
President of the jury:	Prof. Pierre Defourny (UCL, Belgium)
Members of the jury:	Prof. Jan Diels (KULeuven, Belgium)
	Prof. Emmanuel Hanert (UCL, Belgium)
	Prof. Naftali Lazarovitch (Ben Gurion University, Israel)
	Prof. Marnik Vanclooster (UCL, Belgium)
	Prof. Harry Vereecken (Forschungszentrum Jülich GmbH, Germany)

Summary

Many environmental and agricultural challenges rely on the proper understanding of water flow and solute transport in soils, for example the carbon cycle, crop growth, irrigation scheduling or fate of pollutants in subsoil. Current modeling approaches typically simulate plant uptake via empirical approaches, which neglect the three-dimensional (3D) root architecture. Yet, nowadays 3D soil-root water and solute models on plant-scale exist, which can be used for assessing the impact of root architecture and root and soil hydraulic resistances on the root uptake pattern and solute transport and water flow in soil.

In this thesis, we used a numerical model, which offers the possibility to describe soil and root interaction processes in a mechanistic manner avoiding empirical descriptions of root water uptake as a function of averaged water potential and root length density. Water flow is simulated along water potential gradients in the soil-root continuum and the model accounts for solute movement and root solute uptake. Solute movement in soils is modeled with a particle tracking algorithm. With this model, three research questions are investigated.

The first study investigates how root water uptake affects the velocity field, and thus the dispersivity length. The solute breakthrough curves from the three-dimensional results and different simulation setups were fitted with an equivalent one-dimensional flow and transport model. The obtained results of the apparent soil dispersivities show the effect of the plant roots on solute movement, and illustrate the relevance of small scale 3D water and solute fluxes, induced by root water and nutrient uptake.

Second, we show how local matric and osmotic potentials affect root water uptake. We analyze the difference between upscaled time and root-zone integrated water potentials, as often measured in experimental studies, and local water potentials at the root-soil interface. In addition, we demonstrate the relation between the shape of local stress function and the global (time-integrated) plant stress response to salinity.

The last part explores how water uptake could be deduced from tracer concentration distribution monitored in a soil-plant system by magnetic resonance imaging (MRI). We show the effects of root system architecture, fine roots, and root conductance on solute and compare numerical and measured data. This shows the capabilities and limitations of both, the model prediction and the MRI measurement methodology. Furthermore, it points out the extensive effect of root architecture and its conductance parameters on solute spreading.

Contents

List of Figures

List of Tables

List of Symbols

A	active root solute uptake	$[d^{-1}]$
A_r	root outer surface	$[cm^2]$
A_x	root xylem cross sectional area	$[cm^2]$
D_w	molecular diffusion coefficient (free water)	$[cm^2\ d^{-1}]$
H	total water head	[cm]
H_{collar}	water head at root collar	[cm]
H_{collar}^{crit}	critical water head at root collar	[cm]
H_s	root-soil interface water head	[cm]
J_r	radial soil-root water flow	$[cm^3\ d^{-1}]$
J_w	soil water flow	$[cm\ d^{-1}]$
J_x	axial root xylem water flow	$[cm^3\ d^{-1}]$
K_r^*	radial root conductivity	$[cm\ d^{-1}\ cm^{-1}]$
K_x^*	xylem root conductivity	$[cm^2\ d^{-1}\ cm^{-1}]$
K_s	saturated soil hydraulic conductivity	$[cm\ d^{-1}]$
K_x	axial root conductance	$[cm^3\ d^{-1}]$
K_{eff}	effective root conductance	$[cm^3\ d^{-1}\ cm^{-1}]$
K_m	Michaelis-Menten constant	$[\mu mol\ cm^{-3}]$
K_{rs}	conductance of root system	$[cm^3\ d^{-1}\ cm^{-1}]$

R_d	root surface density	[cm^2 cm^{-3}]
S	water sink term	[T^{-1}]
S'	solute sink term	[d^{-1}]
SSF	standard sink fraction	[−]
T_s	total root surface	[cm^2]
T_{act}	actual transpiration rate	[cm^3 d^{-1}]
T_{pot}	potential transpiration rate	[cm^3 d^{-1}]
V	volume	[cm^3]
V_{max}	maximum solute uptake rate	[μmol cm^{-2}d^{-1}]
X	coordinate vector	[cm]
Y_{act}	actual yield	[g m^{-2}]
Y_{pot}	potential yield	[g m^{-2}]
Θ	normalized water content	[−]
α	transpiration reduction function	[−]
β	transformation parameter between c and h_o	[μmol^{-1}]
ϵ	partition coefficient	[−]
λ_L	longitudinal dispersivity length	[cm]
λ_T	transverse dispersivity length	[cm]
λ_{app}	apparent dispersivity length	[cm]
$\mathbf{B}$	dispersion displacement matrix	[L^2 T^{-1}]
$\mathbf{D}$	dispersion coefficient tensor	[cm^2 d^{-1}]
$\mathbf{D}_h$	hydrodynamic dispersion coefficient tensor	[L^2 T^{-1} L^{-2}]
$\mathbf{D}_m$	molecular diffusion tensor	[L^2 T^{-1} L^{-2}]

$\mathbf{I}$	identity matrix	[–]
$\mathbf{J}_c$	advective solute flux	[M T^{-1} L^{-2}]
$\mathbf{J}_d$	diffusive solute flux	[M T^{-1} L^{-2}]
$\mathbf{J}_h$	dispersion solute flux	[M T^{-1} L^{-2}]
$\mathbf{J}_s$	total solute flux	[M T^{-1} L^{-2}]
$\mathbf{K}$	soil hydraulic conductivity tensor	[cm d^{-1}]
σ	membrane reflection coefficient	[–]
σ_{rs}	root surface distribution	[cm^2]
τ	tortuosity factor	[–]
θ	volumetric water content	[cm^3 cm^{-3}]
θ_r	residual volumetric water content	[cm^3 cm^{-3}]
θ_s	saturated volumetric water content	[cm^3 cm^{-3}]
ξ	vector of three random numbers	[–]
a	Mualem-van Genuchten shape parameter	[cm^{-1}]
c	solute concentration	[μmol cm^{-3}]
c_0	initial solute concentration (boundary)	[μmol cm^{-3}]
c_f	flux concentration	[μmol cm^3]
c_r	resident concentration	[μmol cm^3]
d_{ij}	Kronecker delta function	[–]
f	first-order rate coefficient	[cm d^{-1}]
h	pressure head	[cm]
h_{int}	pressure head at root-soil interface	[cm]
h_{leaf}	leaf water head	[cm]

h_o	osmotic head	[cm]
h_{xylem}	pressure head in root xylem	[cm]
l	pore connectivity parameter	[−]
l_{seg}	root segment length	[cm]
m_c	solute mass	[μmol]
n	Mualem-van Genuchten shape parameter	[−]
q	darcy flow	[L T^{-1}]
t	time	[d]
u	pore water velocity	[cm d^{-1}]
z	vertical coordinate	[cm]
$< c >$	averaged concentration at a certain depth	[μmol cm^{-3}]
BBC	bottom boundary condition	
BC	boundary condition	
BTC	breakthrough curves	
CDE	convection-dispersion equation	
CVvz	coefficient of variation of vertical velocity component	
FE	finite element	
MvG	Mualem-van Genuchten	
RLD	root length density	
RSD	root surface density	
RWPT	random walk particle tracking	
TBC	top boundary condition	

Chapter 1

General introduction

Groundwater comprises about 96 % of all liquid fresh water on earth [Shiklomanov, 1993] and thus is the major source for drinking water in most areas of the world. This leads to a close observation of the groundwater quality, and thus groundwater contamination. Nitrate, various pesticides, and heavy metals from industrial sites or from agriculture reach the groundwater through the vadose zone and may affect human health. Therefore, it is crucial to understand solute movement and interaction of water and solutes in saturated and unsaturated soil by investigating and quantifying physical, chemical, and biological processes in the subsurface.

Solutes move through the soil mainly with the water flow or by concentration gradients. In addition, other processes might affect solute fate as adsorption to soil particles, precipitation, uptake by living organisms, etc. [Rausch et al., 2005]. Plants may have a significant impact on solute fate, in a direct or indirect way. The presence of plants impacts solute fate not only because of the solute uptake itself (solute sink), but also by the effect by plants on the water velocity field via water extraction (water sink). Water uptake by plant roots decreases the water content in vegetated soil layers and disturbs the water velocity field around roots. For this reason, the vertical component of the velocity is decreased compared to bare soils subject to the same conditions (retardation).

In addition water uptake affects the variability of the vertical and horizontal components of the velocity field, and thus affects solute dispersion. Furthermore, when considering the effect of root on solute transport, plant uptake of solute needs to be considered. Whether or not solute is taken up by plants and to which extent, will have an impact on the distribution of the solute mass in the heterogeneous flow field. This can have important consequences for transport processes in heterogeneous flow fields [Vanderborght et al., 1998, 2006], and therefore on the transport process.

Understanding solute processes in the vadose zone is also crucial to assess the effect of solutes on plants. Since the water demand of plants is mainly dependent on atmospheric conditions, irrigation of agricultural fields in semi-arid and arid areas of the world is often required. Worldwide, 80% of fresh water is used for irrigation, which leads to

problems for managing water and salt balances [Green et al., 2006]. Of all irrigated lands, approximately 20–50% are salt-affected which cause losses in crop production. This wastage is estimated to be significant and increasing with time, but is difficult to assess [Pitman and Läuchli, 2004]. For this reason, investigating how salts impact plant water status is essential. When salts are excluded by roots, they accumulate around plant roots and cause high osmotic potentials in the root zone [Hamza and Aylmore, 1992]. In this case, these high osmotic potentials cannot be neglected, because the root water uptake depends on the local total water potential gradient that includes the osmotic component. The plants suffer from salt stress and, to avoid damage inside the plant, respond by reducing their transpiration rate, and thus their yield [de Wit, 1958].

Root water uptake is a passive mechanism driven by water potential gradients from the soil around the roots to the root xylem [Steudle, 2000]. The magnitude and location of the uptake depends locally, among others, on the root architecture topology, the precise location of roots inside the soil, the soil water distribution, regulation of transpiration rates by the plant, solute distribution in the soil, and vapor pressure deficit in the atmosphere [Feddes and Raats, 2004]. The local processes at the root-soil interface are of fundamental importance for understanding and predicting plant-soil interactions.

Unfortunately, most of our current experimental devices do not allow an accurate measurement of soil and root variables locally, which make predictions very difficult to realize. There is thus a scale gap between local processes driving the exchanges between plant and soil systems and the scale at which we observe these phenomena. Effective modeling approaches have thus often been used at the plant scale.

Recently, fully coupled root architecture transfer models were developed [Javaux et al., 2011], where the water flow equation is solved in a soil matrix as well as in a root system architecture, allowing a sound investigation of the impact of local soil concentration and pressure head on the apparent plant behavior. Using the model of Javaux et al. [2008] in combination with extended developments describing solute transport and root solute uptake, this thesis investigates soil-plant interactions considering water flow and solute transport on plant scale.

1.1 Objectives

The objective of this thesis is to investigate how the apparent plant-soil system behavior depends on local scale processes occurring in plant, in soil and at their interface by using a detailed three-dimensional (3D) physically based model. Using this model, three questions will particularly be addressed:

1. How does root water uptake affects the velocity field, and thus the dispersion length?
2. How do local matric and osmotic potentials affects root water uptake?
3. How can water uptake be deduced from tracer concentration distribution monitored in a soil-plant system?

To this end, a model at the plant scale, which describes local bio-physical processes in and between plant roots and soil matrix is needed. The model of Javaux et al. [2008] was therefore extended in order to consider solute movement in the soil and root solute uptake. A solute module was added, which simulates solute transport in soil in combination with different root solute uptake mechanisms. This model offers the possibility to describe soil and root interaction processes in a more mechanistic manner avoiding empirical descriptions of root water uptake as a function of e.g. bulk water potential or root length density. In addition, taking osmotic head gradients into account during root water uptake, a feedback coupling from the solute to the water module was added.

1.2 Thesis outline

In this thesis, first a comprehensive description of the physical, mathematical and computational aspects of the used models are given in **Chapter 2**. Here, soil and root water flow, solute transport, and root water and solute uptake are defined and their numerical implementation is explained in detail. Based on these principles, the different projects are presented in the three following Chapters 3–5, corresponding to published or submitted publications to international peer-reviewed journals. In more detail:

Chapter 3 explores the effect of root architecture, root water and solute uptake mechanisms, and transpiration rates on solute transport in soil. Using the three-dimensional (3D) model, two different root architectures were compared by several simulation runs. The simulation setups started with basic boundary and initial conditions and solute uptake type or transpiration rates were modified. Afterwards, parameters, initial and boundary conditions were adapted to describe more realistic behaviors. The effect of water and nutrient uptake on the apparent dispersivity length were analyzed by fitting the solute breakthrough curves (BTC). These were calculated from different simulation setups, and fitted with an equivalent one-dimensional (1D) flow and transport model. The obtained results of the apparent soil dispersivities show the effect of the plant roots on solute movement, and illustrate the relevance of small scale 3D water and solute fluxes, induced by root water and nutrient uptake.

Chapter 4 investigates the impact of salinity on root water uptake. There, the solute concentration in the soil were transformed into an osmotic head, and considered in the potential difference at the root surface that influenced the radial water flow into the root. In a first simulation setup, experimental data from Hamza and Aylmore [1992] were compared with simulation results in order to validate the model. Hereafter, simulation setups with different complexity were run to investigate the plant response to solute accumulation around the roots leading to plant stress. The difference between upscaled time and root zone integrated water potentials, as often measured in experimental studies, and water potentials at the soil-root interface were analyzed. In addition, difference between the global (time-integrated) and the local stress respond, which is used in numerical models, was investigated.

Chapter 5 compares measured data from a tracer experiment with numerical solute simulations. For 9 days, tracer movement in a cylindrical column containing lupine plant, was monitored by magnetic resonance imaging (MRI). The obtained data provide 3D solute distribution patterns and root architecture data. To investigate the effect of root system architecture, fine roots, and root conductance on solute movement, several simulation were run comparing two root systems with a variety of hydraulic root properties. While the first root system were reconstructed from the measured MRI data and shows only the major axes and branches of the lupine root system, the second root system contains additional fine roots, which were added artificially using a root growth model. Comparing averaged one-dimensional as well as spatial three-dimensional solute distributions of the measured and different simulated data does not only show the capabilities and limitations of both, the model prediction and the MRI measurement methodology, but also points out the extensive effect of root architecture and its conductance parameters on solute spreading.

Each of theses chapters deals with its own objectives and thus has its own introduction, theory and methodology. In order to provide the needed fundamentals for each chapter individually, duplication is unavoidable. Finally **Chapter 6** presents the general conclusions of the Chapters 3–5 and perspectives for future research are given.

Chapter 2

Modeling soil-root interactions

In this chapter, descriptions of the fundamental physics used in the numerical models are given. To this end, the definitions of water flow and solute transport in soils, including root water and solute uptake by plant roots, and their numerical implementation are introduced and discussed.

2.1 Transient soil water flow

2.1.1 Water potentials in soil

The physicochemical state of soil water is characterized in terms of its free energy per unit volume, mass, or weight, and is called *soil water potential*. For the soil water potential on volume basis the symbol ψ [P] is typically used, while soil water potential on a weight basis is referred to as *total soil water head* H [L]. The total soil water head can be divided into components that describe the different force fields acting on the soil water. In a rigid soil where the gaseous phase moves freely, the total water head is given by

$$H = h + z + h_o, \tag{2.1}$$

where h [L] is the *pressure head*, z [L] the *gravitational head*, and h_o [L] the *osmotic head*. The gravitational component depends on relative elevation and defined negative, while the pressure component on capillary and adsorptive forces, causing negative pressure. The osmotic component occurs due to solute concentrations in the soil water, which affects the thermodynamic properties of water and lowers its potential energy. Note, that osmotic potential gradients only drive liquid water flow when there is a membrane that restricts solute transport compared to the movement of water molecules. This might be the case for flow across plant cell membranes or through thin water films in porous media in which the mobility of hydrated ions is constrained [Nassar and Horton,

1997]. In this work, water flow in the soil due to gradients in osmotic potential in the soil is neglected. Water flow is driven by differences in water potentials, where water moves from higher to lower potential.

2.1.2 Soil hydraulic properties

Soil is a porous medium consisting of three phases: solid, liquid (mainly water) and gaseous. If the pore space is completely filled with water, the soil is saturated and the water potential is larger than or equal to zero. When a soil is drying, the water leaves the larger pores first and later the smaller ones. The force necessary to empty a single pore is inversely proportional to its diameter.

The amount of water which is hold by a soil is described by the *volumetric water content* θ [L^3 L^{-3}], which defines the ratio of volume water to volume soil. The relationship between water content and matric potential is called the *soil-moisture retention curve*. In this study, the Mualem-van Genuchten parametrization of the retention curves is used [van Genuchten, 1980]:

$$\Theta = \left[\frac{1}{1-(ah)^n}\right]^m = \frac{\theta-\theta_r}{\theta_s-\theta_r} \tag{2.2}$$

with

$$m = 1 - \frac{1}{n}, \tag{2.3}$$

where $\Theta = \frac{\theta-\theta_r}{\theta_s-\theta_r}$ is the *normalized water content*, θ_r and θ_s are the *residual* and the *saturated water content*, defining the minimal and maximal wetness of the soil, and a and n are shape parameters. Note, that hysteresis effects of the $\theta - h$ relationship [e.g. Hillel, 2003] are no focus of this study and are neglected in this thesis.

2.1.3 Richards equation

Transient water flow in rigid porous media is commonly described by the Richards equation [Richards, 1931], which results from the continuity equation for non-steady flow and Darcy's law [Darcy, 1856]. The continuity equation expresses the mass conservation, which specifies the difference between water entering and leaving a certain system, added to a source or sink, and is equal to the change of water content in the same system:

$$\frac{\partial \theta}{\partial t} = -\nabla \cdot \mathbf{q} - S(x, y, z, t), \tag{2.4}$$

where θ [L^3 L^{-3}] is the *volumetric water content*, t [T] is *time*, S [T^{-1}] is the *water sink term* (negative S is a source), and $\mathbf{q}$ [L T^{-1}] the *water flux*. The water flux in the soil is driven by the hydraulic head gradient $\nabla(h + z)$ and defined by Darcy's law

$$\mathbf{q} = -\mathbf{K}(h)\nabla(h + z). \tag{2.5}$$

The proportionality factor $\mathbf{K}$ [L T^{-1}] is called the *hydraulic conductivity tensor* and characterizes the relation of the soil water head gradient to the water flux $\mathbf{q}$. The vertical coordinate z is defined as zero at the top boundary of the soil domain and negative below. Using the Mualem-van Genuchten parametrization [van Genuchten, 1980], the soil hydraulic conductivity is defined by

$$\mathbf{K}(h) = \mathbf{I} K_s \Theta^l \left[1 - \left(1 - \Theta^{1/m}\right)^m\right]^2, \tag{2.6}$$

where Θ is the normalized water content, $\mathbf{I}$ is the identity matrix, K_s [L T^{-1}] is the *saturated hydraulic conductivity* and l the *tortuosity* of flow pathways through the soil, commonly set to 0.5. The combination of the continuity equation and Darcy's law

$$\frac{\partial \theta}{\partial t} = \nabla \cdot [\mathbf{K}(h)\nabla(h + z)] - S(x, y, z, t) \tag{2.7}$$

is called then *Richards equation* and specifies the transient water flow through soil. Here, the water sink term S defines the root water uptake by plants and can be defined in several different ways (see Section 2.3). Prior, a description of water and solute movement inside the plant roots is given.

2.2 Root water flow and solute transport

Besides anchorage of the plant within the soil, the main function of a plant root system is the water and nutrient uptake. The transpiration flux through the leaves generate a water potential gradient in the plant conducting tissues, which pulls water from the soil across the roots through the plant to the atmosphere.

After overcoming the first barrier of the root, there are generally three pathways [Ehlers, 1996; Taiz and Zeiger, 2002; Yeo and Flowers, 2007] for water and solutes through the roots (see Fig. 2.1) : first, water can pass through the so-called symplastic (intercellular)

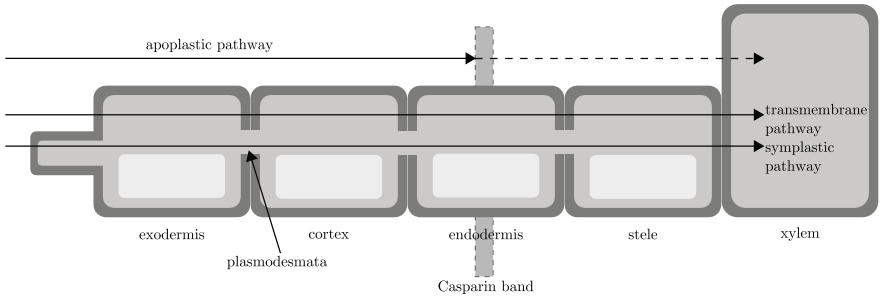

Figure 2.1: Pathways (symplastic, transmembrane and apoplastic) for water and solutes from the soil to the root xylem, adapted from Yeo and Flowers [2007].

way, moving from one cell to the next via the plasmodesmata. Second, water flow through the transmembrane way crosses a cell on one side, and leaves the cell on the other side, thus crossing at least two membranes for each cell. In the third, the apoplastic (intracellular) way, water flows along cell walls without crossing any membrane.

It is not clear which is most important pathway for water flow in different plants, but it is usually considered to be a combination of all three pathways [Taiz and Zeiger, 2002]. If a root segment has a fully developed casparian band (Fig. 2.1) without holes (e.g., due to lateral branching), which is impregnated and acts as a barrier to water and solute movement, the apoplastic way may be closed. In this case, water and solutes have to cross the casparian band in a different way, for example by crossing a membrane and using the symplastic way [Ehlers, 1996; Yeo and Flowers, 2007]. Within the root, the water enters the xylem that consists of dead cells, have no membranes or organelles, and act as water tubes inside the plant. Inside the xylem, water moves (mainly upwards) due to the water potential gradient.

These complex processes of radial water crossing into a root can be simplified by treating the radial flow with a single hydraulic conductance, as if the water is moving only through a single membrane. In addition, an axial conductance can be defined for the water flow inside the root xylem. These root hydraulic conductance depend on plant type, root age, branch type, and the soil environment, and may change also due to environmental influences (e.g., low temperature, anaerobic condition, or solute concentration (salinity) [Taiz and Zeiger, 2002]). Hydraulic conductance values from measured data [Doussan et al., 1998, 2006; Gallardo et al., 1996] can be used to model radial and axial water flow [Doussan et al., 1998].

2.3 Root water uptake

A definition of the coupling between root and soil water flow is necessary to model the soil-root interactions. This can be done at different scales and with different types of models, usually referred to as microscopic or macroscopic models. At the microscopic scale, the interface between root and soil is explicitly considered and the water flux from the soil into the plant roots is defined radially towards and into the root, but cylindrically uniform along the root length [Gardner, 1960; de Jong van Lier et al., 2006]. At this single root scale, soil properties, like water potentials very close to the root, as well as root properties such as root thickness, are taken into account and the whole root structure of a plant is assumed to be a set of these individual roots, equally spaced over the considered soil domain.

On the other hand, a macroscopic definition can be used, where the root water uptake equals the extraction term in the Richards equation (2.7), dependent on the spatial distribution of the root architecture in the soil [Hopmans and Bristow, 2002; Feddes and Raats, 2004; Skaggs et al., 2006b]. This extraction term is usually classified in two different types:

Type 1: Introduced by Nimah and Hanks [1973], the root water uptake is proportional to the unsaturated conductivity and to the difference between the total water head in the soil and at the root surface, and a computed effective xylem water potential. This mechanistic approach allows compensation of water uptake by decreasing the uptake rate in drying soil parts while increasing it in more wet areas. If an osmotic component is considered, it can be added to the soil water matric potential. However, Nimah and Hanks [1973] neglected the impact of root hydraulic properties and architecture on root water uptake. Type 1 models are, for example, developed by Schneider et al. [2010]; Doussan et al. [2006]; Javaux et al. [2008].

Type 2: The second type uses empirical functions that characterize the spatial root water uptake as a function of root length density and plant transpiration rate [Feddes and Raats, 2004]. However, special mechanisms that account for root water compensation are needed [Jarvis, 2011]. The advantage of this approach are relatively low computational costs, since these functions do not depend on single roots and their individual spatial distribution. On the other hand, the averaging of matric and osmotic water potentials, which is usually used here, might neglect important processes at the soil-root interface. Empirical root water uptake functions are used by, e.g., HDYRUS-1D [Simunek et al., 2005], HYSWASOR [Dirksen et al., 1993], and SWAP [Kroes et al., 2008].

Both types do not consider water flow in the root xylem or in the cortex, and thus neglect an important component of root uptake behavior. In addition, most of the macroscopic models solve the Richards equation in 1D, using the vertical direction only. By coupling

the hydraulic root network definition of Doussan et al. [1998] to a soil water flow model, Doussan et al. [2006]; Javaux et al. [2008] and Schneider et al. [2010] developed fully mechanistic soil-root interaction models. These models are called hybrid models, because the soil and root water flow is coupled via the sink term S in the Richards equation (2.7), which in turn depends on the radial root water flow of a 3D plant root system. In this thesis, the model of Javaux et al. [2008] is used to simulate water flow in soil and roots. The numerical implementation is described in Section 2.6.

2.4 Soil solute transport

In addition to the water flow model of Javaux et al. [2008], a stable and extended solute transport module was added. The physical fundamentals are given in the following. The solutes considered in this study are free moving, in water dissolved solution (e.g. nitrate).

2.4.1 Transport processes

Solute movement in soil is connected strongly to the water flow, but also depends on other processes. Describing solute movement in soil, the *solute flux* $\mathbf{J}_s$ [M T^{-1} L^{-2}] has to be defined out of the different processes of the transport of dissolved solute particles. Throughout this thesis, the considered components are *advection* (also called convection), *molecular diffusion* and *hydrodynamic dispersion*. Chemical reactions (e.g., decay) are implemented in the model, but go beyond the scope of this thesis and are not taken into account. The following definitions can be found for example in Rausch et al. [2005] or Hillel [2003].

Advection
Solute particle movement at the average rate of the water flux is called advection. The *advective solute flux* $\mathbf{J_c}$ [M T^{-1} L^{-2}]is defined by

$$\mathbf{J}_c = \mathbf{J}_w c, \tag{2.8}$$

where c [M L^{-3}] is the *solute concentration* in the solution and, in saturated or in unsaturated soil, the *water flux* $\mathbf{J}_w$ [L T^{-1} L^{-2}] is the Darcy or the Buckingham-Darcy flux $\mathbf{q}$ (2.5). If temperature or density gradients affect the water flow, advective transport is called *convection*, but in most cases, the distinction between advection and convection is not drawn.

Molecular diffusion
Pore-scale mixing due to Brownian motion is called molecular diffusion and causes a random movement of solute particles resulting in a gradual mixing of the solute. The solute flux $\mathbf{J}_d$ [M T^{-1} L^{-2}] caused by molecular diffusion can be described by Fick's first law [Fick, 1855]

$$\mathbf{J}_d = -\theta \mathbf{D}_m \nabla c. \tag{2.9}$$

Here, the *molecular diffusion coefficient tensor* $\mathbf{D}_m$ is defined as $\mathbf{D}_m = \mathbf{D}_d \tau$, where $\mathbf{D}_d$ is the *molecular diffusion coefficient in free water* [L^2 T^{-1}] and τ is a *tortuosity factor* [$-$], which is evaluated using the relationship $\tau = \theta^{\frac{7}{3}}/\theta_s^2$ of Millington and Quirk [1961].

Hydrodynamic dispersion
Hydrodynamic dispersion occurs due to the soil structure. Differences in pore size, in flow path length, in velocity within pores and mixing between pores cause solute spreading. Similar to the molecular diffusion, hydrodynamic dispersion is defined by

$$\mathbf{J}_h = -\theta \mathbf{D}_h \nabla c, \tag{2.10}$$

where $\mathbf{D}_h$ is the *coefficient tensor of hydrodynamic dispersion* [L^2 T^{-1} L^{-2}], defined as

$$\mathbf{D}_h = \mathbf{I}\lambda_T \|\mathbf{u}\| + (\lambda_L - \lambda_T)\frac{\mathbf{u}\,\mathbf{u}^T}{\|\mathbf{u}\|}. \tag{2.11}$$

Here, λ_L [L] and λ_T [L] are the *longitudinal* and *transverse dispersivity length*, respectively, $\mathbf{I}$ is the identity matrix, and $\mathbf{u}$ [L T^{-1}] is the *pore water velocity* that is usually given by the solution of the Richards equation ($\mathbf{u} = \mathbf{q}/\theta$).

Hydrodynamic dispersion depends, in contrast to molecular diffusion, on the direction of water flow and thus has a larger effect in the direction of flow (longitudinal) than vertical to the flow (transverse). When the convective transport is sufficiently high, the effect of molecular diffusion is much lower than of hydrodynamic dispersion. Contrary, hydrodynamic dispersion does not play a role when the soil solution is at rest.

The total solute flux $\mathbf{J}_s$ [M T^{-1}] can now be defined as sum over all three components:

$$\mathbf{J}_s = \mathbf{J}_c + \mathbf{J}_d + \mathbf{J}_h. \tag{2.12}$$

The combination of the diffusion and the dispersion coefficient to a single *effective dispersion coefficient tensor* $\mathbf{D} = \mathbf{D}_h + \mathbf{D}_m$, leads to the definition of the total solute flux

$$\mathbf{J}_s = \mathbf{J}_w c - \theta \mathbf{D} \nabla c, \tag{2.13}$$

which describes solute movement by advection, molecular diffusion and hydrodynamic dispersion.

2.4.2 Convection-dispersion equation

Like the definition of soil water movement, the mathematical formulation of solute transport in soil starts with the continuity equation

$$\frac{\partial (\theta c)}{\partial t} = -\nabla \cdot \mathbf{J}_s - S' c, \tag{2.14}$$

where the change of the solute concentration in time is equal to the negative gradient of the solute flux, minus sources or sinks $S'c$ [M T^{-1} L^{-3}]. The solute sink accounts in this thesis for the root solute uptake and is described in more detail in Section 2.5. By using the definition of Eq. (2.13), the 3D convection-dispersion-equation (CDE) can be obtained as

$$\frac{\partial (\theta c)}{\partial t} = \nabla \cdot (\theta \mathbf{D} \nabla c) - \nabla \cdot (\theta \mathbf{u} c) - S' c, \tag{2.15}$$

where $\mathbf{D}$ [L^2 T^{-1}] is the *effect dispersion coefficient tensor* (see Eq. (2.13)). While in 1D the dispersion coefficient is a scalar, in 3D the dispersion is described by a tensor, specifying dispersion in all spatial directions. For a 3D isotropic porous medium it is defined as [Bear, 1972]

$$D_{ij} = \lambda_T \|\mathbf{u}\| \delta_{ij} + (\lambda_L - \lambda_T) \frac{u_j u_i}{\|\mathbf{u}\|} + D_w \tau \delta_{ij}, \tag{2.16}$$

where δ_{ij} is the *Kronecker delta function*. More rate constants can be added to Eq. (2.15) to describe reactions of solutes in the adsorbed or dissolved phase, e.g. microbial degradation and volatilization [Bear, 1972].

2.4.3 Flux vs. resident concentration

Solute concentration c in porous media can be defined in two different ways: as *resident (volume-averaged)* or as *flux concentration* [Parker and van Genuchten, 1984; Kreft and Zuber, 1978]. Resident concentration c_r is defined by *mass of solute* (m_c) per unit volume (V) of fluid contained in an elementary volume of a system [Bear, 1972]

$$c_r = \frac{m_c}{V}. \tag{2.17}$$

In the second definition,

$$c_f = \mathbf{J}_w^{-T} \mathbf{J}_s \tag{2.18}$$

the flux concentration c_f is the ratio of solute flux $\mathbf{J}_s$ to volumetric fluid flux $\mathbf{J}_w$ and $\mathbf{J}_w^{-T}$ is the transposed, component-wise inverse flux vector $\mathbf{J}_w^{-T} = (J_{wx}^{-1}, J_{wy}^{-1}, J_{wz}^{-1})$. Both concentration definitions can be transformed into each other by [Parker and van Genuchten, 1984]

$$c_f = c_r - \left(\mathbf{D}\,\mathbf{u}^{-1}\right)^T \nabla c_r \tag{2.19}$$

where $\mathbf{u}^{-1}$ in 3D is defined as $\mathbf{u}^{-1} = (u_x^{-1}, u_y^{-1}, u_z^{-1})^T$. Thus, Expression (2.19) is valid for non-zero pore-water velocities $\mathbf{u}$ only. If $\mathbf{u}$ is zero, the flux concentration is undefined. The difference in both concentrations is important for measurements. Taking a sample from a soil volume, a resident concentration is measured, while concentration measured when flow occurs, a flux concentration is detected. In numerical solutions of the CDE, a Dirichlet boundary condition predicts flux concentrations within the soil domain and a Cauchy boundary condition a resident concentration. Using a Neumann boundary condition, specifying an outflow at a given depth, a flux concentration at the outlet is defined [Radcliffe and Simunek, 2010]. However, the deviation between both concentrations decreases with smaller apparent dispersivity [Parker and van Genuchten, 1984]. In this thesis, by default all concentrations are defined as resident concentrations $c = c_r$ unless otherwise indicated.

2.5 Root solute uptake

Solute movement in soil is affected by solute uptake by plants which is defined as solute sink term S' in the CDE (2.15). The availability of nutrients for plant roots is depended on local concentration as well as solute properties, like solubility and mobility. Solute

molecules can either reach roots by mass flow (convection) [de Wilding and van Noordwijk, 1994], or by diffusion driven by a concentration gradient to the root [Hopmans and Bristow, 2002]. While the mass flow rate relies on the local root water uptake, diffusion is caused by a concentration gradient near the root surface due to nutrient uptake by the plant. Solute (or nutrient) uptake by plant roots is taken into account in the CDE as solute sink S'.

From the plant point of view, two different mechanisms of solute uptake are used in this work: *passive* and *active* uptake. The uptake mechanism depends on the solute type [Gregory, 2006]. However, the hypothesis that active uptake becomes more important under low nutrient supply, while the transpiration driven mass flow dominates for higher concentrations, is proposed by Simunek and Hopmans [2009]; Porporato et al. [2003]. In this work, the definition of Somma et al. [1998] and Hopmans and Bristow [2002] is adopted and the *root solute uptake* term S' reads

$$S' = \epsilon S + (1 - \epsilon)A, \tag{2.20}$$

where $\epsilon \in [0, 1]$ is a *partitioning coefficient*, regulating both uptake mechanisms and defines how much solute is taken up by which uptake mechanisms. The first term of the right-hand side represents the passive solute uptake where solute enters the root dissolved in water. This term contains the water sink term S from the Richards equation (2.7) and is independent of concentration gradients around a root. In the second term, the *active solute uptake* A $[T^{-1}]$ is driven by ion uptake through electro-chemical gradients, ion pumping or uptake through ion channels.

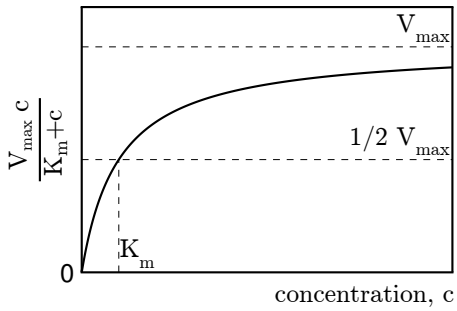

Figure 2.2: Michaelis-Menten description for active solute uptake by roots and a linear component $f = 0$ Eq. (2.21), adapted from Hopmans and Bristow [2002]

These uptake mechanisms are defined by a Michaelis-Menten-type kinetic with a linear component [Kochian and Lucas, 1982], which is distributed over the root zone:

$$A = \left(\frac{V_{max}}{K_m + c} + f \right) R_d. \tag{2.21}$$

Here, V_{max} [M $L^{-2}T^{-1}$] is the *maximum uptake rate* per area of soil-root interface, K_m [M L^{-3}] the *Michaelis-Menten constant*, denoting the concentration where the concentration uptake is half of the maximal possible uptake V_{max},and f [L T^{-1}] is the *first-order rate coefficient*, describing a linear diffusive solute uptake component. The kinetic is distributed via the *root surface density distribution* R_d [L^2 L^{-3}] over the root area and Figure 2.2 shows the Michaelis-Menten kinetic for $f = 0$, which is defined in all simulation of this thesis.

Active solute uptake is independent of the water flow and relies on local concentrations around the roots. The Michaelis-Menten parameters V_{max} and K_m vary with solute type, plant species, plant age, and several other conditions [Hopmans and Bristow, 2002]. If solutes are transported to the root surface, but are not taken up, solute particles accumulate in the root zone and increase the solute concentration there. This may lead to high osmotic gradients that also effect the root water uptake rate [Hamza and Aylmore, 1992].

2.6 Numerical implementation

After descriptions of the used physical and biological processes considered in this work, the implementations necessary for the numerical simulations are explained now. First, the coupled root and soil water flow modules are described.

2.6.1 Soil water flow

In the soil water module, the Richards equation is solved. As the hydraulic conductivity $\mathbf{K}(h)$ and the water content $\theta(h)$ are dependent on the matric head, the Richards equation is a nonlinear partial differential equation and only a few simplified analytical solutions exist. In most cases, the Richards equation is solved by numerical schemes (e.g., by finite element or finite volume methods [Bathe, 2001]). The soil water flow part in the used water module is based on the `SWMS_3D` code [Simunek et al., 1995]. It defines a Galerkin finite element method with linear basis functions on a hexaedral grid, discretizing the Richards equation in space. The voxels are virtually split into tetrahedral elements inside the code. For time discretization, an implicit (backward) finite difference scheme is applied. A Picard iteration is used to handle the non-linearity and the obtained system of linearized equations is solved iteratively by the biconjugate

gradient stabilized method (BiCGSTAB). In addition, an automatic time-step control is implemented to improve solution efficiency in transient problems. Mass balance as well as Courant and Peclet numbers are calculated. For more details of the water flow implementation see the SWMS_3D-manual [Simunek et al., 1995].

Boundary conditions can be applied as head or flux, usually at the top and bottom of a soil column. In x- and y- direction, a no-flux or a periodic condition can be set. Using periodic boundary conditions, not only the soil water flow is continuous between two opposite domain sides, but also the root architecture and thus the root water flow. Root branches projecting beyond the soil geometry enter the soil domain at the opposite side and are interpreted as root branches from a neighboring (identical) plant. This definition is closer to field conditions, preventing boundary effects of a closed soil column.

2.6.2 Root water flow

The root module calculates xylem water flow and xylem potential inside the plant roots based on the model definition of Doussan et al. [1998]. In this approach, a whole root architecture is represented as a network of connected root segments with hydraulic properties. Based on this network, radial and axial water flows inside and into the plant roots are specified.

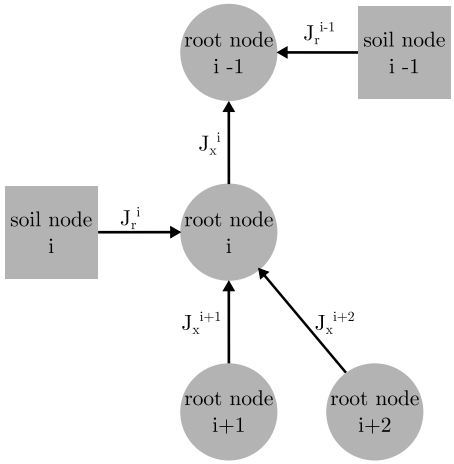

Figure 2.3: Section of a nodal root network of connected root and soil segments based on the definition by Doussan et al. [1998].

The *radial soil-root water flow* J_r^i [L^3 T^{-1}] of a root segment i is defined by

$$J_r^i = K_r^* A_r (H_{s,int} - H_{xylem}^i), \tag{2.22}$$

describing a flow through a single membrane. The *axial xylem flow* J_x^i [L^3 T^{-1}] in a root segment i is defined based on potential gradients of two root nodes by

$$J_x^i = -K_x^* A_x \left(\frac{\Delta H_{xylem}}{l_{seg}} + \frac{\Delta z}{l_{seg}} \right), \tag{2.23}$$

where K_r^* [T^{-1}] is the *radial root conductivity*, A_r [L^2] is the *outer root surface*, K_x^* [L T^{-1}] is the *xylem conductivity*, A_x [L^2] is the *xylem cross sectional area*, z [L] is the *vertical coordinate*, l_{seg} [L] is the *root segment length*, and H_{int} [L] and H_{xylem} [L] are the *total head at the soil-root interface* and the *xylem total head*, respectively. With given boundary conditions (BC) at the root collar and given water head in the soil, this leads to a system of linear equations

$$\mathbf{C}\,\mathbf{H}_{xylem} = \mathbf{Q}, \tag{2.24}$$

which can be solved for the water potential in the root xylem network. Here, $\mathbf{C}$ is the *conductance matrix*, $\mathbf{H}_{xylem}$ a vector containing the pressure heads in each root segment, and the right hand side $\mathbf{Q}$ with the soil factors [Doussan et al., 1998].

The collar BC can be applied as collar water head, as an approximation for leaf water potential, or as flow, describing a plant transpiration rate. When no root growth is simulated and a potential BC is set, the matrix $\mathbf{C}$ does not change. In this case, the linear system of equations is solved by the Gaussian elimination scheme where the LU-factors of the inverse matrix are stored after the first time-step for the whole simulation period. Thus, only the right-hand side has to be updated every time-step and is multiplied with the inverse factors to obtain the solution vector of xylem water potentials. If a flux BC is used, $\mathbf{C}$ changes and thus the stored LU-factors. To avoid a recalculation for the Gaussian elimination, the system is solved with two different water potential BCs. The solution vector for the defined transpiration rate is obtained by a linear combination of the two solution vectors with water potential BC. In simulation scenarios with root growth, the conductance matrix has to be rebuild in every growth step, and the BiCGSTAB solver is used. However, root growth was not considered in this thesis.

2.6.3 Coupled root and soil water flow

Two different geometries have to be merged for the coupling of the soil and root module: the 3D soil grid, consisting of 3D voxels, and a tree-like root network. This coupling

has to provide the soil water potential at the soil-root interfaces to the root module for solving the root flow system, and the water sink to the soil module, which is based on the radial flows into roots. The water potential at a root interface is assumed to be the same as in the soil voxel which surrounds this root segment. Therefore, the pressure head at the soil-root interface h_{int} is computed by a distance-based average of the water pressure head in the surrounding eight soil nodes i of the surrounded voxel with

$$h_{int} = \frac{\sum_{i=1}^{8} h_i \frac{1}{dist_i}}{\sum_{i=1}^{8} \frac{1}{dist_i}}, \tag{2.25}$$

where *dist* is the *distance* from the root node to a soil node.

Based on the radial root water flow of the plant root system, the water sink term S in the Richards equation (2.7) is calculated. For a soil compartment j the sink term S_j $[T^{-1}]$ is defined as

$$S_j = \frac{\sum_{k=1}^{n_k} J_r^k}{V_j}, \tag{2.26}$$

where the radial fluxes of the root segments k, located in a soil compartment j, are summed up. Here, V_j $[L^3]$ is the *soil compartment volume* and n_k is the number of root segments within compartment j. Schröder et al. [2009a] showed that this approximation gives reasonable results for a voxel size smaller than 1 cm.

Based on the initial soil water pressure head h_{int}, the root water model is solved. This generates a first approximation of the xylem water potential h_{xylem}. The resulting solution defines the radial flows between soil and root and is used to calculate the water sink term for each soil voxel (Eq. (2.26)) for the Richards equation (2.7). In this way, the root and the soil module are solved iteratively until a threshold value is reached. The threshold value is defined as the maximal change in root and soil water potential over all nodes and has to be defined at the beginning of the simulation. This approach considers root water compensation, as well as hydraulic lift, and will be used throughout this thesis.

Root water uptake decreases the pressure head in the surrounding soil to more negative values. To attain the potential transpiration rate, which is applied as boundary condition at the root collar, the water head in the root xylem has to decrease as well. When a certain water potential in the xylem is reached, plants respond by reducing their transpiration rate by stomatal closure to avoid damage inside the plant. In this case, the actual transpiration rate is not equal to the potential transpiration rate and the plant suffer from stress. Plant stress is defined in the model by setting a critical stress value of

$H_{collar}^{crit} = -15000$ cm at the root collar. When the collar pressure head reaches H_{collar}^{crit} , the BC at the root collar switches from a flow BC (transpiration rate) to a pressure head BC with a constant head of $H_{collar}^{crit} = -15000$ cm. After this switch, the actual transpiration rate T_{act} is reduced compared to the potential (applied) transpiration rate T_{pot}. When the potential transpiration demand can be fulfilled again by the total root water uptake (e.g., due to more available water in the soil or a decrease of T_{pot}), the BC type is switched back, applying the potential transpiration flux at the root collar again.

2.6.4 Solute transport

The solute modules are connected to the water modules either by the velocity field alone, given by the Richards equation (2.7), or in addition by a feedback coupling from solute to water (Section 2.6.6). Soil solute transport is solved by the model `PARTRACE`. This model uses a random walk particle tracking (RWPT) [Bechtold et al., 2011b], where the CDE is defined as an equivalent stochastic differential equation [Tompson and Gelhar, 1990]

$$X(t+\Delta t) = X(t) + \left[\mathbf{u}(X(t)) + \nabla\cdot\mathbf{D}(X(t)) + \frac{\mathbf{D}(X(t))}{\theta(X(t))}\nabla\theta(X(t))\right]\Delta t + \mathbf{B}(X(t))\xi\sqrt{\Delta t}. \tag{2.27}$$

Here, X is the *coordinate vector* $[L]$ and ξ is a *vector of three random numbers*, normally distributed with zero mean and unit variance. The *dispersion displacement matrix* $\mathbf{B}$ is the is related to the dispersion tensor by $2\mathbf{D} = \mathbf{B}^T\mathbf{B}$ [Salamon et al., 2006] and defined for a isotropic porous media [Lichtner et al., 2002]

$$\mathbf{B} = \begin{pmatrix} \frac{u_x}{\|\mathbf{u}\|}L & \frac{u_x u_y}{\|\mathbf{u}\|\sqrt{u_x^2+u_y^2}}T & \frac{u_y}{\|\mathbf{u}\|\sqrt{u_x^2+u_y^2}}T \\ \frac{u_y}{\|\mathbf{u}\|}L & \frac{u_y u_z}{\|u\|\sqrt{u_x^2+u_y^2}}T & \frac{u_x}{\|\mathbf{u}\|\sqrt{u_x^2+u_y^2}}T \\ \frac{u_z}{\|\mathbf{u}\|}L & \frac{\sqrt{u_x^2+u_z^2}}{\|\mathbf{u}\|}T & 0 \end{pmatrix}, \tag{2.28}$$

where u_x, u_y, and u_z are the *velocities* in x-, y-, and z-direction, $\|\mathbf{u}\|$ is the Euclidean norm of the velocity, $L = \sqrt{2(\alpha_L\|\mathbf{u}\|D_m)}$ and $T = \sqrt{2(\alpha_T\|\mathbf{u}\|D_m)}$.

To represent the movement of solute mass through the soil, a large number of solute particles is defined. Each solute particle has a predefined mass and is tracked through

the soil by Eq. (2.27). The *advective* (deterministic) movement of one particle is caused by the term

$$\left[\mathbf{u}(X(t)) + \nabla \cdot \mathbf{D}(X(t)) + \frac{\mathbf{D}(X(t))}{\theta(X(t))}\nabla\theta(X(t))\right],$$

which is the sum of the fluid velocity and a velocity correction that originates from the spatial variability of $\mathbf{D}$ and θ [Bechtold et al., 2011b; LaBolle et al., 1998]. The last term

$$\mathbf{B}(X(t))\xi\sqrt{\Delta t}$$

represents the *dispersive* (stochastic) movement of a solute particle. The RWPT is an Lagrangian method which solves the transport equation directly and is virtually free of numerical dispersion and artificial oscillations [Salamon et al., 2006]. Another advantage of the method are the significantly smaller computational times for very large amount of cells with strong heterogeneities, compared to the Eulerian approach. Like every particle tracking method, `PARTRACE`, conserves mass by definition and is supposed to handle high concentration gradients better then a Galerkin finite element method. These gradients occur, for example, at evaporation surface [Bechtold et al., 2011a] or at root surfaces where solutes are excluded by the plant or actively taken up. The disadvantages of the RWPT algorithm are the limitations of simulation of non-equilibrium processes and multi-species kinetic reactions [Salamon et al., 2006]. Boundary conditions can be applied either as concentration inflow or outflow, as reflection, where no solute is entering or leaving the system and solute particles are reflected at the domain border, or as periodic, where solute particles leave the soil domain at one side, and enter it at the opposite side again.

2.6.5 Root solute uptake

Solute uptake by plant roots is defined at soil voxels surrounding roots. In the particle tracking algorithm, the mass of a particle, which enters a soil voxel with solute sink definition (Eq. (2.20)) not equal to 0, is reduced by based on the solute sink defined on this soil voxel. Using this definition, the mass of some particle are reduced, but the total number of particles in the system remain the same. In case of pure passive solute uptake, the mass reduction is related to the water sink S (Eq. (2.26)) while for pure active solute uptake, it depends on predefined Michaelis-Menten parameters V_{max} and K_m, and the concentration inside a given soil voxel (Eq. (2.21)).

2.6.6 Coupled water flow and solute transport

The solute transport model solves the CDE by using the water content and velocity distribution of a current time-step, which is provided by the water flow module (water-

to-solute coupling). In addition, solute concentration can be transformed into osmotic potentials, that influences root water uptake. In this case, the transport process has an impact on the water flow. This feedback coupling from the solute to the water module during one time-step is implemented in an explicit way, using the solute concentrations at the beginning of the time-step. From this concentration distribution, the osmotic heads in the soil are calculated according to

$$h_o = \beta\, c \tag{2.29}$$

where β [$L^4\ M^{-1}$] is the transformation parameter between concentration c and osmotic head h_o. In this thesis, $\beta = -50$ cm^4 μmol^{-1} was used, calculated as averaged value of the data of Shani et al. [2007] and Hamza and Aylmore [1992].

For the flows at the soil-root interface, the water potential difference between the soil and root xylem is considered to be the sum of three components, including also the osmotic potential. The radial water flow J_r^i (Eq. (2.22)) at the soil-root interface of one root segment is then described by

$$J_r^i = K_r^* A_r \left[(h_{s,int} - h_{xylem}) + \sigma(h_{o,s,int} - h_{o,xylem})\right], \tag{2.30}$$

where the *osmotic head at the soil-root interface* $h_{o,s,int}$ [L] and *the osmotic head in the xylem* $h_{o,xylem}$ [L] is added to the matric head at the soil-root interface $h_{s,int}$ [L] and the matric head in the xylem h_{xylem} [L] (compare Eq. (2.22)). The *reflection coefficient* σ can vary between zero and one and represents the effectiveness of the membrane complex (plasmalemma and Casparian band) to selectively allow water flow but not solute transport across the complex so that osmotic potential gradients may drive a water flow across the membrane [Hopmans and Bristow, 2002]. Thus, it is a coefficient describing the relative selectivity for solutes. Note that in all simulations, the root cortex it is considered to react as a perfect membrane with a reflection coefficient $\sigma = 1$ [Knipfer and Fricke, 2010]. This is compatible with passive uptake. However, in the simulation with a reflection coefficient of $\sigma = 1$, no salt/solute uptake is considered.

Using this definition, the osmotic potential inside the xylem $h_{o,xylem}$ is neglected, and assumed to be zero. However, a plant osmotic potential could be implemented in the model straightforwardly. Considering an osmotic potential in the xylem will lead to an uptake that is similar to an uptake from a less saline soil solution. Therefore, it will not influence fundamentally the conclusions drawn from simulation results that are obtained without considering the plant osmotic potential.

2.7 Summary

Definitions of water flow, solute transport, and root uptake of water and solutes, used in this thesis are given in this chapter. Furthermore, the numerical implementation of the models is specified. By extending the model of Javaux et al. [2008] with a stable and comprehensive solute transport module, a powerful simulation tool is created. It includes now, among other processes, different solute uptake mechanisms and a feedback coupling from the solute to water module, where the concentration distribution in the soil is converted to an osmotic head. These new developments introduce new possibilities to study soil-root interactions when solute transport and root solute uptake are considered. In the next three chapters, three individual projects are presented where this extended model is applied. The objectives of the three projects are to (i) investigate the effect of root water and solute uptake on apparent soil dispersivity, (ii) analyze the effect of salinity on root water uptake, and (iii) compare simulated and monitored tracer transport in a soil-root continuum as well as to explore the effects of root system architecture and its conductance parameters on solute spreading.

Chapter 3

Effect of root water and solute uptake on apparent soil dispersivity: a simulation study*

3.1 Introduction

Understanding the effect of root water uptake on soil water flow and solute transport processes in the rhizosphere is fundamental for various agricultural problems, such as managing water and salt balances of irrigated fields or limiting leaching of pesticides [Green et al., 2006]. The presence of plants impacts solute fate not only because of the solute uptake itself (solute sink), but also because the plants affect the water velocity field by extracting water (water sink). Water uptake by plant roots decrease the water content in vegetated soil layers and disturbs the water velocity. For this reason, the vertical velocity and thus the transport velocity increase with depth, and the variability of the vertical and horizontal components of the velocity field changes, affecting solute dispersion.

How plant water uptake influences solute spreading is still a subject of ongoing debate. An apparent increasing dispersivity due to plant roots in soil was described by Vogeler et al. [2001]. In contrast, a decreasing dispersivity was reported by Gish and Jury [1983], who compared leaching experiments in cropped fields with a one-dimensional solute transport model. A similar effect was reported by Russo et al. [1998], who presented a numerical study for three-dimensional field-scale nutrient transport in heterogeneous, partially saturated soil and investigated transport of tracer and reactive solute. They detected a decreasing longitudinal nutrient spreading and a "skewing of the solute breakthrough". In their simulation study, they used a water sink term that is proportional

*adapted from N. Schröder, M. Javaux, J. Vanderborght, B. Steffen, and H. Vereecken (2012). Effect of Root Water and Solute Uptake on Apparent Soil Dispersivity: A Simulation Study. Vadose Zone Journal, Vol. 11, No. 3, doi:10.2136/vzj2012.0009

to the soil conductivity times a root effectiveness function, which was assumed to be related to the root length density.

In soils with heterogeneous water distributions and when root hydraulic conductivities are low compared with the soil hydraulic conductivity, root water uptake is not proportional to the root length density [Javaux et al., 2008]. Under such conditions, it is unclear how to determine the root water uptake distribution. This implies that numerical simulation studies that investigated the effect of root water uptake on transport processes in heterogeneous soils in fact have relied on unverified assumptions. Another limitation of simulation studies that have been performed so far is that smooth root uptake functions were used. As a consequence, flow heterogeneity that is induced by flow to individual roots (i.e., when the root length density function becomes a binary function) could not be considered. Finally, when considering the effect of root activity on solute transport, plant uptake of solutes needs to be considered as well. Whether or not solutes are taken up by plants and to what extent will have an impact on the distribution of the solute mass in the heterogeneous flow field, which can have important consequences for transport processes in heterogeneous flow fields [Vanderborght et al., 1998, 2006], and therefore on the transport process.

Studies based on numerical simulation have been used to assess the impact of various factors on solute fate, for example, soil heterogeneity [Hammel et al., 1999; Javaux et al., 2006; Russo et al., 2006] and solute chemical properties [Yang et al., 1996; Russo et al., 2004]. Although a numerical study cannot replace real experimental data, it may be used to obtain insight on how different processes have an influence on transport. In numerical simulations, certain processes can be turned on or off so that their impact can be highlighted. Numerical simulations are therefore useful to unravel sensitivities to certain processes, which may be difficult to obtain from real experiments. The advantage of one-dimensional models is their short calculation time. For large data sets and inverse simulation of measured data, they can be applied and run much faster than two- or three-dimensional models. But, neglected transport processes in the other spatial dimensions need to be lumped in parameters of the one-dimensional models. However, today, other numerical models exist that explicitly account for the three-dimensional distribution of water and solute uptake at the centimeter scale, within the root zone of a single plant (including roots from adjacent plants). In contrast to one-dimensional models, three-dimensional models at plant scale [Javaux et al., 2008] have to deal with larger numbers of root and soil input parameters, but they rely on fewer assumptions about the spatial distribution of root and nutrient uptake [Draye et al., 2010].

In this study, we present numerical solute transport experiments and investigate how water and solute uptake by the plant affects the apparent dispersivity length, which is a parameter of a one-dimensional transport model that lumps the effect of the locally three-dimensional and variable transport process on solute spreading in the mean flow

direction. Therefore, we used a model that explicitly couples water flow and nutrient uptake in a three-dimensional root structure with a three-dimensional model for water and solute transport in soil. In this model, water flow in the soil-root system is described in a fully mechanistic manner thereby avoiding empirical relationships between root density, local soil water potential, and root water uptake that are typically used to represent root water uptake in soil water flow models. A validation of this approach to simulate water uptake was given by Doussan et al. [2006].

We start our simulations with very simplified setups. Single parameters like solute uptake type or the transpiration rate are modified. Afterwards, parameters, initial and boundary conditions are adapted to describe more realistic conditions. The effect of water and nutrient uptake on the apparent dispersivity length are analyzed by fitting an effective one-dimensional transport model to horizontally averaged three-dimensional simulation results. Besides the influence of root water and nutrient uptake on the apparent dispersivity length, we also point out the importance of small-scale (approximately 1-cm resolution) flow and transport processes and small-scale variations in solute concentration in the effective parameterization of solute uptake in one-dimensional models.

3.2 Theory

3.2.1 Three-dimensional water flow model in soil and roots: R-SWMS

The three-dimensional water flow model in soil and roots, the `R-SWMS` model (Javaux et al. [2008], Schröder et al. [2008]), couples a three-dimensional soil water flow model with a root water model. In the soil, the water flow is described by the Richards equation [Richards, 1931]

$$\frac{\partial \theta}{\partial t} = \nabla \left[\mathbf{K}(h) \nabla (h + z) \right] - S(x, y, z, t) \tag{3.1}$$

where θ [cm^3 cm^{-3}] is the volumetric water content, t [d] is time, $\mathbf{K}$ [cm d^{-1}] is the hydraulic conductivity tensor, h [cm] is the matric head, S [d^{-1}] is a sink term representing the root water uptake, and z is the vertical coordinate [cm]. The soil flow equation is solved with a Finite Element (FE) Galerkin scheme [Simunek et al., 1995].

The water flow in the root network is simulated by the model of Doussan et al. [1998], where the flow within the root xylem and between the soil-root interface and root xylem is solved by discretizing the root system as a network of connected root nodes. The radial soil-root water flow J_r [cm^3 d^{-1}] and the axial xylem flow J_x [cm^3 d^{-1}] in a root segment are defined by

$$J_r = K_r^* A_r (h_{s,int} - h_{xylem}) \qquad J_x = -K_x^* A_x (\frac{\Delta h_{xylem}}{l_{seg}} + \frac{\Delta z}{l_{seg}}) \tag{3.2}$$

with the radial root conductivity K_r^* [d^{-1}], the root outer surface A_r [cm^2], the xylem conductivity K_x^* [cm d^{-1}], the xylem cross sectional area A_x [cm^2], the vertical coordinate z [cm], the root segment length l_{seg} [cm], and the water pressure head at the soil-root interface $h_{s,int}$ [cm] and in the xylem h_{xylem} [cm]. At the soil-root interface, the water pressure head $h_{s,int}$ is computed by a distance-based average of the water pressure head in the surrounding eight soil nodes:

$$h_{int} = \frac{\sum_{i=1}^{8} h_i \frac{1}{dist_i}}{\sum_{i=1}^{8} \frac{1}{dist_i}} \tag{3.3}$$

where *dist* is the distance from the root node to a soil node.

Soil and root water flow are coupled via the sink term S in the Richards equation (Eq. (3.1)). For a soil voxel j the sink term is defined as

$$S_j = \frac{\sum_{k=1}^{n_k} J_{r,k}}{V_j} \tag{3.4}$$

where the radial fluxes of the root segments k, located in a soil voxel j, are summed up. Here, V_j is the voxel volume and n_k is the number of root segments within voxel j.

Based on the initial soil water pressure head $h_{s,int}$, the root water model is solved. The resulting solution is used to calculate the water sink term for each soil voxel (Eq. (3.4)) for the Richards equation (Eq. (3.1)). Richards equation and the root water flow model of Doussan are solved iteratively until a threshold error is reached.

3.2.2 Three-dimensional solute transport model in soil: PARTRACE

After calculating the water flow in soil and root, the three-dimensional convection-dispersion-equation (CDE)

$$\frac{\partial \theta c}{\partial t} = \nabla(\theta \mathbf{D} \cdot \nabla c) - \nabla(\theta u c) - S' c \tag{3.5}$$

is solved, where c [μmol cm^{-3}] is the solute concentration, $\mathbf{D}$ [cm^2 d^{-1}] is the dispersion coefficient tensor, u [cm d^{-1}] is the pore water velocity (which is given by the solution of the Richards equation), and S' [d^{-1}] is the solute sink term. The dispersion coefficient

tensor for a three-dimensional isotropic porous medium [Bear, 1972] is given with

$$D_{ij} = \lambda_T \|u\| \delta_{ij} + (\lambda_L - \lambda_T) \frac{u_j u_i}{\|u\|} + D_w \tau \delta_{ij} \tag{3.6}$$

where D_w [cm^2 d^{-1}] is the molecular diffusion coefficient in free water, τ [$-$] is a tortuosity factor, δ_{ij} is the Kronecker delta function, and λ_L and λ_T [cm] are the longitudinal and transverse dispersivities, respectively.

For the simulation of solute transport, the random walk particle tracking (RWPT) model `PARTRACE` Bechtold et al. [2011a] was used. In the RWPT algorithm, the CDE is defined as an equivalent stochastic differential equation [Tompson and Gelhar, 1990]. This equation contains the velocity field obtained by the Richards equation and a random displacement for dispersion and is used to move a large number of solute particles, representing the solute mass, through the soil. Like every particle tracking method, `PARTRACE` is mass conservative by definition and is supposed to handle high concentration gradients, for example, at evaporation surfaces (Bechtold et al. [2011b] and at root surfaces, when solutes are excluded by the plant or actively taken up, better then a FE method.

3.2.3 Solute sink terms

For the root solute uptake term the definition of Hopmans and Bristow [2002] is adopted, where the nutrient uptake is summed up for every voxel of the soil grid and given in the sink term:

$$S' = \epsilon S + (1 - \epsilon) A, \tag{3.7}$$

where $\epsilon \in [0, 1]$ is a partitioning coefficient. The first term on the right-hand side represents the passive solute uptake with water and contains the water sink term S from the Richards equation (Eq. (3.1)). In the second term, the active solute uptake by the roots is defined by a Michaelis-Menten kinetic and a linear component

$$A = \left(\frac{V_{max}}{K_m + c} + f \right) R_d, \tag{3.8}$$

where V_{max} [μmol cm^{-2}d^{-1}] is the maximum uptake rate per area of soil-root interface, K_m [μmol cm^{-3}] the Michaelis-Menten constant, R_d [cm^2 cm^{-3}] the root surface density, and f [cm d^{-1}] is the first-order rate coefficient.

R_d is computed as follows:

$$R_d(x,y,z) = T_s \sigma'_{rs}(x,y,z) \tag{3.9}$$

and constant in time because root growth was not simulated. Here, T_s [cm^2] is the total root surface at the current time, and the function σ'_{rs} describes the distribution of root surfaces within the spatial domain Ω. The distribution σ'_{rs} is calculated in a voxel from the root surface of the root segments in the voxel around (x,y,z) $\sigma_{rs}(x,y,z)$ [cm^2] as:

$$\sigma' = \frac{\sigma_{rs}(x,y,z)}{\int_\Omega \sigma_{rs}(x,y,z) d\Omega}. \tag{3.10}$$

By representing the root water uptake and solute uptake by sink terms in the soil water and solute transport models, the geometry, orientation, and location of a root segment in a soil voxel is not explicitly considered in the soil water and solute transport models. As a consequence, water pressure head and solute concentration variations towards root segments within the voxel are not resolved.

Schröder et al. [2009a] have shown that this approach is valid for the water sink term and the pressure head distribution predictions as long as the voxel size is small enough (≤ 1 cm). The effect of approximating the solute concentration at the soil-root interface by the average concentration in the soil voxel will be evaluated using simulations with different voxel sizes.

3.3 Materials and methods

3.3.1 Virtual experiments

Virtual three-dimensional solute transport experiments under steady-state flow conditions were generated with `R-SWMS` (for water velocity field) and `PARTRACE` (for solute transport) under different conditions.

Soil domain

For all scenarios a 24-by 24-by 60-cm soil column with lateral periodic boundary conditions was defined. With a discretization of 1 cm, the simulations where run with 38,125 soil nodes and 34,560 soil elements. The Mualem-van Genuchten expression (MvG)

Table 3.1: Parameters of hydraulic soil functions $\theta(h)$ and $\mathbf{K}(h)$ for the MvG expression (loam, Vanderborght et al. [2005]): residual and saturated volumetric water content, θ_r and θ_s, respectively; MvG shape parameters, a and n; pore connectivity parameter l; saturated hydraulic conductivity K_s

θ_r [−]	θ_s [−]	a [cm^{-1}]	n [−]	K_s [cm d^{-1}]	l [−]
0.08	0.43	0.04	1.6	50	0.5

[van Genuchten, 1980] were used to describe the $\theta(h)$ and $\mathbf{K}(h)$ relations. We used parameters representing hydraulic properties for loam (Table 3.1).

Table 3.2: Top (TBC) and bottom (BBC) soil boundary condition for water and solute simulations

TBC water	TBC solute	BBC
-1 cm d^{-1}	10^{-2} μmol cm^{-3}	free drainage

As top soil boundary condition for the water flow calculation, an infiltration rate of $J_w = -1$ cm d^{-1} was chosen, and the bottom boundary was defined as free drainage. For the solute transport, a uniform solute step of $c_0 = 10^{-2}$ μmol cm^{-3} was applied for the solute flux concentration (Table 3.2). The diffusion coefficient was defined as $D_w = 1$ cm^2 d^{-1}. The Michaelis-Menten parameters were selected from Roose and Kirk [2009] for nitrate uptake: $V_{max} = 0.044$ μmol cm^{-2} d^{-1}, and $K_m = 0.05$ μmol cm^{-3}. Soil parameters for solute transport are shown in Table 3.3. The simulation time was 45 days and started at Day 45, which was the age of the simulated plants.

Table 3.3: Soil parameters for solute transport: longitudinal dispersivity length λ_L, transversal dispersivity length λ_T, molecular diffusion coefficient in free water D_w, tortuosity τ

λ_L [cm]	λ_T [cm]	D_w [cm^{2}d^{-1}]	τ [−]
1.0	$0.1\lambda_L$	1.0	$\theta^{\frac{7}{3}} \setminus \theta_s^2$

For our scenario definitions, three different types of solute uptake by the plant were specified: full passive solute uptake ($S' := S$), full active solute uptake ($S' := A$), and solute exclusion (no solute uptake, $S' := 0$). By passive uptake, solute particles enter the plant only with water, by active uptake only by the Michaelis-Menten kinetic, and by solute exclusion, no solute is taken up.

Plant root architecture

Two different plant root architectures were defined: *fibrous* and *taprooted* root systems (Figure 3.1), with both plants being 45 days old. The root structures were created

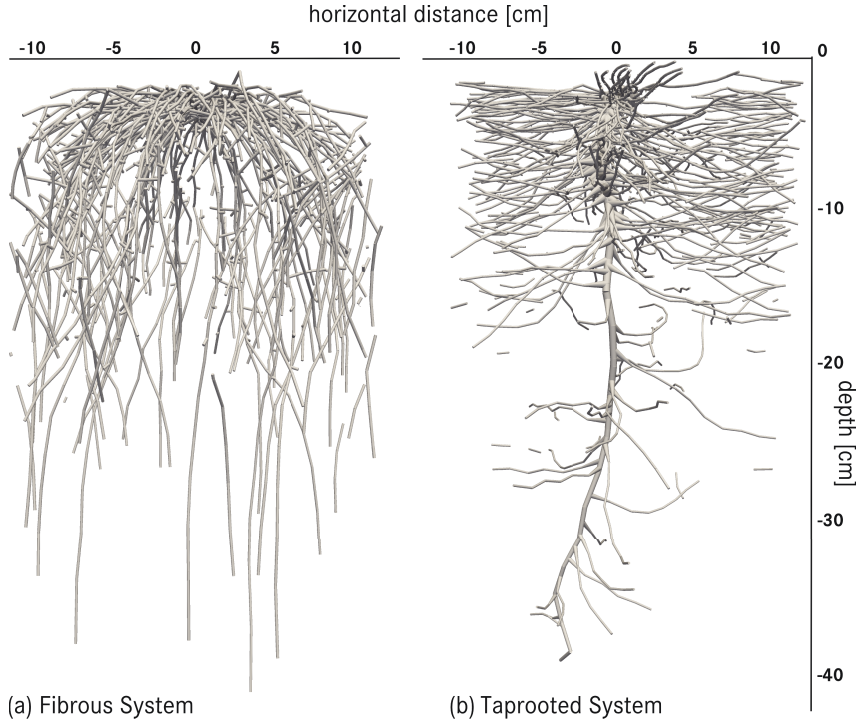

Figure 3.1: Three-dimensional root architectures of fibrous (a) and taprooted (b) plant; both generated with `Root Typ` [Pagès et al., 2004], the root diameters shown are not to scale

with `Root Typ` [Pagès et al., 2004] based on Italian ryegrass (*Lolium multiflorum* L.) and Curled Dock (*Rumex crispus* L.) architectural parameters. During the architecture generation, no spatial boundaries were defined for the root growth. If a root branch leaves the soil domain in x- or y-direction, this root branch enters the soil domain again at the opposite site. This definition of a continuous root domain fits with the periodic boundary conditions of the soil domain. Thus, not only a lonely plant in a pot was simulated, but also the root branches from "neighboring plants".

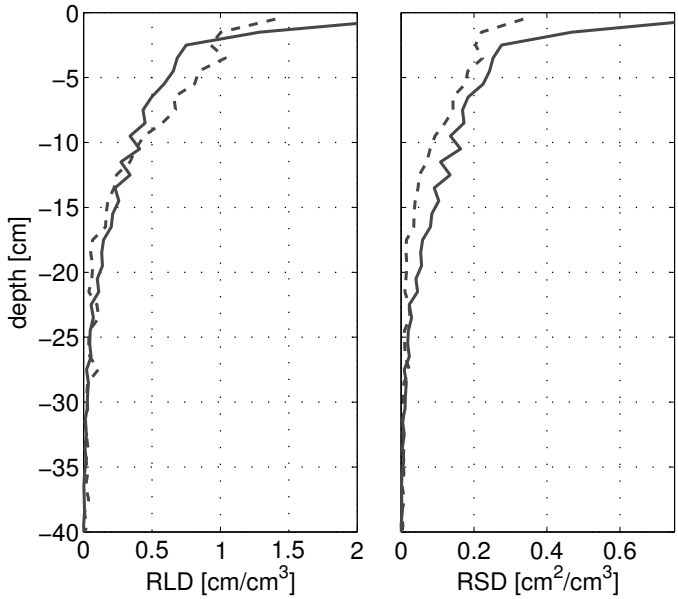

Figure 3.2: Root length density (RLD) and root surface density (RSD) for the fibrous (continuous) and the taprooted (dashed) system

The fibrous and the taprooted system have an almost identically total root length of 3.1979×10^3 cm and 3.1976×10^3 cm, respectively. The total root surface is 1.2111×10^3 cm^2 (fibrous) and 0.7054×10^3 cm^2 (taprooted). Hence, the root length density (RLD) of both structures are very similar (Figure 3.2), but the root surface density is different, which is caused by the different root diameters of the roots of the two different plants. The root diameters are also given by `Root Typ` and vary between 0.014 and 1.082 cm for the taprooted and between 0.049 and 0.15 cm for the fibrous plant. The rhizosphere was not explicitly modeled because soil voxels around the roots were not described with different soil parameters.

Table 3.4: Plant hydraulic parameters, partly adapted from Doussan et al. [2006]; radial root conductivity K_r^*, xylem conductance K_x

	1st order	2nd order	3rd order
K_r^* $[d^{-1}]$	$0.0648 \cdot 10^{-3}$	$0.181 \cdot 10^{-3}$	$0.181 \cdot 10^{-3}$
K_x $[cm^3 d^{-1}]$	4.32	4.32	4.32

For both plants, hydraulic characteristics were assumed to be constant in time and partly adapted from Doussan et al. [1998] (Tab. 3.4). Root properties were adapted following the branching order. A high axial root conductance of $K_x = K_x^* \cdot A_x = 4.32$ cm^3 d^{-1} was set for all branching orders so that the water uptake could be expected to be similar to the root length density. Radial root conductivity was set to $K_r^* = 0.0648 \cdot 10^{-3}$ d^{-1} for first branching order, $K_r^* = 0.181 \cdot 10^{-3}$ d^{-1} for second and third branching order.

3.3.2 Scenario definitions

To investigate the effects of plants on solute transport in soil, four scenarios with different levels of complexity in the boundary conditions were used. They allow analysis of the impact of the solute uptake type, the transpiration rate, the soil dispersivity length λ_L, the transient flow conditions, and the plant root architecture on the apparent dispersivity length λ_{app}.

Scenario 1: Impact of solute uptake types

A constant transpiration rate with $T_{pot} = 0.5$ cm d^{-1}, equal to one-half of the constant irrigation rate, was chosen. Infiltration and transpiration were simulated for a certain time period until a water flow steady-state condition was reached. Then, an uniform solute step was applied to the upper soil surface. This scenario was run for all three solute uptake types (passive, active, exclusion).

Scenario 2: Impact of transpiration rate

In this scenario, three transpiration rates $T1_{pot} = 0.25$ cm d^{-1} , $T2_{pot} = 0.5$ cm d^{-1} and $T3_{pot} = 0$ .667 cm d^{-1} were considered for passive uptake and solute exclusion.

Scenario 3: Impact of soil dispersivity length

In this third scenario, the impact of soil dispersivity length was investigated by changing λ_L to 0.5 cm, 1.0 cm and 2.0 cm. Water flow conditions where defined equal to Scenario 1, and a passive nutrient sink term and solute exclusion were considered.

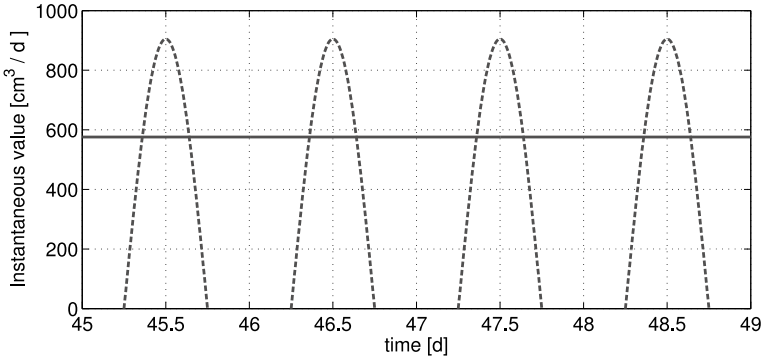

Figure 3.3: Jump function for diurnal root water uptake (dashed) compared to constant irrigation (continuous)

Scenario 4: Impact of transient flow

The impact of transient water flow was tested for solute exclusion (no solute uptake by roots). Time-averaged transpiration rate T_{pot} was defined one-half the constant irrigation, as in Scenario 1, but with a diurnal cycle for root water uptake. For the diurnal cycle, a jump function was chosen (Figure 3.3). This jump function has maxima at $t = 0.5, 1.5, \ldots$ d (corresponding to midday) and zero between $t = x.25$ d and $x.75$ d (at night). During the day the horizontally averaged water flux may be upward close to the soil surface around noon, but the time average flux over the entire day remains negative and downward. By comparing the results with those of Scenario 1, the impact of transient flow could be analyzed.

3.3.3 Scenario analysis

The workflow of the scenario simulations and scenario analysis are schematized in Figure 3.4. To derive λ_{app}, which characterizes solute spreading in an effective one-dimensional transport model, breakthrough curves (BTC) of horizontally averaged res-

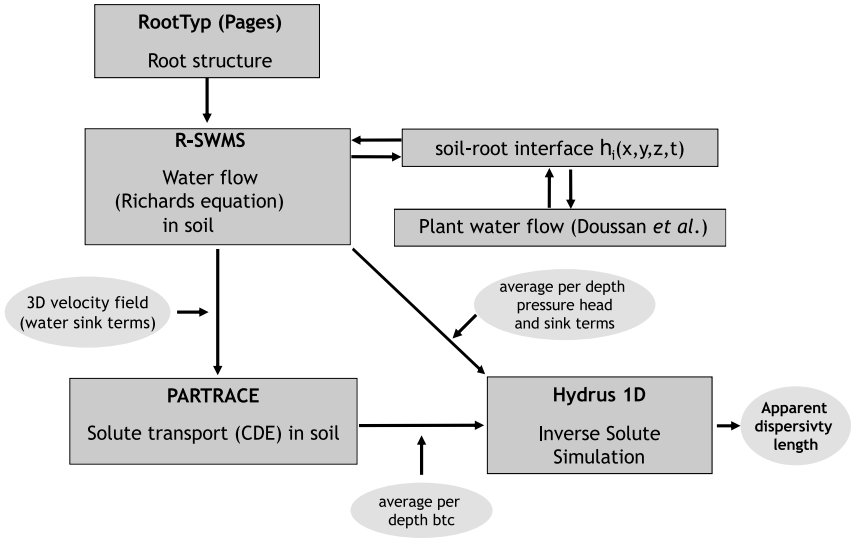

Figure 3.4: Workflow of virtual solute transport experiments and their scenario analysis

ident concentrations were calculated at different depths (z = -10, -20, -40 cm). The averaged concentrations at a certain depth were calculated as:

$$< c > = \frac{\sum_{i=1}^{N} \theta_i \, c_i \, \mathrm{vol}_i}{\sum_{i=1}^{N} \theta_i \, \mathrm{vol}_i} \tag{3.11}$$

where N is the number of soil grid voxels at a given plane and c_i, θ_i and vol_i are the voxel resident concentration, the voxel water content, and the voxel volume, respectively. Depth profiles of horizontally averaged water sink term, water content, water flux, and pressure head were calculated from the `R-SWMS` output.

The depth profile of the averaged three-dimensional sink term was used as one-dimensional sink term profile, and the averaged one-dimensional pressure head was defined as initial pressure head in the `Hydrus 1D` simulations [Simunek et al., 2005]. These initial pressure heads remained unchanged for steady boundary conditions, which shows that the average water profiles from three-dimensional and the water profiles from one-dimensional were equal. The diffusion coefficient was imposed similarly to the three-dimensional simulations (D_w = 1 cm^2 d^{-1}). For active solute uptake, the same Michaelis-Menten

constant (K_m = 0.05 μmol cm^{-3}) was used in `Hydrus 1D`, the maximal uptake rate V_{max} had to be adapted (see Section 3.5 Results: Solute Transport).

Only the apparent dispersivity length was derived from fitting `Hydrus 1D` to the breakthrough curves of horizontally averaged `PARTRACE` simulated solute concentrations. In addition, the same grid size (1 cm) was used for the effective one-dimensional transport model. The effect of the grid size on λ_{app} and solute uptake was tested by changing the grid resolution to a finer (0.5 cm) and a coarser (1.5 cm) grid (not shown). The fitted dispersivity length λ_{app} were in the same range for the finer grid (maximal difference: 0.088 cm). Therefore, simulations with 1 cm resolution were used in the comparison.

The coefficient of variation of the vertical velocity component (CVvz) is defined as the ratio of the standard deviation to the mean of the vertical velocity component.

3.4 Results: Steady-state water flow

Vertical profiles of the flux (averaged per depth), the coefficient of variation of the vertical velocity component (CVvz), and the vertical water sink term are compared for the different transpiration scenarios and both root architectures in Figure 3.5.

For a given root architecture, the flux, water sink and CVvz profiles have similar shapes for the different transpiration rates. Only small differences in flux, sink term and CVvz between the fibrous and the taprooted plant are seen at the upper 30 cm of the soil column. Below 30 cm soil depth, the profiles of both plants were similar due to absence of roots in these soil layers. With higher transpiration rate, CVvz and sink term increased, while the vertical velocity decreased. Since the dispersivity length is affected by the velocity spatial distribution, and correlated to the squared coefficient of variation of the vertical velocity, the highest apparent dispersivity length could be expected for the highest transpiration rate.

The three-dimensional distribution of the water content (Figure 3.7a, 3.7b, 3.7c, 3.7d), the water sink term (Fig. 3.7f, 3.7g, 3.7h, 3.7i), and the horizontal and vertical flux (Figure 3.6) differ significantly between both root architectures. Note, however, that the variability of the simulated water content is small (around 1 %) when compared with the variability in water content observed in field soils (up to 10 %, Vereecken et al. [2007]). This might lead to different solute breakthrough curves for both plants, even if the average one-dimensional water content, the average water sink term and the vertical flux profiles are very similar for the taprooted and for the fibrous root structure. In addition, the lateral fluxes to the roots (Figure 3.6) cannot represented with a one-dimensional model. Thus, the one-dimensional and the three-dimensional water flow and solute transport simulations may result in different predictions of solute transport.

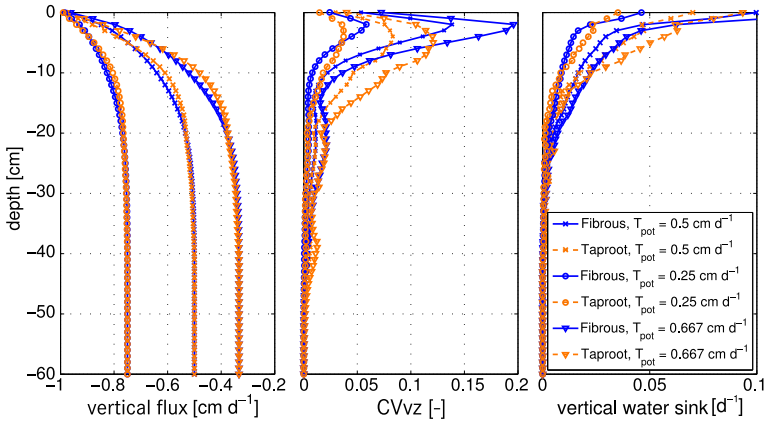

Figure 3.5: Average flux profile, coefficient of variation of the vertical velocity component (CVvz) and average water sink profiles for three different transpiration rates: $T1_{pot} = 0.25$ cm d^{-1} $T2_{pot} = 0.5$ cm d^{-1},and $T3_{pot} = 0.667$ cm d^{-1} for the fibrous (blue) and the taprooted (orange) plant; water flux at the top: $J_w = -1$ cm d^{-1};

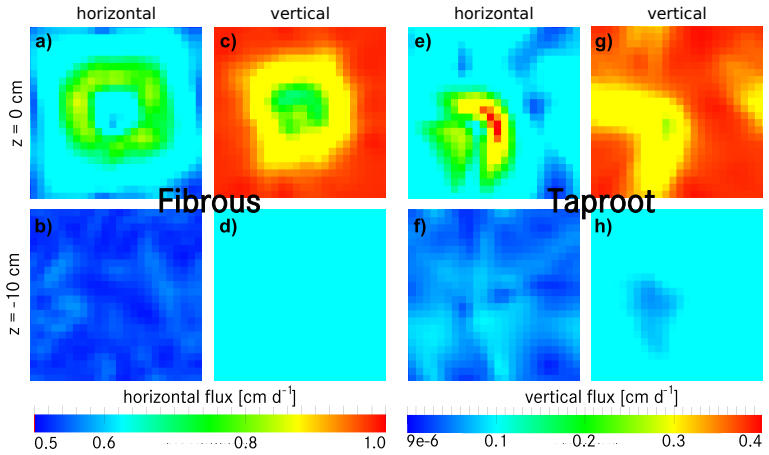

Figure 3.6: Two-dimensional x-y-planes of the horizontal (a, b, e, f) and vertical (c, d, g, h) flux distributions for the fibrous plant at $z = 0$ cm and $z = -10$ cm (a,b, e,f) and taprooted plant at $z = 0$ cm and $z = -10$ cm (c,d, g,h)

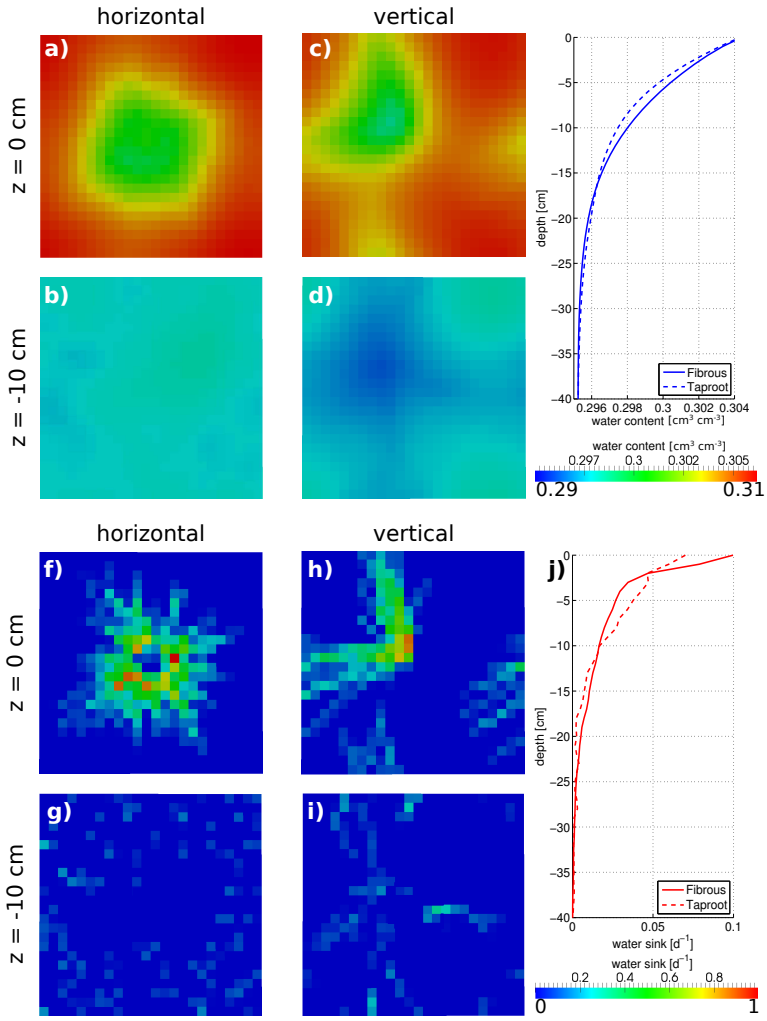

Figure 3.7: Two-dimensional x-y-planes of the water content (top - a, b, c, d) and of the water sink term distribution (bottom - f, h, g, i) for the fibrous plant at $z = 0$ cm and $z = -10$ cm (a,b, f,g) and taprooted plant at $z = 0$ cm and $z = -10$ cm (c,d, h,i); averaged (per depth) water content profile (e) and water sink profile (j)

3.5 Results: Solute transport

3.5.1 Scenario 1: Impact of solute uptake type

The simulated BTCs for the solute uptake scenarios are given in Figure 3.8. Each subfigure corresponds to one of the three different types of solute sink terms. The BTC is plotted at three depths ($z = -10$ cm, -20 cm or -40 cm) for the fibrous plant (blue) and the taprooted plant (red).

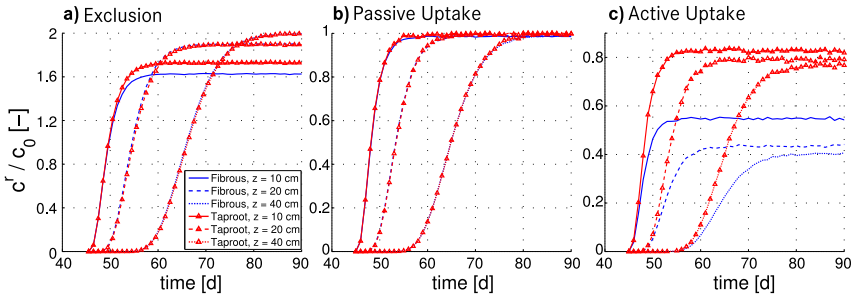

Figure 3.8: Three-dimensional numerical BTC at $z = -10$ cm, $z = -20$ cm and $z = -40$ cm of the soil column with root water uptake by a fibrous and a taprooted plant structure; water flux at the top: $J_w = -1$ cm d^{-1}, Transpiration rate $T_{pot} = 0.5$ cm d^{-1}; solute boundary condition at the top: $c_0 = 10^{-2}$ μmol cm^{-3}; the scenario was run with three different solute uptake types: solute exclusion, passive and active solute uptake

First it is observed that equilibrium concentration level changes with solute uptake type and depth. In case of nutrient exclusion (Fig. 3.8a), when one-half of the water is taken up by the plant, an increase of solute concentration in the pore water is obtained, which is twice the initial concentration below the root zone. The level of the equilibrium concentration reached in the effluent will therefore reflect the depth-integrated proportion of water that is extracted by the plant. In case of passive uptake (Figure 3.8b), the laterally averaged relative solute concentration should always be one since solute is taken up proportionally to the extracted water rate.

In case of active uptake (Figure 3.8c), when solute is extracted at a larger rate than the corresponding passive nutrient uptake with the water, relative soil solute concentration should be lower than one. In addition, the solute concentration level decreased with depth for both plants. These results are consistent with the result obtained by Simunek and Hopmans [2009], where the root zone solute concentration decreases with active

solute uptake, increases with solute exclusion, and does not change when nutrient uptake was passive.

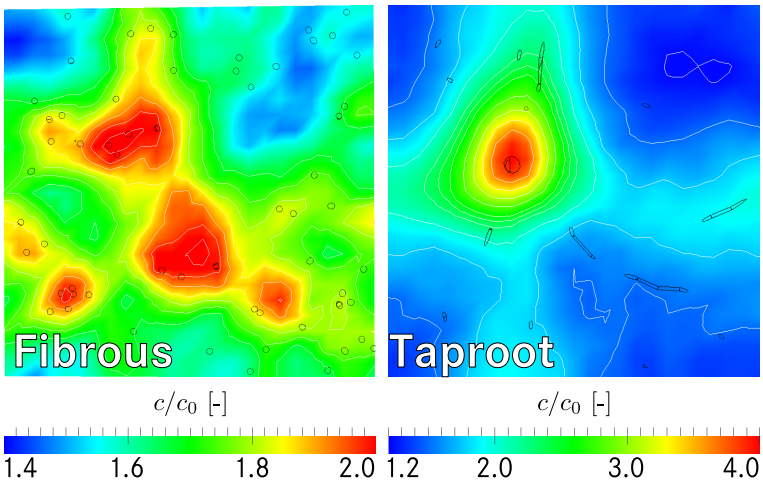

Figure 3.9: Two-dimensional x-y-planes of the local concentration (solute exclusion), scaled to the initial concentration, at $z = -15$ cm for the fibrous (left) and the taprooted plant (right); the circles represent the plant roots

The large difference between the two root architectures is only slightly reflected in slope of the BTCs with passive nutrient uptake and solute exclusion, but the equilibrated solute amount differs between the two different root types for the exclusion scenario. In particular in the upper layer, the fibrous system approached a lower averaged concentration level than the taprooted system when solute was excluded. Since the equilibrium concentration in the effluent is related to root water uptake from the soil layer between the surface and the depth where solute breakthrough is observed, this shows that in the upper soil (from $z = 0$ cm to $z = -10$ cm), the two types of plants extracted different amounts of water. Figure 3.9 shows the spatial distribution of the solute concentration in the root zone at $z = -15$ cm depth, indicating an increase of solute concentration close to the root surface. While the local concentration increased mainly around the biggest root of taprooted plant, solute accumulated more uniformly when the fibrous plant was considered, due to more uniform root distribution and water uptake.

In contrast to the passive solute uptake, more solute was removed from the soil column with active solute uptake. In this scenario a big difference can be seen between the fibrous and the taprooted plant. The breakthrough curves with the fibrous root system

reached a lower equilibrium concentration level than the taprooted system. This is due to a high total root surface of the fibrous plant, leading to a higher nutrient uptake.

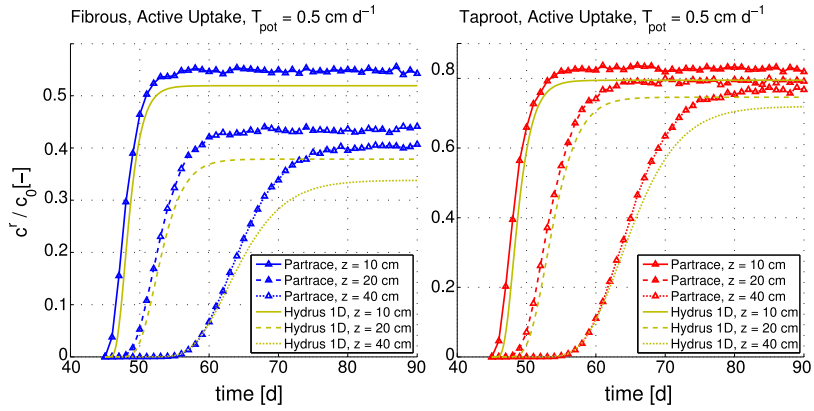

Figure 3.10: Three-dimensional numerical BTC of `PARTRACE` (fibrous plant – blue, taprooted plant – red) and `Hydrus 1D` without fitting V_{max} (green) at $z = -10$ cm, $z = -20$ cm and $z = -40$ cm of the soil column with root water and active solute uptake; the scenario was run with $T_{pot} = 0.5$ cm d^{-1}

The apparent dispersivity lengths obtained by `Hydrus 1D` are shown in Figure 3.11 for three different solute uptake types. The standard errors for all fitted apparent dispersivity lengths λ_{app} are shown in the Appendix.

Fitting the BTCs with the active solute uptake using the same values of the Michaelis-Menten parameter from the three-dimensional simulation in the one-dimensional model was not possible. When using the same values of the Michaelis-Menten parameter in one-dimensional and three-dimensional models, different concentration plateaus were simulated for active solute uptake (Figure 3.10). This effect occurs because the three-dimensional model takes the local concentration at the soil-root interface for the nutrient uptake into account. Since the active uptake was in this scenario larger than the uptake that would be expected for passive uptake (solute concentration levels were smaller than the applied concentration c_0), solute concentrations at a certain depth at the soil-root interface were smaller than the average concentration at that depth. Since uptake in the one-dimensional model is calculated on the basis of average concentrations, the calculated uptake rate in the one-dimensional model is larger than in the three-dimensional model. These local concentrations vary, for example, due to solute uptake by the plant roots, and cannot be represented in one dimension. Therefore, the solute uptake rate

V_{max} in the three-dimensional model must also be adapted so as to match the simulated BTCs. The obtained values were $V_{max} = 0.066$ cm^2 d^{-1} for the fibrous plant and $V_{max} = 0.04$ cm^2 d^{-1} for the taprooted plant.

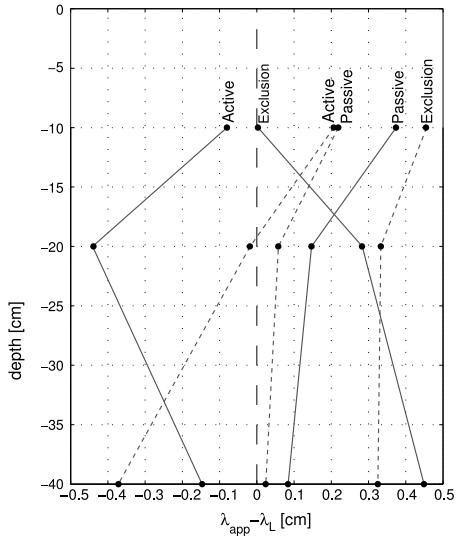

Figure 3.11: Difference of apparent dispersivity length λ_{app} minus soil dispersivity length λ_L for different solute uptake types at three soil depths ($z = -10, -20, -40$ cm); fibrous system (continuous) and taprooted system (dashed)

The effect of plant water uptake on the apparent dispersivity length was the largest for the solute exclusion scenario. An increase of the apparent dispersivity values with increasing depth was observed in the root zone of the taprooted plant, whereas a decrease was observed for the fibrous root system. For the taprooted system, the largest apparent dispersivity lengths were observed at the bottom of the root zone, despite the fact that the coefficient of variation of the vertical pore water velocity decreased to small values at this depth (Figure 3.5).

In contrast, the highest λ_{app} were observed at the top of the root zone for the passive uptake case, and the effect of passive solute uptake decreased below the root zone. This corresponds to the largest coefficient of variation of the vertical pore water velocity at the upper soil domain, which also decreased with depth (Fig. 3.5).

For the scenarios with active uptake, the apparent dispersivity length was smaller than the soil dispersivity length used in the three-dimensional simulations (Figure 3.11). For these scenarios, the solute concentrations were the smallest around the roots, where also the largest deviations in the vertical pore water velocities were simulated. As a consequence, most of the solute mass that passed the root zone for this scenario was transported in a region where the variability in pore water velocity induced by the roots was small.

3.5.2 Scenario 2: Impact of transpiration rate

In Scenario 2, both plants had similar impact on solute movement, so the results are shown for the fibrous root system, only. In Figure 3.12, the breakthrough curves for the three transpiration rates – one-quarter (T1), one-half (T2) and two-third (T3) of the total irrigation – with no nutrient uptake (blue) and passive solute uptake (red) are plotted versus the pore volume (cumulative outflow divided by the water volume in the soil between the soil surface and the depth where the BTC is simulated).

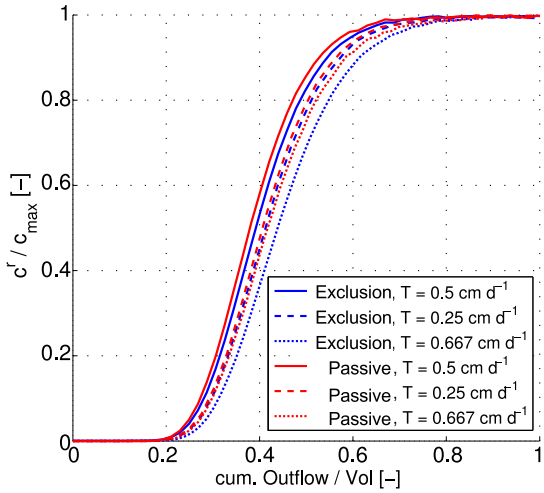

Figure 3.12: Three-dimensional numerical BTC for three different transpiration rates ($T_{pot} = 0.5, 0.25, 0.667$ cm d^{-1}) at depth $z = -40$ cm of the soil column with root water uptake by a fibrous plant; solute exclusion (blue) and passive solute uptake (red); the concentration is scaled to its maximum and compared to the cumulative water outflow

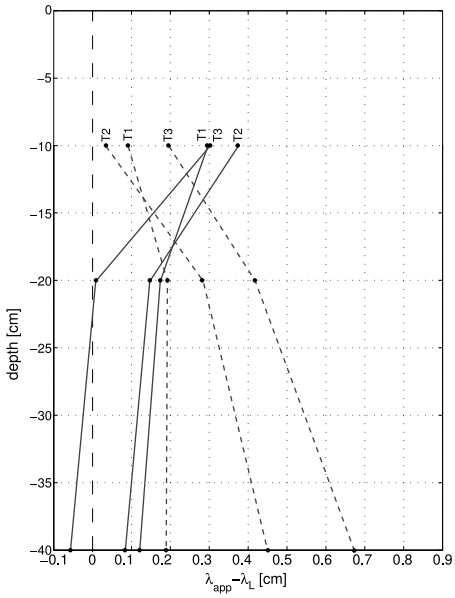

Figure 3.13: Difference of apparent dispersivity length λ_{app} to soil dispersivity length λ_L at three soil depth ($z = -10, -20, -40$ cm) for three transpiration rates (T1 = 0.25 cm d^{-1}, T2 = 0.5 cm d^{-1}, T3 = 0.667 cm d^{-1}) with solute exclusion (dashed) - passive solute uptake (continuous)

The difference between the passive solute uptake and the solute exclusion scenario is manifested by the different impact of the transpiration rate on λ_{app}. Despite the fact that the coefficient of variation of the vertical pore water velocity increased with increasing transpiration rate, the apparent dispersivity length decreased with increasing transpiration rate for the passive solute uptake scenario (Figure 3.13). This shows that for passive solute uptake the dispersivity length is correlated to the variation of the velocity field, considering soil depth. However, values lower then the soil dispersivity length of $\lambda_L = 1$ cm are obtained. From this it follows that the CVvz is not the main influence of the dispersivity length anymore when nutrients are taken up passively. Besides the CVvz, the dispersivity length is also determined by the spatial correlation of the velocity field. A higher transpiration rate and root water uptake leads to larger horizontal water fluxes, which reduces the spatial correlation in the mean flow direction of the vertical water velocity and therefore the apparent dispersivity length. A similar

effect of transient flow conditions and root water uptake on lateral solute redistribution and apparent dispersivity was observed in simulations by Russo et al. [1998].

On the other hand, for the scenario with solute exclusion, the apparent dispersivity length increased with transpiration rate. This indicates that the solute redistribution and accumulation of solute close to the soil-root interface in this scenario had an important but different impact on the transport process than the variability of pore water velocity induced by root water uptake has.

3.5.3 Scenario 3: Impact of soil dispersivity length

To investigate the impact of the soil dispersivity length λ_L used in the three-dimensional simulations we ran Scenario 1 with the fibrous root system, a transpiration rate of $T_{pot} = 0.5$ cm d^{-1}, solute exclusion and passive solute uptake, and for several soil dispersivity lengths ($\lambda_L = 0.5$ cm, 1.0 cm, 2.0 cm). Figure 3.14 shows the difference between the apparent and soil dispersivity length versus soil depth.

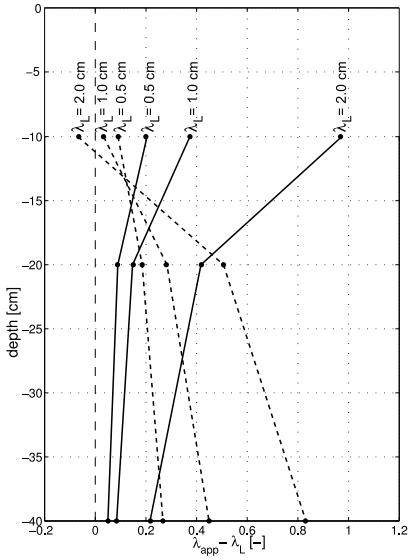

Figure 3.14: Difference of apparent dispersivity length λ_{app} minus different soil dispersivity length λ_L at three soil depths ($z = -10, -20, -40$ cm) for the fibrous root system with transpiration rate $T_{pot} = 0.5$ cm d^{-1}; passive solute uptake (continuous) - solute exclusion (dashed)

If solute is excluded, the largest relative effect on the apparent dispersivity length can be seen for the lowest soil dispersivity length ($\lambda_L = 0.5$ cm), while for passive solute uptake for the largest ($\lambda_L = 2$ cm). The difference decreased with depth when solute was taken up passively and vanishes at soil depth without plant roots ($z = -40$ cm), where almost no impact of soil dispersivity length can be seen. The results show that for both solute uptake definitions (solute exclusion and passive uptake), the difference between apparent dispersivity and soil dispersivity increased with increasing soil dispersivity. This is different from the effect that soil dispersivity has on the apparent dispersivity in soils with spatially variable soil hydraulic properties. Using approximate solutions of stochastic transport equations, Fiori (1996) demonstrated that soil dispersivity, which is also called local dispersivity, has no impact on the difference between the apparent and soil dispersivities for small soil dispersivities. For larger local dispersivity, this difference even decreases with increasing local dispersivity. This shows, that the effects of root water and nutrient uptake on λ_{app} are different and not additive compared to the effect of soil heterogeneity.

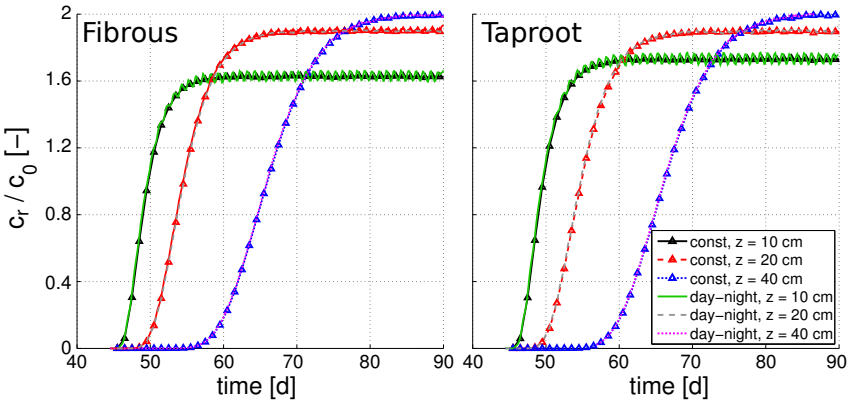

Figure 3.15: Three-dimensional numerical BTC at $z = -10$ cm, $z = -20$ cm and $z = -40$ cm of the soil column with root water uptake by a fibrous (left) and a taprooted (right) root structure; root transpiration with $T_{pot} = 0.5$ cm d^{-1}; solute boundary condition at the top: $c_0 = 10^{-2}$ μmol cm^{-3}; the scenario was run with solute exclusion.

3.5.4 Scenario 4: Impact of transient flow

The upper boundary condition of the plant collar was changed from a constant to a transient flow (Figure 3.3). The solute setup did not change, and no solute uptake

(exclusion) was defined. The six breakthrough curves, resulting by a transient and a constant boundary condition and three different depths, are compared in Figure 3.15. As there is no uptake during night, the net vertical water flux is downward, while in the middle of the day, as the instantaneous transpiration is higher than the rainfall, the flux goes to the root system. This generates the diurnal oscillation of the solute concentration in the upper root zone, while in the lower soil the effect of transient flow fades out. Below the root zone ($z = -40$ cm) no difference between BTCs, simulated with a constant or a transient collar flux, could be seen anymore.

The effect of the transient flow regime on the apparent dispersivity length depended strongly on the root structure and depth (Figure 3.16). For both root systems, the effect of transient flow conditions decreased with increasing depth. For the fibrous system, transient flow led to larger apparent dispersivity values when compared with steady state flow close to the soil surface, whereas the opposite was observed for the taprooted system. Below of the root zone ($z = -40$ cm), the apparent dispersivity values of both plants and both boundary conditions of the plant collar were in the same range.

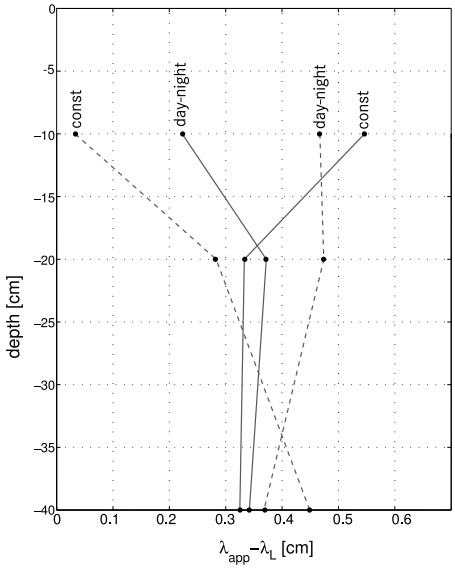

Figure 3.16: Difference of apparent dispersivity length λ_{app} minus soil dispersivity length λ_L at three soil depth ($z = -10, -20, -40$ cm) for a constant and a transient collar flux; Fibrous (dashed) - Taproot (continuous)

3.6 Summary, discussion and conclusions

Several simulation experiments were run to investigate the impact of root water and solute uptake on solute transport in soil. In these scenarios parameters and steady boundary conditions were varied, and the apparent dispersivity length, which is used as a characteristic of solute spreading in soil, was estimated by fitting solute breakthrough curves with the one-dimensional model `Hydrus 1D`. The results showed deviations of the apparent dispersivity lengths from the soil dispersivity values used in the three-dimensional simulations.

The taprooted and fibrous root architectures, with similar root length density profiles and a similar total root length, resulted in similar profiles of the mean average vertical pore water velocity but different profiles of the coefficient of variation of the pore water velocity, and water sink term distributions (Figure 3.5). When compared with apparent dispersivity length derived from simulations with a constant transpiration rate, the diurnal cycles of the transpiration rate influenced the apparent dispersivity length only in the soil layers with diurnal cycles of water content. This effect might be due to the upward total flux during the day and decreased with increasing soil depths. Below the root zone, the difference vanished.

Besides the root water uptake, the solute uptake mechanism has an important impact on solute transport. Different solute uptake mechanisms led to different redistributions of the solute mass in the heterogeneous flow field that was generated by the root water uptake. This solute redistribution also had an important impact on the apparent dispersivity length and its behavior with travel distance, and this impact depended on the root architecture.

In our simulations we considered a homogeneous soil and found that it leads to higher apparent dispersivity values for passive uptake and solute exclusion. This is in contrast with previous simulations in heterogeneous soils where the apparent dispersivity decreased due to plant water uptake [Russo et al., 1998]. In our study, the effect of water uptake by individual roots on the flow field was considered whereas in Russo et al. [1998], spatial variability of root water uptake was described on a macroscopic scale so that its effect on the smaller scale was not explicitly simulated.

For active solute uptake, we also noticed that solute uptake rate parameters that have been determined in nutrient solutions can not be transferred to simulate nutrient uptake in soils using bulk soil concentrations. It should be noted that we only considered non-sorbing solutes. For sorbing solutes, concentration gradients close to the root surface are larger than for non-sorbing solutes so that this effect will be even larger for these substances. The dependence of the dispersivity length on local spatial root solute uptake illustrate that the dispersivity length that is used in one-dimensional simulation models

should not be considered as a soil property since it depends on flow conditions and root and plant properties. To what extent these dependencies need to be considered in practical applications such as simulations for prediction of leaching plant nutrients and plant protection products out of the root zone requires further investigation.

In this study we focused on transport in a homogeneous soil in which root water and solute uptake were the only processes that generated solute redistribution and flow field heterogeneity and therefore influenced the apparent dispersivity. Soil heterogeneity also plays an important role and its impact on flow field heterogeneity and the magnitude and scale dependency of the apparent dispersivity have been investigated intensively (e.g., Vanderborght et al. [2006]). A review of apparent dispersivities that were derived from leaching experiments in undisturbed bare soils indicates that in general, the apparent dispersivity increases from 2 cm for a travel distance of 20 cm to 6 cm for a travel distance of 100 cm (see Figure 6 in Vanderborght and Vereecken [2007]). Assuming a simple linear relation between travel distance and apparent dispersivity, dispersivity would increase from 2 cm to 3 cm (i.e., by 50 %) for an increase of travel distance from 20 to 40 cm. Although we do not want to put much weight to this very simple analysis, it nevertheless illustrates that the effect of root water and nutrient uptake on the apparent dispersivity, which may also lead to an increase of apparent dispersivity by 50% over the same transport distance depending on the considered scenario, does not seem negligible when compared with the effect of soil heterogeneity. The effects of root water and nutrient uptake and soil heterogeneity on apparent dispersivity are not expected to be additive since interactions between root water uptake and the spatially variable water contents and water fluxes in a heterogeneous soil are plausible.

In further studies, the virtual experiments could be extended to simulations in heterogeneous soil. In addition, simulations with different horizontal root length density (increasing and decreasing of soil domain but with the same root structure) and simulations with similar plants, but different potential transpiration rates (heterogeneous water uptake) could point out important effects on solute movements in soil.

In our simulations, we considered cases with a high leaching rate, when compared with expected leaching rates in field soils, and with a quasi-steady flow regime. Such conditions may be relevant for experimental conditions of leaching experiments or for regularly (over)irrigated crops. Another scope of further simulation experiments could be to investigate the interactions between plant water and solute uptake and transport under more natural climatic boundary conditions leading to lower ratios of the leaching rate to the rainfall/irrigation rate at the soil surface and to a larger time scale (i.e., seasonal time scale) of the temporal variation of leaching rates. For those conditions water uptake profiles may vary considerably over time when parts of the root zone dry out and root water uptake is locally reduced. Differences in modeled profiles of root water uptake by

three-dimensional and one-dimensional models in these cases also are expected to have an impact on simulated solute transport.

Since theses studies are limited to simulation experiments, the results should also be validated with experimental data. Therefore, tracer measurements in soil with plants and root water uptake, using magnetic resonance imaging , will be performed. Comparing these experiments to our simulated data could lead to a better understanding of the effects on solute movement by root water and solute uptake.

Chapter 4

Linking transpiration reduction to rhizosphere salinity using a 3D coupled soil-plant model *

4.1 Introduction

Irrigation of agricultural lands uses 70 % of the global fresh water withdrawals [Siebert et al., 2010] and is common especially in arid and semi-arid areas to increase and optimize crop production. The high demand and the water quality decline require a careful and economical handling of the available water resources. One major problem of irrigated fields is the soil salinity. Salts accumulate in the root zone and at the soil surface and cause high osmotic potentials in the soil, which lead to very low values of the water potential near the plant roots [Hamza and Aylmore, 1992]. Plants suffering from salt stress respond by reducing their transpiration rate, and thus their yield [de Wit, 1958].

Soil-hydrological models may be used to predict plant response to salt stress. In these models, a potential transpiration rate T_{pot}, which corresponds to transpiration under optimal growing conditions, is defined and distributed as a water sink term over the root zone, commonly as a function of the root length density. If the potential atmospheric demand cannot be supplied by the plant, due to too much/little water and/or too much salt in the soil, the transpiration is reduced. In a soil hydrological context, this reduction is defined as plant stress.

In a first type of models, called type II models [Hopmans and Bristow, 2002], the stress response function α is defined as a function of matrix water potential and/or the osmotic potential in the root zone. Stress response functions link a whole plant response

*adapted from N. Schröder, N. Lazarovitch, J. Vanderborght, H. Vereecken and M. Javaux. Linking transpiration reduction to rhizosphere salinity using a 3D coupled soil-plant model. Plant and Soil *accepted*

(described by relative yield or relative transpiration) to salts and water in the root zone, as:

$$\frac{Y_{act}}{Y_{pot}} \text{ or } \frac{T_{act}}{T_{pot}} = \alpha, \tag{4.1}$$

where Y_{act} is an actual yield, Y_{pot} is a potential yield, T_{act} is an actual transpiration rate, and T_{pot} is a potential transpiration rate.

Several stress response functions have been developed over the years [Homaee et al., 2002c; Feddes and Raats, 2004], whereas two mathematical formulations are most common: piecewise linear for salt stress [Maas and Hoffman, 1977] and for water stress [Feddes et al., 1976] and s-shaped functions for water and salt stress [van Genuchten, 1987; van Genuchten and Hoffman, 1984], but other modified functions exists [Feddes and Raats, 2004]. Salt and water stress response functions were often developed independently. If a combination of both stress types is described, salt and water response functions are added (osmotic and matrix potential), multiplied (stress response for salt and water), or otherwise recombined [Homaee et al., 2002a]. The right way to combine two stress functions has been subject of discussion in the literature [Homaee et al., 2002b; Hopmans and Bristow, 2002; Feddes and Raats, 2004].

However the use of such stress functions and their combination has been criticized. Water and salinity stress functions must link the response of the whole plant, i.e. transpiration rate or yield, to matrix and osmotic water potentials in the root zone, which vary considerably with depth, with horizontal distance to roots, and with time. A typical approach is to infer the whole plant response from a composite of local stress responses, which are derived from local soil matrix and osmotic potentials. However, since the root system is hydraulically connected the local response of the system does not depend solely on the local conditions but also on the conditions at other locations in the root zone [Skaggs et al., 2006a]. In case of heterogeneous soil matrix potential, for instance, a local reduction of water uptake may be compensated by an increase in water uptake at other depths where sufficient water is still available [Jarvis, 2011]. Applying local stress functions without a link to conditions at other locations in the root zone may therefore lead to errors in simulated water uptake distributions.

Another potential weakness of type II models arises from the fact that bulk soil (and not soil-root interface) water potentials are used in stress functions. Water uptake by a single root creates a radial water potential gradient towards and salt accumulation at the soil-root interface so that the water potential at the interface differs from bulk soil water potential. The difference depends on the soil hydraulic properties, the uptake rate, and the root density. We postulate that the gradients of matrix potential and the gradients of osmotic potential between bulk soil and soil-root interface will be different as well. Since water potentials at the soil-root interface are relevant for plant stress,

stress functions defined in terms of bulk soil water potentials should be functions of soil hydraulic properties, root densities, water uptake, and also of the type of stress (i.e. matrix versus osmotic stress). These dependencies should be parametrized in stress functions of type II models.

In addition to type II models, Hopmans and Bristow [2002] also defined type I models in which the water flow in the soil-root system is described in a mechanistic manner and based on water potential differences/gradients and conductance/conductivities along a flow line in the soil-plant system. The major advantages of this modeling approach are that local processes between the bulk soil and the soil-root interface and hydraulic connections in three-dimensional root architecture are simulated explicitly based on principal laws of water flow in porous media (also the root tissue can be considered as a porous medium). Type I models therefore avoid empirical parametrization of root water uptake, uptake compensation, and stress functions that are used in type II models. Simulations using type I models can be used to derive parametrization for type II models. Metselaar and de Jong van Lier [2007]; de Jong van Lier et al. [2009] and Couvreur et al. [2012] used type I models to parametrize root water uptake functions for the case of matrix potential stress.

For combined matrix and osmotic potential stresses, Cardon and Letey [1992] compared the sensitivity of type I and type II models. They used the type I water uptake model of Nimah and Hanks [1973] and concluded that it was insensitive to osmotic stress, while the type II model (zero-to-one stress function) produced, when compared with experimental data, more reasonable results.

The Nimah and Hanks [1973] model calculates the radial water flow into the root based on the difference between the bulk soil water potential and the water potential in the root. Yet, the accumulation of salts at the soil-root interface was not considered in the model, which may be a reason for the small sensitivity of the used type I model to bulk soil osmotic potentials. Therefore, we refined the model and considered also three-dimensional (3D) water and salt transport in the soil towards the 3D root architecture so that water flow into the root can be modeled based on the potential difference between the potential at the soil-root interface and inside the root.

The objectives of the study are (1) to investigate how the stress functions used in type II models depend on the total water potential and its partial potentials: matrix and osmotic potentials, and on the transpiration rate, and (2) to analyze stress responses as a function of water potentials at the soil-root interface and in the bulk soil. Therefore, we will carry out simulations using the type I model R-SWIMS [Javaux et al., 2008], which considers 3D flow and transport in the coupled soil-root system.

We hypothesize that the local water potential at the soil-root interface, which is 'felt' by the plant, is the key to a unique stress function for salt and water stresses, in case there

is no plant osmotic adjustment. We further hypothesize that when a perfect osmotic membrane is present in the roots, which separates water in the root transport tissue (xylem) from soil water, how the local water potential at soil-root interface is made up by osmotic and matrix potentials is irrelevant for root water uptake. However, the different spatial distributions of the matrix potential and the osmotic potential around individual roots lead to different sensitivities of water uptake to bulk matrix or osmotic potentials, when potential gradients occur. Therefore, we hypothesize that at the macroscopic scale, the effect of the bulk osmotic potential on root water uptake will be different from the effect of the bulk matrix potential.

First, we compare experimental data from measurements by Hamza and Aylmore [1992] with simulated data to validate our model. In their experimental setup, salt accumulation of Na^+ at the root surface of a lupine plant was detected with Na^+-LIX microelectrodes. In addition, leaf water potential and the actual transpiration rate were measured. Different simulation runs were performed based on these experimental setups with four saline treatments and the experimental and simulated data are compared. In a second step, a simple setup, consisting of one vertical root in the middle of a soil cube, was considered. In this setup, scenarios with different salinities and transpiration rates were defined in order to analyze the transpiration response to local soil water potential. Finally, a more realistic case was simulated for a root system typical of grassland to assess the impact of more complex root architectures on a one-dimensional (1) effective salt stress function.

4.2 Theory

The total water potential is equal to

$$H = h + h_g + h_o, \tag{4.2}$$

where H is the total water potential, h is the matrix potential, $h_g = z$ is the gravitational potential, and h_o is the osmotic potential.

In soil hydrology, potentials are mostly defined on a weight basis and potentials or heads have dimension length. In plant sciences, potentials are mostly defined on a volume basis and potentials have dimension of a pressure. Heads can be simply translated to pressures by multiplying the head by $\rho_w g$ where ρ_w is the density of water and g the acceleration due to gravity. We use for potentials dimension [cm] in the following, which approximately corresponds with pressure in [h Pa = 10^2 Pa].

It should be noted that osmotic potential gradients only drive liquid water flow when salt movement is restricted compared with the movement of water molecules. This might be

the case for flow across selective membranes such as plant cell membranes or through thin water films in porous media in which the mobility of hydrated ions is restricted [Nassar and Horton, 1997]. For the cases considered here, we will neglect water flow due to gradients in osmotic potential in the soil.

Based on this definition of the total water potential and on analytical solutions of water flow in a root system, Couvreur et al. [2012] developed a new model of plant water stress. In their model, water stress and compensatory root water uptake are clearly decoupled and an explicit equation for the actual transpiration rate T_{act} [cm^3 d^{-1}] is proposed as:

$$T_{act} = K_{rs} \left(\sum_{j=1}^{M} H_{s,j} SSF_j - H_{collar} \right), \tag{4.3}$$

where K_{rs} [cm^3 cm^{-1} d^{-1}] is the equivalent conductance of the complete root system, M [-] is the total number of soil elements, $H_{s,j}$ [cm] the total water potential at the soil-root interface in a soil compartment j, H_{collar} [cm] the water potential at the root collar, and SSF_j [-] is the standard sink fraction in the j-ht soil element. The vector of standard sink fractions, SSF, represents the distribution of the normalized sink terms in the soil domain for the case of a uniform soil water potential distribution in the soil profile. The SSF_j depends on the root system architecture and its hydraulic properties and is obtained by solving the flow equation in a network of root segments for a uniform water potential at the soil-root interface [Doussan et al., 1998; Couvreur et al., 2012]. The term $\sum_{j=1}^{M} H_j SSF_j$ is the SSF-weighted mean soil water potential at the soil-root interface and represents the plant-sensed soil water potential. If no salinity is considered, the water potential is the sum of matrix and elevation potential ($H = h + z$), while with salinity, the osmotic potential is added ($H = h + z + h_o$).

Stress in this model is defined to occur when H_{collar} reaches a predefined value, H_{collar}^{crit} below H_{collar} cannot fall due to leaf stomata regulation. In this case, T_{act} can be calculated from Eq. (4.3) for the soil water potential distribution and the water potential at the root collar.

Dividing Eq. (4.3) by T_{pot} [cm^3 d^{-1}], the transpiration reduction factor can be estimated as

$$\alpha = \frac{T_{act}}{T_{pot}} = \frac{K_{rs}}{T_{pot}} \left(\sum_{j=1}^{M} H_{s,j} SSF_j - H_{collar} \right). \tag{4.4}$$

For $H_{collar} > H_{collar}^{crit}$ the potential atmospheric demand can be fulfilled and α is equal to 1 ($T_{act} = T_{pot}$). In the case of $H_{collar} = H_{collar}^{crit}$, water uptake by the plant is reduced

linearly to the plant 'felt' soil water potential. Since they link the whole plant response, i.e. transpiration rate to an averaged soil water potential, Eq. (4.3) and (4.4) give some indications about the shape of type II models. According to Eq. (4.3) and (4.4), the transpiration reduction should be a function of the sum of local matrix and osmotic potentials and should be independent of the nature of the partial water potential that generates stress. This contradicts type II models that use products of stress response functions to respectively matrix and osmotic potentials, e.g. Hydrus-1 [Simunek et al., 2005], SWAP [Kroes et al., 2008] or HYSWASOR [Dirksen et al., 1993].

Eq. (4.3) and (4.4) also indicate that the reduction functions should be linear functions with a slope that depends on root properties, K_{rs}, the potential transpiration rate, T_{pot}, but is independent of soil properties. However, the water potential in Eq. (4.3) and (4.4) is defined at the soil-root interface and is therefore a local variable that may differ from the bulk averaged water potential at a certain depth in the soil profile.

In the following, we will use detailed 3D simulations of water flow and salt transport in the soil towards roots and inside the root system in a saline soil. The simulation results are used subsequently to evaluate the shape of of reduction functions when water potentials are determined as an average of the potentials in the bulk soil around roots.

4.3 Materials and methods

4.3.1 Modeling

We used the simulation model R-SWIMS [Javaux et al., 2008] that solves the 3D Richards equation [Richards, 1931] to describe water flow in the soil and the Doussan equations [Doussan et al., 1998] to describe water flow inside and into the plant roots. These equations describe fluxes in the root network based on pressure potential differences across a membrane between the soil-root interface and the root xylem, pressure potential gradients along root segments, and radial and axial root conductance or conductivities.

Solute transport in the soil is modeled by the 3D convection-dispersion equation (CDE) and solved with a particle tracking algorithm [Bechtold et al., 2011a; Schröder et al., 2012]. Since the transport influences osmotic potentials and therefore root water uptake, the transport process has an impact on the flow. This feedback-coupling between water flow and solute transport within one time step was implemented in an explicit way, using the solute concentrations (transformed to osmotic potentials) at the beginning of one time-step to calculate the radial flows at the soil-root interface. More details of the coupling of the different model modules are given in Chapter 2.

The water potential difference between the soil and the root xylem in a certain root segment j is considered to be the sum of two components: h and h_o. The radial flow into the root segment j is described using the following equation [Hopmans and Bristow, 2002]

$$J_r^j = K_r^* A_r \left[(h_{int} - h_{xylem}) + \sigma \left(h_{o,int} + h_{o,xylem} \right) \right], \tag{4.5}$$

where K_r^* [d^{-1}] is the radial root conductivity, A_r [cm^2] is the root outer surface, h_{int} [cm] and $h_{o,int}$ [cm] are the matrix and the osmotic potential at the soil-root interface, and h_{xylem} [cm] and $h_{o,xylem}$ [cm] the pressure and the osmotic potential in the xylem.

The reflection coefficient σ can vary between zero and one and represents the effectiveness of the membrane complex to selectively allow water flow but no salt transport across the complex so that osmotic potential gradients may drive a water flow across the membrane [Hopmans and Bristow, 2002]. Note, that we consider in all simulations that the root endodermis reacts as a perfect membrane with a reflection coefficient $\sigma = 1$ [Knipfer and Fricke, 2010]. As mentioned before, the potentials at the interface h_{int} and $h_{int,o}$ are defined locally as the matrix and osmotic potential in the soil voxel around a given root segment. In our definition, we neglect the osmotic potential inside the xylem ($h_{o,xylem}$), and assume it is zero, which means that we also neglect any plant osmotic adjustment. However, a plant osmotic potential could be implemented in the model straightforwardly. Considering an osmotic potential in the xylem will lead to an uptake that is similar to an uptake from a less saline soil solution. Therefore, it will not influence fundamentally the conclusions drawn from simulation results that are obtained without considering the xylem osmotic potential.

Plant stress was defined in the model by setting a critical stress value of $H_{collar}^{crit} = -15000$ cm (≈ -1.5 MPa) at the root collar, to simulate an isohydric plant behavior [Tardieu, 1996]. When the collar potential reaches H_{collar}^{crit}, the boundary condition (BC) at the root collar switches from a flow BC (transpiration rate) to a constant potential BC equal to H_{collar}^{crit}. After this switch, the actual transpiration rate T_{act} is reduced compared to the potential (applied) transpiration rate T_{pot}. When the potential transpiration demand can be fulfilled again by the total root water uptake, for example due to more available water in the soil or a decrease of T_{pot}, the BC type is switched back, applying the potential transpiration flux at the root collar.

4.3.2 Simulation setup

Three scenarios were run in this study. The first one aimed at validating our model by comparing simulation results to data from the literature. A second setup allowed us to

investigate the sensitivity of the effective reduction function obtained from the 3D model to to osmotic and matrix potentials at the soil-root interface and in the bulk soil, and to the transpiration rate. Finally, a larger scale scenario was run with a more realistic plant root structure to investigate the impact of root distribution on effective stress functions. The simulation results are evaluated based on the approach of Couvreur et al. [2012] (Eq. (4.3) and (4.4)).

Calculation of matrix and osmotic potentials

The salt concentration c [μmol cm^{-3}] in the model was transferred to the osmotic potential h_o [cm] according to

$$h_o = \beta \cdot c \tag{4.6}$$

with

$$\beta = -50 \frac{cm^4}{\mu\text{mol}}.$$

The parameter β was calculated as averaged value of the data of Shani and Ben-Gal [2005] and Hamza and Aylmore [1992].

The water potential at the soil-root interface was computed for the complete root domain as a weighted average of potentials in all soil voxels that contain one or more root segments. The voxels size was assumed to be small enough (see Schröder et al. [2009a] for details about the voxel size) so that the water potential in the voxel represents the water potential at the soil-root interface. Bulk soil water potential for the whole soil domain was calculated as a weighted average of potentials in all voxels of the soil domain. For both, the soil-root interface and bulk soil average water potentials, the standardized sink fractions (SSF) were used as weights. Since the SSF is only defined in soil voxels containing a root segment, water potentials in voxels further away from roots were weighted by the SSF of the nearest voxel containing a root segment.

In addition, average water value of all voxels that are at a certain distance to the nearest root was calculated. Doing this for different distances, the spatial variation of water potential in the radial direction to the root segments was derived.

Scenario 1: Comparison to Hamza and Aylmore dataset

In the first simulation setup, a soil column of 4.5 x 4.5 x 12 cm with 0.5 cm grid spacing was defined so as to compare the simulation results with measured data from Hamza and Aylmore [1992]. In their experiment, salt accumulation of Na^+ at the root surface,

leaf water pressure potential and the actual transpiration rate of a single lupine root were measured. The water retention curve and diffusivity function of the used soil (85 % Bassendean sand and 15 % Clackline kaolinite form Western Australia) were measured by Hainsworth and Aylmore [1986]. The parameters of the Mualem-van Genuchten (MvG) hydraulic functions [van Genuchten, 1980] were obtained by fitting using the RETC software [van Genuchten et al., 1991] and are given in Table 4.1 ($R^2 = 0.907$).

Table 4.1: Mualem-van Genuchten parameter for the different simulation scenarios; HA86 = Hainsworth and Aylmore [1986]

	θ_r [cm^3 cm^{-3}]	θ_s [cm^3 cm^{-3}]	a [cm^{-1}]	n [-]	K_s [cm d^{-1}]	l [-]	Scenario
HA86	0.001	0.432	0.00285	2.867	0.723	0.355	1
clay loam	0.095	0.41	0.019	1.31	6.24	0.5	2,3

A single plant root with a total length of 12 cm was located in the center of the box. The hydraulic characteristics of the roots were assumed to be constant over time and uniform along the root. The root axial conductance was set to $K_x = K_x^* A_x = 0.2592$ cm^4 d^{-1} cm^{-1} and a radial conductivity K_r^*, equal to 0.000864 cm d^{-1} cm^{-1} was assumed, based on measured values of lupine roots by Doussan et al. [2006]. Plant transpiration rates measured by Hamza and Aylmore [1992] were used as collar boundary condition and four treatments with different initial salt concentration in the soil ($c_{init} = 25, 50, 75, 100$ μmol cm^{-3}) were simulated. Analog to their experimental setup, no infiltration and no outflow were defined and the initial water content was $\theta_{init} = 0.3$ cm^3 cm^{-3}. Simulation outputs were compared to the experimental data at $2, 4, 6$, and 8 hours after the start of the experiment similarly to their study. We assumed that the water potential at the root collar is a good proxy of the leaf water potential (pressure potential loss in the stem was considered as negligible).

With this comparison, we also verified whether our assumptions of no osmotic adjustments and a constant reflection coefficient of $\sigma = 1$ are valid. Therefore, we started from the following general function to describe the relation between T_{act}, leaf pressure potential h_{leaf} [cm], osmotic potential and matrix potential (see Eq. (4.3)).

$$T_{act} = K_{eff} \left(|h_{leaf}| + \sigma \left(|h_{o,int}| - |h_{o,xylem}| \right) - |h_{int}| \right), \tag{4.7}$$

This can be rewritten as

$$T_{act} = K_{eff}\left(|h_{leaf}| - |h_{int}| - |h_{o,int}|\right) + K_{eff}\left(1-\sigma\right)|h_{o,int}| + K_{eff}|h_{o,xylem}| - |h_{int}|. \tag{4.8}$$

When we assume that $\sigma = 1$ and that $h_{o,xylem} = 0$, then T_{act} versus $|h_{leaf}| - |h_o| - |h|$ for all salt concentrations fall on the same line through the origin and the slope should be equal to K_{eff}. If $\sigma = 1$ but $h_{o,xylem}$ is different from 0, T_{act} plotted against $|h_{leaf}| - |h_o| - |h|$ results in a line but with an intercept. If the osmotic potential has less influence on root water uptake ($\sigma < 1$), or does not play any role ($\sigma = 0$), then T_{act} versus $|h_{leaf}| - |h|$ should be a line through the origin for all salt concentrations.

Scenario 2: Simulated stress function with a single root

In this second scenario we analyzed the plant stress response due to salt accumulation around roots using a very simplified simulation setup with a single root only, which is similar to the experimental setup of Hamza and Aylmore [1992]. The defined geometry for the single root setup is shown in Figure 4.1a. The soil column geometry was 4.5 x 4.5 x 10 cm, discretized with 0.5 cm cubes. The soil column was filled homogeneously with clay loam (MvG-parameters in Table 4.1).

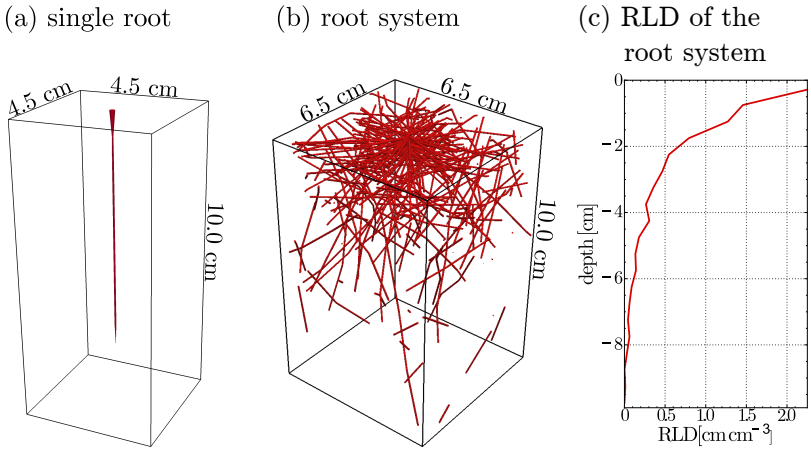

Figure 4.1: Three-dimensional root architectures and soil geometry for (a) the single root setup and (b) the whole plant root structure (25 days old); (c) Root length density (RLD) of the plant root architecture;

The single plant root had a total length of 8 cm and was placed in the center of the box, leading to a root length density (RLD) of 0.04 cm cm^{-3}. Axial root conductance was set to $K_x = 0.0432$ cm^4 d^{-1} cm^{-1} and the radial conductivity was set to $K_r^* = 0.000178$ cm d^{-1} cm^{-1} [Doussan et al., 1998]. The root hydraulic characteristics were assumed to be constant over time and uniform along the root. As root boundary condition, three different constant potential transpiration rates ($T_{pot} = 1.0, 1.5, 2.0$ cm ^{3} d $^{-1}$) were applied at the root collar. The transpiration rates were chosen very low due to the small size of the single root. For example, for a root zone of 1 m, the root water uptake of 1 cm^3 d^{-1} by a root segment of 8 cm would then correspond with a transpiration rate of 6 mm d^{-1}.

At all boundaries (top, bottom, left, right, front, back) a no flux boundary condition for water flow simulation and a reflection condition for the particle tracking was set during the simulations. The initial matrix potential was $h_{init} = -1000$ cm and the initial solute concentration c_{init} in the soil solution varied between different scenarios ($5, 10, 20, 30, 60, 90, 120, 150, 200, 250$ μmol cm^{-3}), and were always defined uniform over the soil domain. The longitudinal dispersivity length α_L was set to 1 cm and the transverse dispersivity length to $\alpha_T = 1/10\,\alpha_L$. The diffusion coefficient D_W of salt in free water was 1 cm^2 d^{-1}. The simulations were run for 6 days.

Scenario 3: Stress function for a full root architecture

As we expected that root spatial distribution could impact the apparent stress function, a setup with whole plant architecture was simulated. Therefore, a 25 days old plant root architecture was set centered in a soil domain (Figure 4.1b). This architecture was created with RootTyp [Pagès et al., 2004], based on parameters for Italian ryegrass (*Lolium multiflorum* L., in Schröder et al. [2012]). The soil domain was 6.5 x 6.5 x 10 cm and resulted in the root length density profile shown in Figure 4.1c.

For this root system, axial root conductance, radial root conductivity and the limiting pressure potential at the root collar were identical to the single root simulations and constant in time and branching order. In x- and y-directions of the soil domains, periodic boundary conditions were defined for soil water and solute transport, as well as for the root architecture and the root water flow [Schröder et al., 2012]. In this definition, the root branches that leave the soil boundary on one lateral boundary enter the domain again from the opposite side. This definition is closer to field conditions, as boundary effects of a closed soil pot are prevented and the re-entered root branches are interpreted as branches from neighboring plants.

We assumed an irrigation with saline water before the simulation begun, and started with wet, but saline soil defining an uniform initial matrix potential $h_{init} = -300$ cm

and an uniform initial soil solution concentration of $c_{init} = 30$ μmol cm^{-3}. The daily potential transpiration rate was $T_{pot} = 20$ cm^3 d^{-1} and applied as sinusoidal day-night circle. The simulation run for 10 days.

4.4 Results and discussion

4.4.1 Scenario 1: Comparison to Hamza and Aylmore dataset

The measured [Hamza and Aylmore, 1992] and simulated response of leaf water potential h_{leaf} to osmotic potential h_o at the root surface (Figure 4.2a), the concentration accumulation at the root surface over time (Figure 4.2b), and the relation of transpiration rate T_{act} (water uptake rate) to leaf water potential h_{leaf} (Figure 4.2c) are shown for different initial soil water salinities.

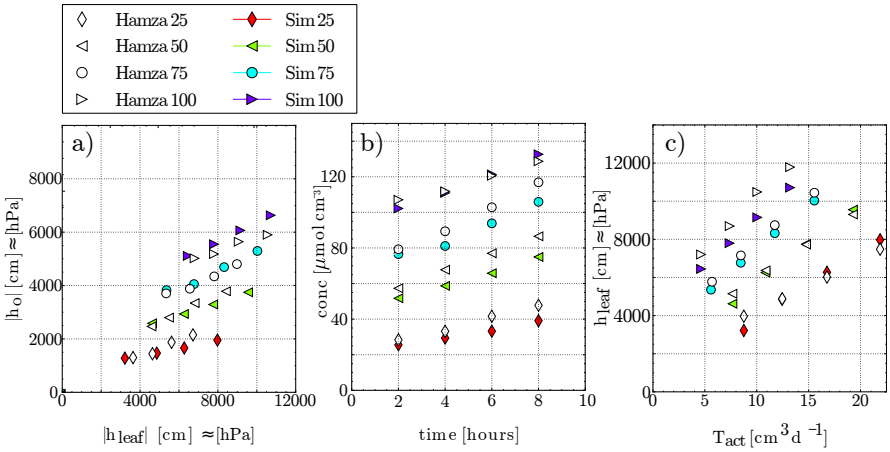

Figure 4.2: Comparison of simulated data (colored filled symbols) and measured data (open symbols) from Hamza and Aylmore [1992] for different initial salt concentrations (25, 50, 75 and 100 μmol cm^{-3}):
(a) leaf water potential h_{leaf} plotted against osmotic potential h_o at the root surface;
(b) concentration accumulation at the root surface over time;
(c) actual transpiration rate T_{act} plotted against h_{leaf};

The simulated concentration and osmotic potential values are in a good agreement with the experimental data, especially considering the fact that the input parameters and properties for soil and roots were imposed without any further adjustment. Slight differences may occur due to the sampling at different layers, which leads to concentration and osmotic potentials values at a single point at the root surface. In contrast, the simulated values are averaged values along the whole root profile.

Absolute values of simulated h_{leaf} slightly underestimated the measured data (not negative enough) for the treatments with higher concentrations (75 and 100 μmol cm^{-3}), but showed the same trend with osmotic potential, time, and actual transpiration rate as the measured data. In the model, the potential at the root collar was assumed to represent h_{leaf} (Figure 4.2c). The underestimation of the absolute leaf water potential might be due to the fact that we do not consider the potential loss in the stem. In addition, the relation of h_{leaf} and transpiration rate depends on the hydraulic conductivity of the plant root. Here, hydraulic properties were not measured and we assumed values from literature, which might not match exactly.

However, the comparison between measured and simulated data shows that the changes in h_{leaf} depend on the initial osmotic potential and that and that the changes of the salt concentration at the soil-root interface and the osmotic potential over time are well reproduced by the model simulations. In addition, the results imply that our assumptions of no osmotic adjustments and a constant reflection coefficient of $\sigma = 1$ were valid.

In Figure 4.3, the difference between h_{leaf} and $h_{int} + h_o$ ($\Delta h = h_{leaf} - h_{int} - h_o$) and the difference between h_{leaf} and h_{int} ($\Delta h_{leaf,m} = h_{leaf} - h$) are plotted against T_{act} for scenarios with a reflection coefficient of $\sigma = 1.0$ (legend - a), $\sigma = 0.5$ (legend - b) and $\sigma = 0.0$ (legend - c).

Figure 4.3 shows that the simulated difference of Δh versus T_{act} leads to a straight line through the origin, with a slope of K_{eff}, for all salt concentrations. The data of Hamza and Aylmore [1992] show also a straight line through the origin, but varies the slope for between treatment. This is because K_{eff} of the plant is different for each treatment.

Figure 4.3b shows $\Delta h_{leaf,m}$ plotted against T_{act} for $\sigma = 1.0$ together with the experimental data. In Figure 4.3c, simulated $\Delta h_{leaf,m}$ and T_{act} are plotted against each other for $\sigma = 0.5$ (dashed line) and for $\sigma = 0.0$ (dotted line). The deviations between measured and simulated $\Delta h_{leaf,m}$ versus T_{act} relations for $\sigma = 1.0$ (Figure 4.3b) are small when compared with the differences between simulated $\Delta h_{leaf,m}$-T_{act}-relations for other σ values ($\sigma = 0.5$ and $\sigma = 0.0$ in Figure 4.3c). For σ significantly smaller than 1.0, decreases due to smaller effects of the osmotic potential (Figure 4.3c, dashed line). Using a reflection coefficient of $\sigma = 0.0$ (Figure 4.3c, dotted line), the response to is similar for

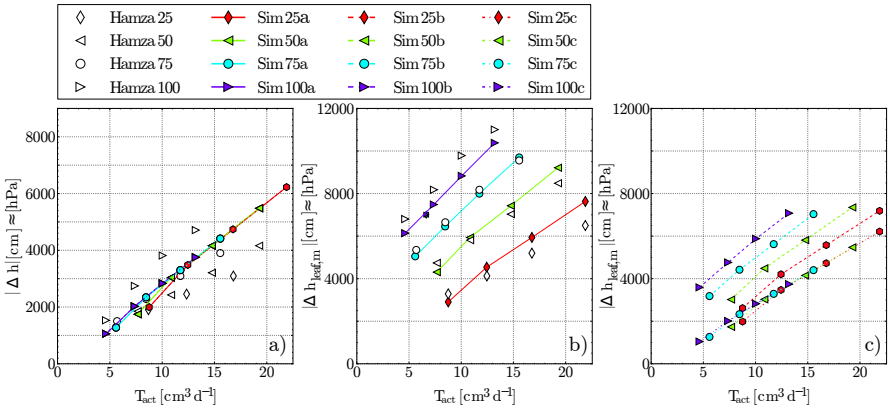

Figure 4.3: (a) Δh ($h_{leaf} - h_o - h_{int}$) plotted against T_{act} for $\sigma = 1.0$ and different initial salt concentrations (25, 50, 75 and 100 μmol cm^{-3}), open symbols are measured data from Hamza and Aylmore [1992], colored filled symbols connected by lines are simulation results
(b) Simulated (filled symbols connected by full lines) and measured data (open symbols): $\Delta h_{leaf,m}$ ($h_{leaf} - h_{int}$) plotted against T_{act} for $\sigma = 1.0$ (a, solid line)
(c) Simulated $\Delta h_{leaf,m}$ ($h_{leaf} - h_{int}$) plotted against T_{act} for $\sigma = 0.5$ (dashed line) and $\sigma = 0.0$ (dotted line)

all salt concentrations reflecting that the plant behavior is not affected anymore by the solute concentration levels around its roots.

4.4.2 Scenario 2: Simulated stress function with a single root

For this scenario, we imposed a constant potential transpiration rate to a single root located in a soil with different levels of solute concentration. At each time step, an actual transpiration rate and averaged or soil-root interface (osmotic, gravimetric and matrix) potentials were obtained.

Comparison with the model of Couvreur et al. [2012]

In Figure 4.4, the apparent plant stress response $\alpha = {}^{T_{act}}/_{T_{pot}}$ is plotted against the total potential H, the matrix potential and gravity potential components $h + z$, and the

osmotic potential h_o at the soil-root interface for the lowest transpiration rate, $T_{pot} = 1.0$ cm^3 d^{-1}, and for a broad range of initial concentrations.

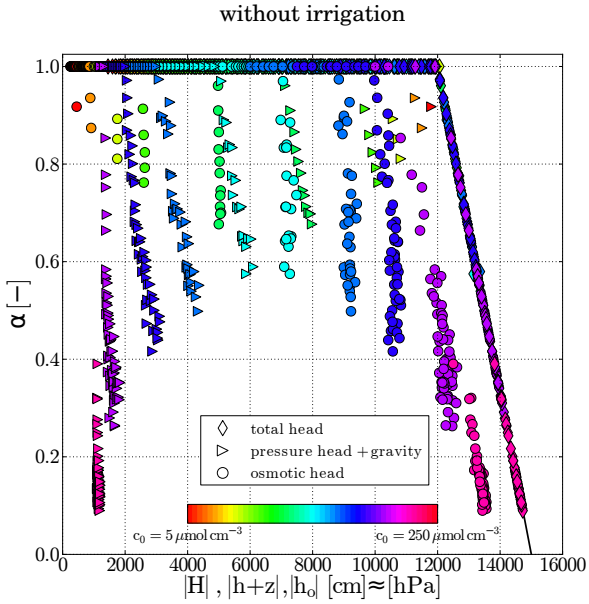

Figure 4.4: Transpiration reduction α vs. water potential at the soil-root interface. Comparison of the total potential $|H|$(diamond), matrix plus gravity potential , $|h+z|$ (triangle) and the osmotic potential $|h_o|$ (circle); results are shown for $T_{pot} = 1$ cm^3 d^{-1}. The colorbar represents the different initial salt concentrations. All potentials are SSF-weighted.

When the soil-root interface total water potential is used, the reduction of the transpiration rate is piecewise linear. It is important to note that neither the initial salt concentration nor the soil type (results not shown) control the shape of these curves. The obtained relation between transpiration rate and total matrix potential at the soil-root interface is identical to the relation proposed by Couvreur et al. [2012], which predicts the onset of stress based on the plant-felt total water potential and predicts a linear decrease of actual T_{act} with the plant-felt total water potential. Therefore, a correct evaluation of the root-felt water potential is a solution to get a mathematical relationship that depends only on T_{pot} and root properties.

It can be observed that reduction of the transpiration rate is induced at a very low local negative water potential (approx. −12000 cm for T_{pot} = 1 cm^3 d^{-1}) independently of the main component of the total potential (Figure 4.4). Whether the osmotic or the matrix component is predominant does not impact the stress onset, only the total water potential is important (given our hypothesis that there is no plant osmotic adjustment and $\sigma = 1$). This confirms the definition of the model of Couvreur et al. [2012] in which only the total potential is decisive. By comparing the osmotic and the matrix plus gravity potentials in Figure 4.4, it can be seen that both parts perfectly 'compensate' each other.

Comparing bulk and root-soil interface water potential

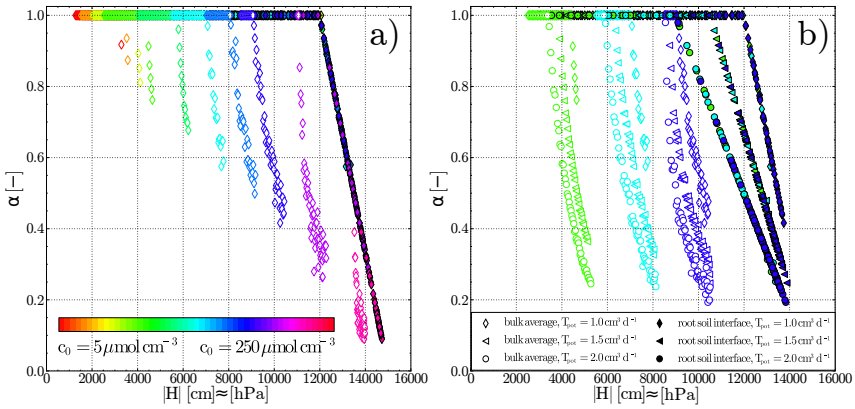

Figure 4.5: Transpiration reduction α vs. total water potential $|H|$ at the soil-root interface (filled symbols) and vs. total bulk soil water potential (open symbols); the color scale refers to the initial salt concentration in the soil (low concentration red – high concentration pink). All potentials are SSF-weighted.
(a) T_{pot} = 1.0 cm^3 d^{-1} and the whole considered initial salt concentration range
(b) three initial salt concentrations and three different transpiration rates (T_{pot} = 1.0, 1.5, 2.0 cm^3 d^{-1});

In Figure 4.5 the reduction functions are plotted either versus the total water potential at the soil-root interface or versus the total water potential of the bulk soil. For a given transpiration rate, the reduction function is clearly not a unique function of the total water potential of the bulk soil but depends strongly on the initial salt concentration or

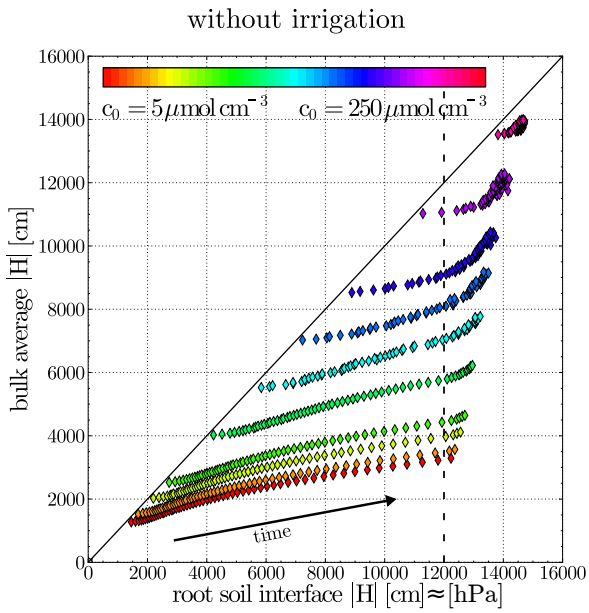

Figure 4.6: Average bulk soil total potential $|H|$ vs. total potential $|H|$ at the soil-root interface plotted for different initial concentrations (see colorbar) and $T_{pot} = 1$ cm^3 d^{-1}. All potentials are SSF-weighted.

osmotic potential. For lower salt concentrations (Figure 4.5a) onset of stress is reached for higher (lower in absolute value) bulk/averaged total water potentials (red - green symbols) than for higher salt concentrations (blue - violet symbols). For higher salt concentrations, the stress response curves obtained using bulk-averaged potentials and using potentials at the soil-root interface approach each other.

The onset of the reduction and the slope of the reduction function depend on the potential transpiration rate (compare Eq. (4.4) and Figure 4.5b). In addition, the transpiration rate affects the differences between bulk and soil-root interface stress functions (Figure 4.5b). A higher transpiration rate leads to a stress onset for less negative bulk soil matrix potentials than the matrix potentials at the soil-root interface.

Although local values of the water potential at the soil-root interface should be preferably used for stress functions, they are hardly measurable with current measurement devices. The discrepancy between local and bulk soil water potential is further investigated in Figure 4.6, where the total potential at the root-soil interface is plotted against the bulk average total potential. At the beginning of the simulation runs, the

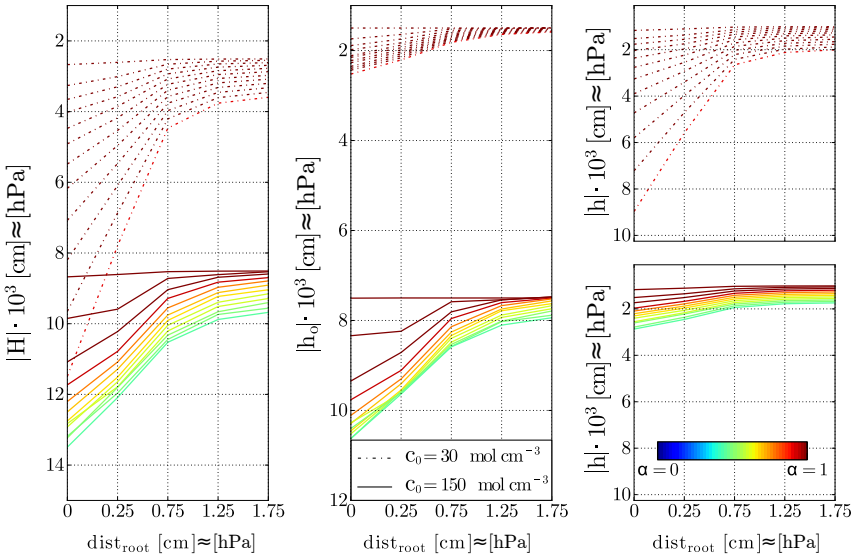

Figure 4.7: Distance plots of total potential $|H|$ (left), osmotic potential $|h_o|$ (middle), and matrix potential $|h|$ (right) versus distance from the root surface $dist_{root}$ at different times for the single root scenarios; initial concentration $c_{init} = 30$ μmol cm^{-3} (dotted line) and $c_{init} = 150$ μmol cm^{-3} (solid line); $T_{pot} = 1$ cm^3 d^{-1}. The color of each line indicates the transpiration reduction factor α calculated from the model simulations, transpiration decreases and the water potential gradients increase with time. All potentials are SSF-weighted.

solute and water distributions are uniform, leading to no differences between bulk and root surface potentials. With progressing simulation time, the gradients of osmotic and matrix potential are getting larger, leading to a larger discrepancy between bulk and root-soil interface potentials. It can be seen that the difference between bulk and root-soil interface water potentials becomes larger with smaller initial solute concentration (see Figure 4.6a) leading to larger discrepancies between bulk and local stress functions (Figure 4.5). When stress is reached (here −12000 cm at the soil-root interface, dashed line in Figure 4.6) the difference is not increasing further.

When comparing the gradients of the matrix and osmotic potentials that develop in the soil towards the soil-root interface during the simulated time period in the scenarios (Figure 4.7), the gradients in matrix potential that developed for low initial salt con-

centration, are much larger than the gradients in osmotic potential that developed for high initial salt concentration. The processes that lead to the development of these two different gradients are fundamentally different. For the matrix potential, the gradients are driving the water flow in the soil and, because of the non-linearity of the hydraulic conductivity, the gradients have to become very large to drive the same flow when the soil dries out. Osmotic potential gradients are not driving a flow, but are the result of an advective flow towards the soil-root interface that is countered by a back diffusion. The consequence of this difference in gradients between osmotic and matrix potentials is that the difference between soil-root interface total potential and bulk soil total potential depends on which of the components of the water potential (osmotic or matrix) is dominating. This implies that, although the relation between soil-root interface total potential and transpiration reduction α is not dependent on the contribution of osmotic and matrix potential to the total potential, the relation between bulk soil total potentials and transpiration reduction is.

Indeed, when the soil-root interface water potential depends mainly on solute accumulation around roots and on the matrix potential gradient linked to the transpiration rate, the bulk potential is mainly affected by the initial soil water potential and initial solute concentration. Increasing the initial salt concentration, the total bulk soil water potential is decreased and smaller salt accumulation (and thus smaller osmotic potential differences between bulk and interface) is needed to generate stress (see Figure 4.7). The total bulk water potential is then closer to the soil-root interface total water potential. On the opposite, when the initial salt concentration is low, the matrix potential is the major component of the total potential and larger differences exist between root interface and bulk soil matrix potential than for the osmotic potential.

4.4.3 Scenario 3: Extrapolation with a full root architecture

Scenario 2 investigated the sensitivity of the stress function to the definition of the water potential (at soil-root interface versus bulk) for a very simple root architecture. It is, however, to be expected that the difference between stress function defined in terms of local or bulk potentials will be a function of the root distribution, soil type, and transpiration. In this third scenario, we tested the behavior of the stress function with a bigger plant root architecture (Figure 4.1b). In this simulation, a sinusoidal day-night cycle of the potential transpiration rate was used. Therefore, according to Eq. (4.4), the relation between soil water potential and the reduction coefficient α is not unique anymore since it depends the potential transpiration rate T_{pot}. This dependency on the potential transpiration is also reported by experimental data [Groenveld et al., 2013]. In contrast, the relation Eq. (4.3), which links the actual transpiration rate T_{act} to the

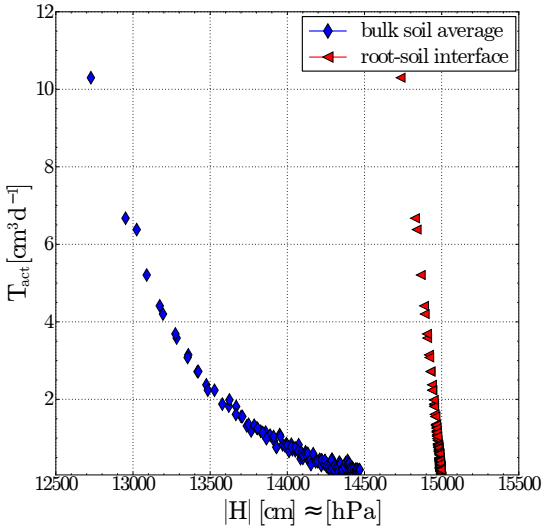

Figure 4.8: Actual transpiration T_{act} plotted against absolute total potential $|H|$ at the soil-root interface (triangles - red) and in the bulk soil (diamonds - blue) for the plant root architecture. All potentials are SSF-weighted.

water potential at the root-soil interface, does not depend on T_{pot} [Couvreur et al., 2012] and is used for this for this scenario (Figure 4.8).

Although the local stress function (with the water potential at the soil-root interface) is linear, using the bulk soil potential leads to a non-linear stress response (Figure 4.8), like in the single root simulations (Figure 4.5). The onset of stress also occurs at lower absolute total bulk water potentials than water potentials at the soil-root interface.

However, the difference in the response to bulk-average or to soil-root interface water potentials is not as large in the grassland setup as in the single root scenario. This is due to the fact that roots are spread in the whole soil column. Although there are still large matrix and osmotic potential gradients between root surface and the soil in these scenario (Figure 4.9), the average of water potential includes far more soil voxels close to roots compared to the single root setup. As compared to the single root scenario, this leads to a smaller shift between the bulk averaged and soil-root interface water potentials and shows that the shift between average and soil-root interface water potential depends on the root length density.

4.4.4 Comparison of simulation results with empirical stress functions

Using the averaged total water potential over the root-zone and over the complete simulation time period, as it is mostly done in for experimental data [Dudley and Shani, 2003], the transpiration reduction against the bulk soil average water potential is plotted in Figure 4.10a for the single root scenario. Here, each point corresponds with one initial concentration and initial potential transpiration rate.

For each potential transpiration rate, one global transpiration reduction response function can be observed (grey lines). Thus, the global transpiration reduction functions also depend on the potential transpiration rate, as the local transpiration reduction (Figure 4.10a - black lines). Note that this was also suggested in the original Feddes water stress function [Feddes et al., 1978].

For the two larger transpiration rates, stress is observed for very small salt concentration in the soil column over the whole simulation period. Hence, the matrix potential decrease over the time causes already a transpiration reduction and the stress in scenarios

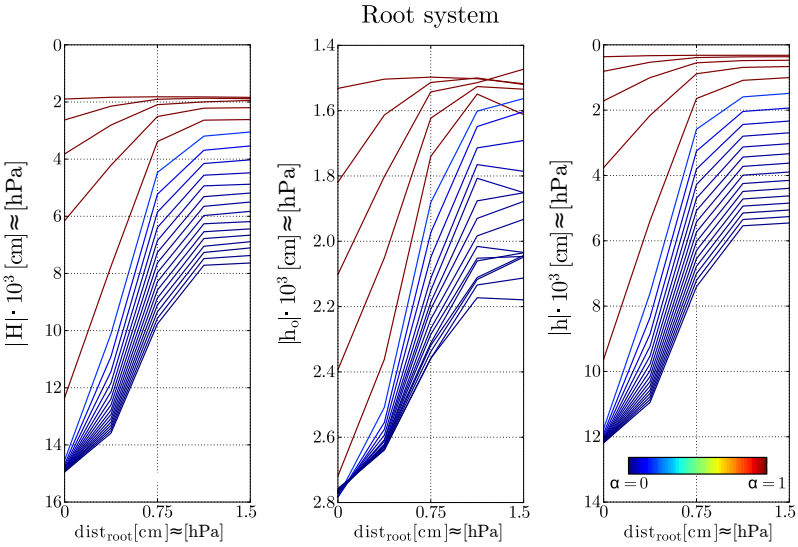

Figure 4.9: Total potential $|H|$, osmotic potential $|h_o|$, matrix potential $|h|$ vs. distance to the nearest root in the whole plant root structure. The transpiration reduction increases with time (smaller alpha value - see colorbar) and the water potential gradients increase with time. All potentials are SSF-weighted.

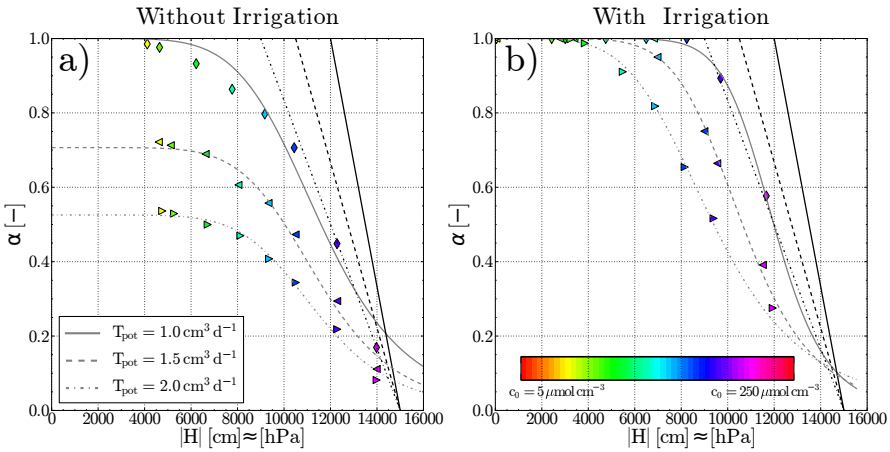

Figure 4.10: Time and space averaged transpiration reduction α plotted versus time and root zone averaged water potential, $|H|$, (filled symbols - grey lines), and instantaneous transpiration reduction plotted against the total water potential at the soil-root interface, $|H|$ (piecewise linear functions - black lines) for the transpiration rates T_{pot} = 1.0 cm^3 d^{-1} (solid line), 1.5 cm^3 d^{-1} (dashed line) and 2.0 cm^3 d^{-1} (dotted line) and for the scenario without irrigation (a) and with irrigation (b)

with salt is a combination of salt and water stress. For global transpiration reduction cause by salt only, the single root scenarios were run again, but with additional irrigation uniformly applied at the top soil boundary. The irrigation included salt concentration equal to the initial concentration in the soil and was defined as 2/3 of the T_{pot}. Figure 4.10b shows the global stress functions for these irrigation scenarios. Here, no stress is observed when the salt concentration is small.

The global transpiration reduction functions are similar to the *s*-shaped salt stress response function of van Genuchten and Hoffman [1984]

$$\alpha = \frac{T_{act}}{T_{pot}} = \frac{1}{1 + \left(\frac{h_o}{h_{o50}}\right)^p}, \tag{4.9}$$

where at h_{o50} is the value of h_o at which the yield, or the averaged actual transpiration rate, has declined by 50% an p is a shape parameter. This shows that the piecewise

linear local response to stress at every time point is very different from the whole plant response over a longer time period.

Which empirical stress function, which of the stress function parameters, and which approaches of combined stress function, fits best must be investigated in further studies. However, as already pointed out by Skaggs et al. [2006a], parameters that are obtained by fitting an empirical salt stress function to time-integrated measurement data should not be transferred to numerical models where the response to plant stress is applied at any point and time in the root zone. However, by using the piecewise linear stress function at the soil-root interface (Eq. (4.3), black lines in Figure 4.10) for every time step, a *s*-shape global stress response is obtained after averaging in time and space.

The relation between local and global transpiration respond depend, among others, on root length density and soil and root hydraulic parameters, and needs further investigation by analyzing the sensitivity to these parameters.

4.5 Summary and conclusion

A coupled numerical model that simulates flow and transport in the soil towards roots and water flow within the root system was used to simulate root water uptake in a drying saline soil with decreasing osmotic and matrix potentials. In a first scenario, the simulation results showed a good agreement with the observed data of Hamza and Aylmore [1992]. Their study provides experimental information about the relation between solute accumulation at a single root surface, the transpiration rate, and leaf water potential response. The good agreement between the measurements and simulation results indicated that the assumption of a perfectly selective permeable membrane, a negligible osmotic potential of the xylem sap, and no regulation of plant hydraulic properties were appropriate.

Second, two different simulation setups were used to investigate the transpiration response due to water and/or salt stress. The simulation results demonstrated that the actual transpiration rate under stress conditions is linearly related to the local total water potential (sum of matrix, gravimetric, and osmotic potentials) at the soil-root interface. This result supports the macroscopic model or type II model of Couvreur et al. [2012] which uses a linear relation between the transpiration rate and a weighted sum of local total water potentials.

However, local water potentials at the soil-root interface were found to differ considerably from bulk water potentials in the root zone. We showed that the differences between soil-root interface and bulk water potential decreased with increasing root density, increasing initial salt concentration, and decreasing transpiration rate. Furthermore, the differences

also depend on the soil hydraulic properties, which also change the gradient between soil-root interface and bulk water potential [Gardner, 1960; Schröder et al., 2008], but this was not investigated in this study.

Looking at the relation between the transpiration rate and bulk total water potential, we found that it depends on the composition of the bulk water potential and changes for the same bulk total water potential when the fraction of the bulk osmotic and matrix potentials changes. This is a result of different gradients in osmotic and matrix potential around a root. As a consequence, the effect of bulk matrix and osmotic potentials on water uptake is not additive in contrast to the effect of these potentials at the soil-root interface. Another noticeable difference is that, although stress relations are piecewise linear functions of the local soil-root interface potential, non-linear relations instead were obtained when spatially and temporally averaged bulk water potentials were related to temporally averaged transpiration rates.

The fact that the relation between bulk water potential and transpiration rate is influenced by several properties of the soil-plant system (e.g. hydraulic soil properties, root density, root conductivity), and states of the system (e.g. the relation depends on relative contribution of osmotic vs. matrix potentials to the total bulk water potential), makes that a relation that was parametrized for certain conditions is not directly transferable to other conditions. This may also explain the large noise that is often observed in experimentally derived relations [Homaee et al., 2002a]. When soil hydraulic properties are known and root distributions, salt and water contents are measured, simulations using a more detailed process model, which considers small scale variations of matrix potentials and osmotic potentials (or salt accumulation) around roots, may be used to derive root hydraulic properties by inverse modeling. In a subsequent step, simulation by such a detailed model may be used to derive stress relations in terms of bulk soil water potentials to other conditions.

In future work, the relation between local and global transpiration reduction must be analyzed, and the dependence of plant and soil parameters, e.g., root length density and soil and root hydraulic parameters, investigated. In addition, the simulations in this study focused on salt accumulation around plant roots and did not consider salt uptake. Nevertheless, some salts are taken up by plants and the amount and mechanisms of the salt uptake influence the concentration distribution around the root system [Schröder et al., 2012]. The influence of root salt uptake on transpiration reduction should be investigated. Furthermore, we assumed no osmotic adjustment. It should be noted that implementing such an adjustment in the model is straightforward. Root hydraulic properties, osmotic potential of the xylem sap, the reflection coefficient of the osmotic membrane σ can be made functions of external and internal conditions (e.g. water potentials). The problem appears in setting up experiments and measuring responses that can be used to validate and parametrize such functions. However, model simulations

may be useful to assess in a first step the sensitivity of the system to such adjustments. In a second step, simulations can be used to design experiments that can be used to parametrize adjustment functions.

Chapter 5

Three-dimensional measuring and modeling of a tracer transport in a planted soil column*

5.1 Introduction

Understanding solute movements in the vadose zone is crucial for managing soil and groundwater quality. Although the majority of our terrestrial environment is covered by vegetation, solute transport studies have mainly focused on bare soil in the last decades [e.g., Jury et al., 1976; Vanderborght et al., 1998; Vanderborght and Vereecken, 2007; Kasteel et al., 2009; Bechtold et al., 2012]. While our knowledge on the impact of soil types, boundary conditions, or spatial heterogeneity on solute transport has thus significantly progressed, the quantification of the effect of plants on solute is lagging behind.

In particular the impact of the heterogeneity generated by plant water uptake on solute transport has not been deeply studied. Models are available ranging from the single root scale [Gardner, 1960; de Jong van Lier et al., 2006] to whole root architecture models [Doussan et al., 1998, 2006; Javaux et al., 2008; Schneider et al., 2010] predicting soil water flow and root water uptake. Solute transport and uptake can be considered by coupling water flow and the convection-dispersion equation (CDE) with a sink for root solute uptake. Using these models, few studies exist though, which showed that root water and solute uptake distribution affect the water flow and solute distribution in the root zone, and the apparent dispersivity length [Jury et al., 1977; Russo et al., 1998; Vogeler et al., 2001; Schröder et al., 2012].

Although these studies investigated the impact of solutes on plants or the impact of nutrients on root growth at the plant scale, considering the soil plant system as a one-

*adapted from N. Schröder, M. Javaux, A. Pohlmeier, S. Haber-Pohlmeier, K. Huber, B. Steffen, H. Vereecken and J. Vanderborght. *in preparation*

dimensional (1D) system, there were almost no research on the quantification and modeling of solute and water uptake in function of the root architecture. The location and magnitude of solute and water uptake along the root system is thus still a matter of debate [Draye et al., 2010]. This is explained by the fact that direct, *in situ* monitoring of the uptake along the 3D root system architecture (RSA) is still difficult to achieve [Zarebanadkouki et al., 2012]. New methodologies for characterizing the effects of plant roots on solute movement are therefore needed.

Comparing simulation studies with measurement data is essential for the development of numerical models. Available data sets usually depict solute breakthrough curves (BTC) of leaching experiments [Gish and Jury, 1983] or depth average profiles of solute concentrations and water content [Vogeler et al., 2001]. These 1D data sets were compared to 1D model results. Dunbabin et al. [2002] compared a three-dimensional (3D) model to root growth and average nitrate uptake rates. However, spatial data showing concentration patterns and the influence of plant roots on the solute distribution are hardly available.

New 3D tomography systems like magnetic resonance imaging (MRI) [Rausch et al., 2005; Pohlmeier et al., 2008, 2009], X-ray tomography [Mairhofer et al., 2012] or neutron tomography [Esser et al., 2010; Zarebanadkouki et al., 2012] allow direct monitoring of 3D root architecture and/or the impact on water or solute distribution. Even if the uptake is not directly measurable, by monitoring the change of the solute concentration distributions and inverting it with a 3D model, the uptake distribution could be obtained. Tracer particles, which are not taken up by the plant roots, are transported to the plant roots and accumulate around them. Therefore, local root water uptake can be visualized. In addition, the horizontally averaged 1D concentration profile is directly linked to the root water uptake and [Schröder et al., 2012] and can be used to calculate an depth-averaged water sink distribution.

In this study, we aimed at comparing measured and simulated 3D data of a tracer experiment in order to assess the distribution and magnitude of the water uptake of a young lupine plant. The data were obtained by MRI, using appropriate measurement protocols that are able to differentiate between plant roots and soil. Thus, MRI provide high resolution 3D images of root growth, water uptake processes and root architecture structures [Pohlmeier et al., 2008, 2013; Stingaciu et al., 2013]. In addition, it has been shown that the contrast agent Gd-DPTA^{2-} (gadolinium-diethylenetriaminepentacetate) can be used as tracer to monitor solute movement in soil columns [Haber-Pohlmeier et al., 2010; Bechtold et al., 2011a]. The data collected this study, include root system architectures (RSAs) and solute distribution from MRI as well as irrigated, transpired and percolated water mass and solute concentration in the percolate as a function of time.

This experimental setup was simulated using a 3D high-resolution numerical model. This model is an extended version of the model R-SWMS [Javaux et al., 2008; Schröder et al., 2012] describing water and solute movement in the root zone, where the plant root architectures is resolved at the scale of single roots. This model offers the possibility to describe soil and root interaction processes in a more mechanistic manner avoiding empirical descriptions of root water uptake as a function of, for example, bulk water potential or root length density. The experimental data of the MRI setup are important for the calibration of the numerical model and are therefore compared to the simulation results. The combination of MRI data and the simulation model offers the prospect (1) to investigate the extensive effects of root architecture parameters on solute spreading, and (2) to obtain valuable information about plant hydraulic parameters.

5.2 Materials and methods

5.2.1 MRI tracer experiment

In the experimental setup (Figure 5.1), a two week old white lupine plant (*Lupinus albus* L.) was grown in a 10 cm high cylindrical column with an inner diameter of $d = 5$ cm. The column was filled with compacted, dry, sand (F31). The packing density was 1.57 g cm^{-3}. The seedling (1 day after germination in wet filter paper) was placed into the top of the sand and a 3 mm thick layer of coarse sand was filled on the upper surface in order to distribute the irrigated water. The plant was allowed to grow for one week at about half saturation. Then, the system was nearly saturated ($\theta = 0.36$).

A continuous irrigation rate of 1.47 cm d^{-1} (28.8 cm^3 d^{-1}) was applied uniformly at the top of the soil column by intervals of 5 min irrigation and 1 hr waiting time, since the pump had a lower limit of flow velocity. The transpiration rate of the plant was obtained by daily weighing of the soil column (see Figure 5.5). Over the measured period, a loss of 16.6 cm^3 per day was observed on average. The controlled outflow of the system ensures a quasi-steady-state condition during the measurement.

After the steady-state was reached (after two days), 1 μmol cm^{-3} Gd-DTPA^{2-} was added to the irrigation solution in a step function. Gd-DTPA^{2-} is chemically inert and behaves conservative in the sense that is does not adsorb at the sand matrix due to its negative charge. In addition, Gd-DTPA^{2-} reduces the longitudinal relaxation time of water and can be used to measure flow processes in soil by MRI [Haber-Pohlmeier et al., 2010]. The form of Gd^{3+} can be used as a diagnostic blocker of (stretch-activated) cation channels in plants [Demidchik et al., 2002], but is not expected to change root water uptake dynamics. The outflow solution at the bottom of the soil column was measured once per measurement day and the Gd concentration of the daily outflow was

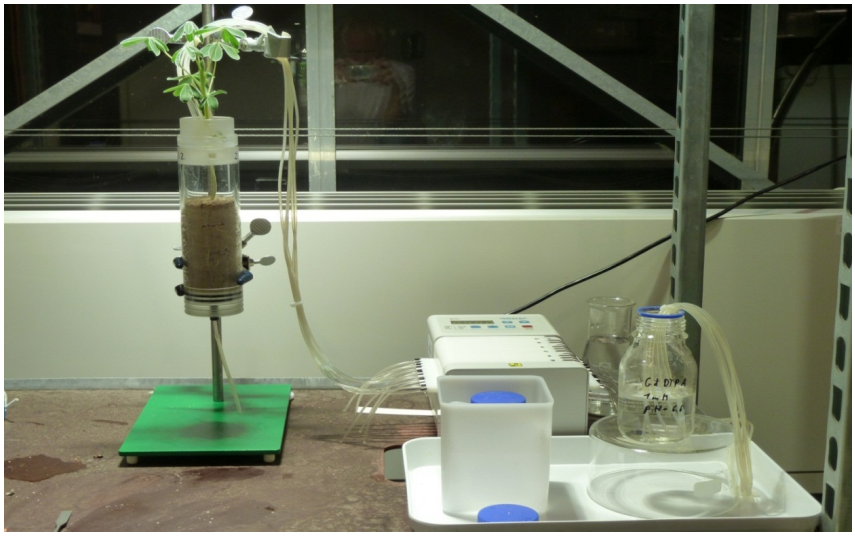

Figure 5.1: Setup of MRI tracer experiment: two week old lupine plant in soil column ($d = 5$ cm, fill-height $= 10$ cm)

detected. The measurement analysis of the column outflow detects Gd in all forms, but the stoichiometric ratio of Gd^{3+} and Gd-$DTPA^{2-}$ is 1 : 1. However, all measured Gd-concentrations in the outflow were Gd-$DTPA^{2-}$.

The tracer distribution inside the soil-root system was visualized over ten days by MRI. In this study, the used signal intensity in the spin-echo MRI sequence is described by

$$S(x,y,z) = S_0(x,y,z)\left[1 - \exp\left(-\frac{t_R}{T_1(x,y,z)}\right)\right]\exp\left(-\frac{n_E t_E}{T_2(x,y,z)}\right) \tag{5.1}$$

where S is the measured spatial signal intensity, S_0 is the extrapolated signal intensity for $t_E \to 0$ and for $t_R >> T1$, T_1 and T_2 are the effective longitudinal and transversal relaxation times, and t_R, n_E, and t_E are experimentally adjustable parameters, defined as repetition time, number of echoes, and echo time, respectively. For more details on the MRI measurement methodology and the used sequences, we refer to Haber-Pohlmeier et al. [2010]; Pohlmeier et al. [2008, 2009] and Stingaciu et al. [2013].

For the MRI measurements, a 4.7-T vertical ultra wide bore magnet (Magnex Scientific, UK) was used. This system uses a Varian gradient system of 300 mT/m and a 60-mm

RF birdcage coil (RAPID Biomedical GmbH, Germany) and is operated by VNMRJ software. Tracer sensitive data S were detected once every measurement day by a strongly T_1-weighted spin-echo multislice sequence with an echo time of $t_E = 3.4$ ms and a repetition time of $t_R = 0.15$ s [Haber-Pohlmeier et al., 2010]. Reference data (maximum signal intensity) S_{ref} was measured by setting $t_R >> T_1$ (see Eq. (5.1)).

The obtained slices were recorded in interleaved mode and vertical orientation. The field of view was 60 by 90 mm at a matrix size of $256(x)256(z)$ with z as vertical direction, resulting in a resolution of 0.23 x 0.35 mm, and a slice thickness of 2.1 mm (y-direction).

The used root system architecture was imaged at day 5 after measurement start using a T_2-weighted spin-echo multislice sequence with $t_E = 30$ ms and $t_R = 3$ s, 53 slices with a thickness of 1.0 mm in interleaved mode. Spatial resolution of the root system in x- and z-direction was 0.23 x 0.35 mm.

5.2.2 Post processing of the MRI data

Calibration curve

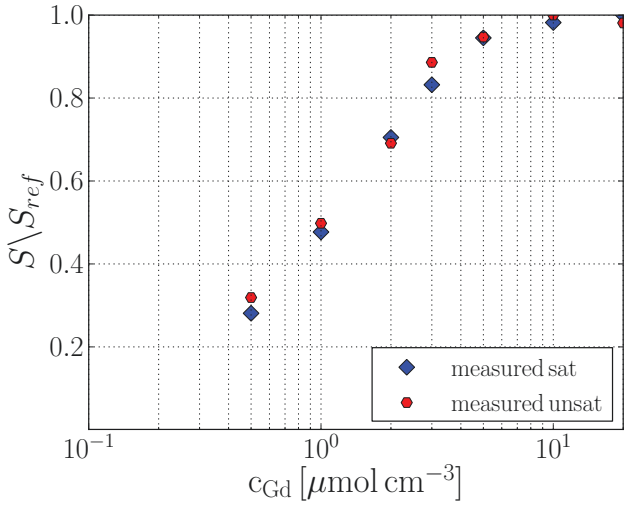

Figure 5.2: Calibration curve: relation between MRI signal S/S_{ref} to Gd-DTPA^{2-} concentration

The Gd-concentration c in the water solution measured with MRI is related to the signal intensity S normalized to the maximum signal intensity S_{ref}. This relationship between S/S_{ref} and c was calibrated by Haber-Pohlmeier et al. [2010] and is shown in Figure 5.2 for saturated and unsaturated (relative saturation of 52 %) samples. This calibration curve was fitted with an polynomial of 4th order and is used for concentrations between $c_{min} = 0.2$ μmol cm^{-3} (minimum) and $c_{max} = 4$ μmol cm^{-3} (maximum). Concentration values larger of this maximum or smaller than this minimum show not enough sensitivity to the normalized MRI signal. Therefore, all concentration values obtained by MRI values smaller than 0.2 μmol cm^{-3} were set to 0.0 μmol cm^{-3}. Larger than the maximal value were treated by the grid coarsening (see next section). The raw data S is available for all days, but S_{ref} could only be measured at day 2, 5, 6, 7, 8 and 9. For this reason, S/S_{ref} and thus the concentration maps are also only available for these days. For the comparison between measured and simulated concentration patterns, we focus on the the days where the tracer distribution is in a steady-state (days 6, 7, 8, and 9).

Grid coarsening

The comparison region of the MRI images was defined between $z = -1$ cm and $z = -7$ cm depth to avoid regions with boundary artifacts in the MRI data [Vaughan and Griffiths, 2012]. In addition, the data are transferred to a coarser grid, which was made up by 9 small scale voxels in the x-, 1 voxel in the y- and 6 voxels in the z-direction, so that a grid of 0.21x0.21x0.21 cm was obtained, similar to the simulation grid. The advantage of the coarser grid is an easier comparison between simulated an measured data and a faster run time for simulations.

We considered three alternative methods to derive the concentrations in voxels of the coarser grid. In the first two alternatives, concentrations were calculated from the MRI signals S/S_{ref} in the fine grid. If the calculated concentrations exceeded a threshold value of 4.0 μmol cm^{-3}, the small scale voxel concentration was blanked.

In the first method, the concentrations in the larger scale voxels were obtained from averaging the concentrations of the smaller voxels and for the four measurement times (day 6, 7, 8, 9). If the dataset of voxel concentrations that were averaged contained a blanked-out value, the larger scale and time averaged voxel concentration was blanked out as well. In the second method, the large scale voxels concentrations were obtained for a nearest neighbor interpolation.

In these two methods, the non-linearity of the calibration relation is properly accounted for to obtain averages of concentrations on a larger scale, which might be important when small scale variations of concentrations are present. On the other hand, also the noise on the MRI measurements is propagated in this non-linear calibration. This may

pose problems when the MRI signal is not very sensitive to concentration changes as is the case for higher concentrations.

Calibration relations were made from MRI signals measured in prepared soil samples with known and assumed uniform concentration distributions [Haber-Pohlmeier et al., 2010]. These calibrations were made on averaged voxels of approximately 1 x 1 cm^2, thereby deleting the noise of the higher resolution solute distribution. As a consequence, the noise on S/S_{ref} was averaged out to derive the calibration relation. Therefore, we considered a third method in which first S/S_{ref} were averaged in the coarser grid voxels. Then, we used averaged of the four measurement times (day 6, 7, 8, 9). Concentrations were subsequently derived from the averaged S/S_{ref} for the case $S/S_{ref} \leq 0.9$. Otherwise no voxel values were blanked out. Based on these three alternative coarser grid data, a noise analysis and a mass correction is performed on the data.

Measured and simulated concentration distributions are compared by 2D concentration planes obtained from the measured and coarsened MRI data are and 2D slices from the simulations. The 2D slices that are shown in the result sections are either x-z-planes at $y = 0$ cm between the depths $z = -1$ and $z = -7$ cm or xy-planes from the depth -2, -4 or -7 cm, as shown in Fig. 5.3.

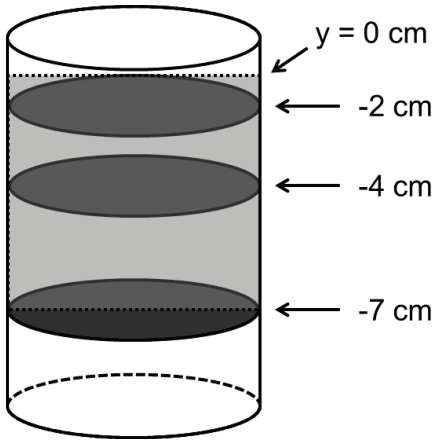

Figure 5.3: Two-dimensional x-z-slice from the middle of the soil column in the range of $z = -1$ and $z = -7$ cm, and x-y-slices from the depth -2, -4 and -7 cm

Noise analysis

The noise of the MRI data was analyzed from the measurement days 6 to 9. During these days, the concentration was supposed to be at steady-state and the spatial distribution of the tracer should, according to the model simulations and in agreement with the concentrations measured in the effluent, remain nearly constant. Each voxel is compared over theses days and the variation of the concentration is determined. This is done for all three different grids obtained by the coarsening (see section above) to additionally investigate the effect of the different grid coarsening methods.

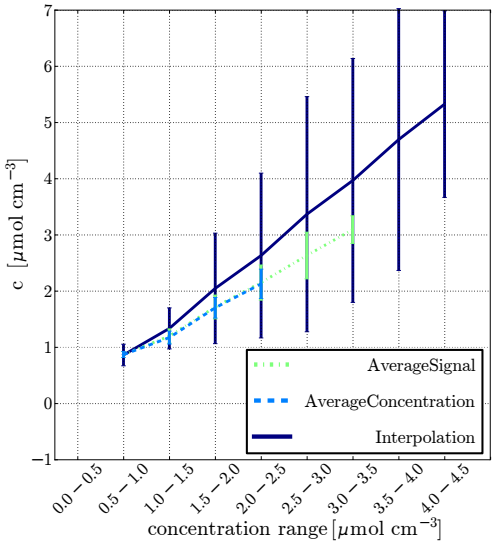

Figure 5.4: Mean, m, and standard deviation, s, (the concentration range represented by the vertical lines corresponds with the range [m-s,m+s]) of the MRI derived concentration in a voxel for three different averaging methods (days 6 to 9)

For each voxel of the coarsened MRI grid, the mean value and the standard deviation of the concentration between days 6 to 9 is plotted for different concentration classes (x-axis) in Figure 5.4 for the three coarsening methods (see Section 5.2.2).

When the concentrations or normalized signals of the high resolution MRI image are first averaged, the standard deviation of the concentrations of the coarsened MRI image is considerably smaller than for the case that the coarsened grid concentrations are derived

from an interpolation method. In the interpolation method, the value of the nearest voxel in the high resolution grid is used so that random variations between images taken at different times is not averaged out. The standard deviation increased with increasing concentration indicating that the uncertainty of the concentration estimates increases with the concentration. However, since we used a maximal threshold of 4 μmol cm^{-3}, the derived standard deviation decreased again when the mean voxel concentrations approaches this threshold.

Mass correction

The MRI data from day 6 to 9 are averaged to one three-dimensional data set for each coarsing method in order to reduce the noise of the images. This leads to three different averaged data sets on which a mass correction is applied. The mass correction was necessary since the MRI data underestimate the concentration values inside the soil column. Indeed the input concentration was $c_{init} = 1$ μmol cm^{-3}, and in principle, it is impossible to get soil region with a lower concentration than 1, after steady-state has been reached, as observed. However, regions with a lower concentration than 1 were found after steady-state has been reached, for example, at the top of the soil column. Since the signal sensitivity is decreasing with increasing concentration (see calibration curve Figure 5.2), larger error can be expected for soil areas with tracer accumulation and the solute mass measured by the MRI is underestimated. This underestimation of the data mass is independent of the data noise. The approach we used for the mass correction is the same for all three grid data:

1. blank out all (coarse) voxels that include an MRI voxel with concentration values larger 4 μmol cm^{-3} (averaged or interpolated concentration).

2. scale all non-blanked out voxel values with a factor 1.3 to obtain the input concentration of 1 μmol cm^{-3} at the upper boundary of the MRI scanned soil volume where tracer accumulation due to root water uptake has not occurred yet

3. set all blanked-out voxel to 4 μmol cm^{-3}

4. calculate the mass from the different averaged MRI data and compare to the mass from simulation results; the simulated mass $M_{sim} = 98$ μmol inside the soil-plant system was calculated from the simulation results between the depth -1 and -7 cm and is almost constant from day 6 to 9 in all simulation runs.

Calculation of the 1D sink term distribution

The one-dimensional sink term profile (in z-direction) is linked to the 1D averaged concentration profile. At a certain depth z, the concentration $c(z)$ depends on the cumulative water uptake between the top ($z = 0$ cm) and z. Therefore, the 1D sink term can be calculated from the averaged 1D concentration profiles obtained by MRI. We consider for this calculation again the depths between $z = -1$ cm and $z = -7$ cm to avoid boundary artifacts and therefore adapt the calculation of the sink term to this depth range. The sink term and the concentrations in this depth range are related as follows:

$$\frac{\int_{z=-1\,\mathrm{cm}}^{z} S_w(z')dz'}{\int_{z=-1\,\mathrm{cm}}^{z=-7\,\mathrm{cm}} S_w(z')dz'} = \frac{1 - \frac{c(z=-1\,\mathrm{cm})}{c(z)}}{1 - \frac{c(z=-1\,\mathrm{cm})}{c(z=-7\,\mathrm{cm})}}, \tag{5.2}$$

where $S_w(z)$ is the 1D water sink term at a certain depth z. The normalized water sink term S'_w is given by

$$S'_w(z) = \frac{S_w(z)}{\int_{z=-1\,\mathrm{cm}}^{z=-7\,\mathrm{cm}} S_w(z')dz'} \tag{5.3}$$

and with this definition, the normalized 1D water sink can be calculated from the averaged 1D concentration as

$$S'(z + \Delta z/2) = \left(\frac{1 - \frac{c(z=-1\,\mathrm{cm})}{c(z+\Delta z)}}{1 - \frac{c(z=-1\,\mathrm{cm})}{c(z=-7\,\mathrm{cm})}} - \frac{1 - \frac{c(z=-1\,\mathrm{cm})}{c(z)}}{1 - \frac{c(z=-1\,\mathrm{cm})}{c(z=-7\,\mathrm{cm})}} \right) / \Delta z. \tag{5.4}$$

The averaged 1D concentration $c(z)$ should increase with depth in order to avoid negative sink terms. We applied this to the 1D concentration profile obtained by the MRI data.

5.2.3 Tracer uptake by plant roots

After the experiment, the Gd-concentration in the whole plant root system, plant stem, and plant leaves were analyzed by inductively coupled plasma mass spectrometry (ICP-MS). Over all plant parts, less than 2 % of the input Gd-mass was found. Hence, no solute uptake of the tracer was assumed and defined during the simulation runs.

5.2.4 Water flow and tracer transport modeling

Water flow was simulated with the model R-SWMS [Javaux et al., 2008], which couples transient soil water flow, described by Richards equation [Richards, 1931], with a plant architecture based root flow model [Doussan et al., 1998]. Tracer movement was described by the convection-dispersion equation (CDE) and solved by a particle tracking algorithm [Bechtold et al., 2011b; Schröder et al., 2012]. While the water flow part of the simulations involved root water uptake and water flow inside the root architecture system, no solute root uptake or tracer movement inside the roots was assumed since only less than 2 % of the input Gd-mass was found inside the plant (see section above).

Table 5.1: Sand (F31) parameters for Mualem-van Genuchten expression

θ_r [−]	θ_s [−]	a [cm^{-1}]	n [−]	K_s [cm d^{-1}]	l [−]
0.005	0.41	0.03	3.6	647	0.5

The simulation setup was defined analog to the experimental setup of the MRI measurements. The soil geometry is a 10 cm high cylindrical column with an inner diameter of $d = 5$ cm, which was represented by a 3D regular grid with 0.2 cm spacing. The soil hydraulic relationships of $\theta(h)$ and $\mathbf{K}(h)$ of the sandy soil (FH31, Pohlmeier et al. [2009]) were expressed by the Mualem-van Genuchten parametric expressions [van Genuchten, 1980] with the parameters given in Table 5.1. The longitudinal dispersivity length α_L was set to the mean grain size $\alpha_L = 0.035$ cm and the transversal dispersivity length α_T to $1/10$ of α_L, which are typical values reported for saturated unconsolidated homogenous porous media. The diffusion coefficient D_W of Gd-DTPA^{2-} was assumed to be 0.1 cm^2 d^{-1} and was multiplied by the tortuosity factor [Millington and Quirk, 1961].

The top boundary condition of the continuous irrigation of 1.47 cm d^{-1} with 1 μmol cm^{-3} Gd-DTPA^{2-} in the solution was applied uniformly on the top area of the cylinder (radius = 2.5 cm). For the lower boundary, the measured outflow data was used (Figure 5.5). A homogeneous soil water content was set to $\theta = 0.36$ (90 % initial saturation) at the start of the simulation.

5.2.5 Root architectures

Following the experiment, a manual 3D reconstruction of the root architecture was made [Stingaciu et al., 2013]. A 3D virtual reality system called PI-casso was used, which is operated by the VISTA software [Assenmacher and Kuhlen, 2010] at Jülich Supercomputing Centre (JSC), Forschungszentrum Jülich GmbH. The device is essentially an

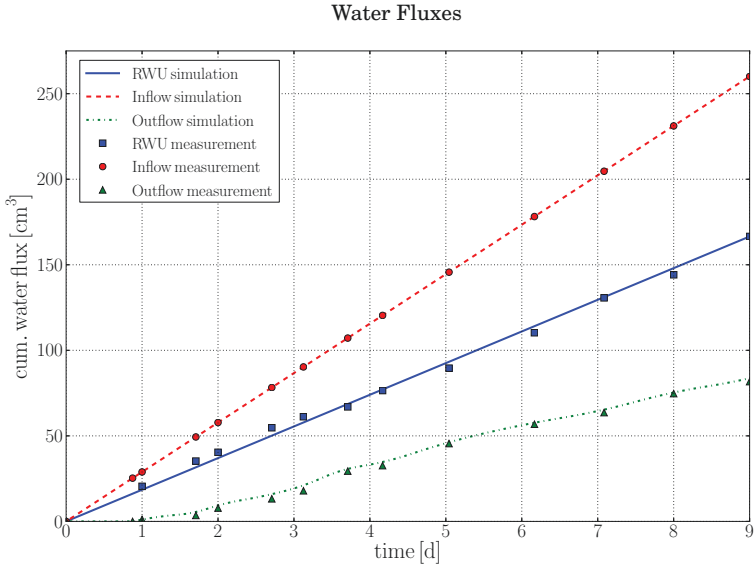

Figure 5.5: Simulated and monitored water flows in and out of the soil column; input irrigation at the top (red), outflow at the bottom (green), and root water uptake (transpiration rate) by the plant in the middle (blue)

interactive IMAX system that allows displaying and manually redrawing the root system architecture (RSA) in a virtual 3D environment. This method provides the root architecture from the MRI measurements as a hierarchical tree structure, which can be stored and later transformed to ASCII format [Wienke, 2009], and used as input for the R-SWMS model. The ASCII file contains information of the spatial coordinates (x, y, z) of each root node, the IDs of the node, the branching order, the surface area of each root segment, the length of the root segment, and its mass. These parameters are needed for the simulations of root water uptake [Javaux et al., 2008] and solute movement in soil [Schröder et al., 2012].

Since the MRI had a field of view of 60 x 90 mm and matrix size of 256 x 256, which define a resolution of 0.23 x 0.35 mm, fine roots that are smaller than the MRI resolution are missing. In addition, the MRI root structure data used was from day 5 of the measurement period, and afterwards, new, smaller roots might have emerged. For this reason, the root growth module from R-SWMS [Somma et al., 1998] was used to grow additional branches onto the measured root structure.

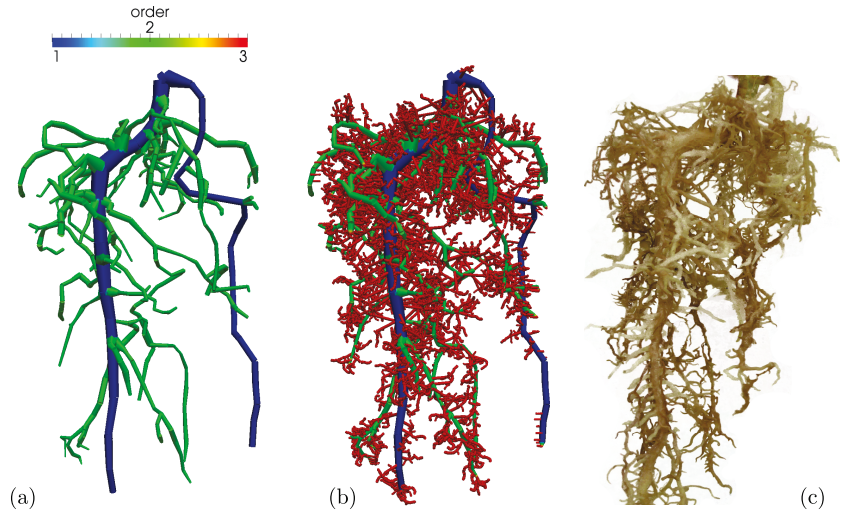

Figure 5.6: Basic manually reconstructed RSA (a), basic RSA with additional branches (b) and original structure, excavated after the experiment (c); root branching order: order 1 (blue), order 2 (green), order 3 (red);

Root growth started from the RSA obtained from the PI-casso system (basic root architecture, further referred to RSA (a), Figure 5.6a). In the first step, root branches that were assumed to have a similar age and similar root diameters were set to the same branching order. The roots of the original RSA obtained from the manual reconstruction were defined to be of branching order 1 for the two thickest root branches (blue in Figure 5.6a) and of order 2 for all other lateral root branches (green in Figure 5.6a).

With the known age of the measured RSA (a), a linear growth model was applied and each segment was allocated with an age. In a next step, initiation points for branching were defined along the roots considering a branching distance of 0.5 cm that were obtained from the unearthed root system after the experiment (Figure 5.6c). The previously measured RSA (a) was fixated and no further elongation was applied to roots with the order smaller than or equal to 2: only branches were added to the basic RSA (further referred to RSA (b), Figure 5.6b).

The applied root growth module consists of two stages. Stage one is the directional growth, which is dependent on predefined preferential growth angles and branching distances. Root tortuosity can be adjusted by varying the root growth time-step size;

the smaller the time-step, the more tortuous the roots will be. In the second stage, root elongation and root diameter as a function of local soil strength are defined. Branching order for all additional finer root branches was set to 3 (red in Figure 5.6b).

The validation of this growth adaption was by eye only (Figure 5.6c), as no surface measurements were conducted on the excavated root.

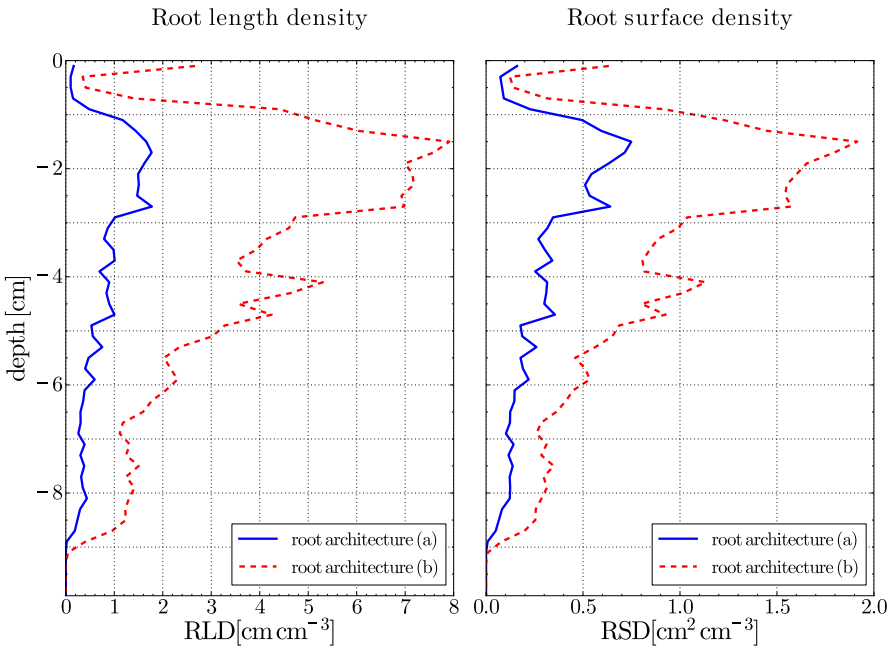

Figure 5.7: Root length density (RLD) and root surface density (RSD) of the basic RSA (a) and the RSA with additional branches (b)

Figure 5.6 shows the obtained RSA from the PI-casso system (RSA (a)) and the RSA with the additional branches (RSA (b)). The added, finer roots change the root architecture completely, as can be seen by comparing the root length density (RLD) and the root surface density (RSD) of both root system architectures (Figure 5.7). Especially in the upper root zone ($z = -1$ to $z = -3$ cm depth), the increase of RLD and RSD is very large. Since root water uptake is related to the spatial length and surface distribution of a RSA, we expect that the additional finer roots, if they take up water, have a large impact on the 3D water sink term and the velocity distribution, and consequently on the solute spreading.

Both root system architectures are used and compared in the numerical simulations. The objective of this comparison is to investigate the effect of the finer roots (branching order 3) on solute spreading, which depends on the root water uptake. The finer roots can clearly be seen in Figure 5.6c, but could not be measured by MRI due to too low resolution. However, if these finer roots do not have developed xylem vessels (which is true for young roots), they could be unable to extract water.

By comparing the two root architectures in different simulation runs, the model results will show the sensitivity of root water uptake and solute spreading in the presence of these finer roots.

5.2.6 Scenario analysis

For each of the RSAs, four simulation scenarios with different hydraulic parameters accounting for the different root orders were run (see Table 5.2) in order to investigate their influence on solute spreading:

(A) constant radial conductivity K_r^* and constant axial root conductance K_x

(B) constant radial conductivity K_r^* and varying axial root conductance K_x by root order

(C) varying radial conductivity K_r^* by root order and constant axial root conductance K_x

(D) varying radial conductivity K_r^* and varying axial root conductance K_x by root order

Note that for the basic root structure RSA (a), only root segments with order 1 and 2 are defined. Hydraulic root parameters for lupine are used from Doussan et al. [2006] and varied in the same order of magnitude. The transpiration boundary condition was constant for both RSAs in all simulation runs and set to $T_{pot} = 16.6$ cm^3 d^{-1} in accordance with the experimental setup.

5.3 Results

5.3.1 Modeled and observed breakthrough curve at the outlet

The collected samples at the column outflow ($z = -10$ cm) are compared to the simulated results in Figure 5.8. Here, the shaded area contains the breakthrough curves (BTCs) at $z = -10$ cm of all simulation scenarios (A, B, C, D, RSA (a) - dark-grey,

Table 5.2: Root hydraulic parameters for different simulation scenarios

Scenario	A	B	C	D
	K_x [cm^4 d^{-1} cm^{-1}]			
Order 1	0.2592	0.2592	0.2592	0.2592
Order 2	0.2592	0.0173	0.2592	0.0173
Order 3[a]	0.2592	0.0069	0.2592	0.0069
	K_r^* [cm d^{-1} cm^{-1}]			
Order 1	0.000864	0.000864	0.0000864	0.0000864
Order 2	0.000864	0.000864	0.0008640	0.0008640
Order 3[a]	0.000864	0.000864	0.0043200	0.0043200

[a]only for RSA with additional smaller root branches (RSA (b))

RSA (b) - light-grey). The solid black line is the mean value of all numerical data with RSA (a) and the dashed black line is the mean for RSA (b). Synthetic and experimental data are in a good agreement for all simulation runs, where the BTC from the RSA (b) fits slightly better compared to the BTC from RSA (a). The differences of numerical BTCs between the two root architecture systems are small and mainly in the error range of the measured data. The variation within the four scenarios is more pronounced for the simulation runs with RSA (b), where the different parametrization of the roots lead to more variation to the shape of the BTC. This variation caused by the additional finer roots and their parametrization affects more the slope of the BTC than the reached equilibrium concentration level. The reason for this is that the plant roots affect the flow velocity and the flow path of the solute tracer differently depending on their uptake distribution. However, the equilibrium concentration level of a BTC depends on the total root water uptake between $z = 0$ cm and $z = -10$ cm depth (if the tracer is not taken up by the plant roots). Since the root zone ends at $z = -9$ cm and the transpiration rate for all scenarios is the same, the concentration level is equal for all simulation runs.

5.3.2 Solute distribution patterns

Figure 5.9 shows the spatial concentration patterns in x-z- and in x-y-direction. The x-z-plane is from the middle of the soil column and the x-y-planes from the depth -2, -4 and -7 cm. The top row corresponds to the coarsening with the interpolation method, in the middle row, the concentration c was averaged, and in the bottom row, the signal

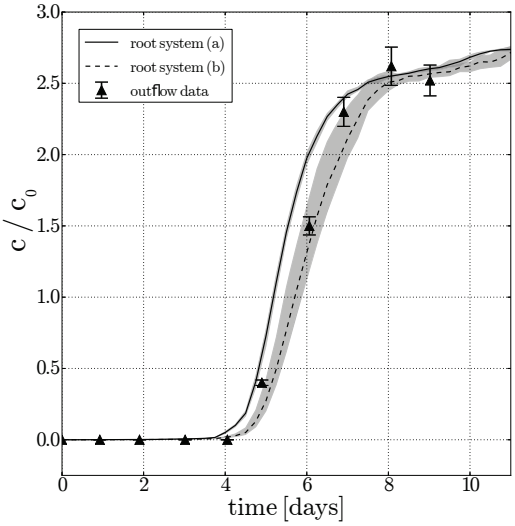

Figure 5.8: Simulated and monitored breakthrough curves at the column bottom ($z = -10$ cm) for root architecture systems (a) and (b); the dark-grey envelop correspond to all four simulation scenarios with RSA (a), the light-grey to all four simulation scenarios with RSA (b)

S/S_{ref} was averaged to obtain a similar grid size compared to the simulation runs and to smooth out the noise (see Section 5.2.2).

The tap root and a few laterals can be observed in dark blue, corresponding to $c = 0$ μmol cm^{-3} concentration (no uptake). As expected from the theory (see Fig. 9 in Schröder et al. [2012]), tracer enrichment, defined as concentration values higher than the input concentration of $c_{init} = 1$ μmol cm^{-3}, can be seen around the taproot mainly, and some laterals. In addition, though, high solute accumulation occurred also at the left boundary of the soil column. This enrichment occurred from day 5 on, but then decreased again with time (single day MRI data not shown).

The estimated mass from the simulation between -1 and -7 cm depth was $M_{sim} \approx 98$ μmol cm^{-3}. This value was similar between all simulation runs (scenarios defined in Section 5.2.6). In Figure 5.9 it can be seen that the MRI data obtained with the concentration-averaging method contains much more voxels set to 4 μmol cm^{-3} com-

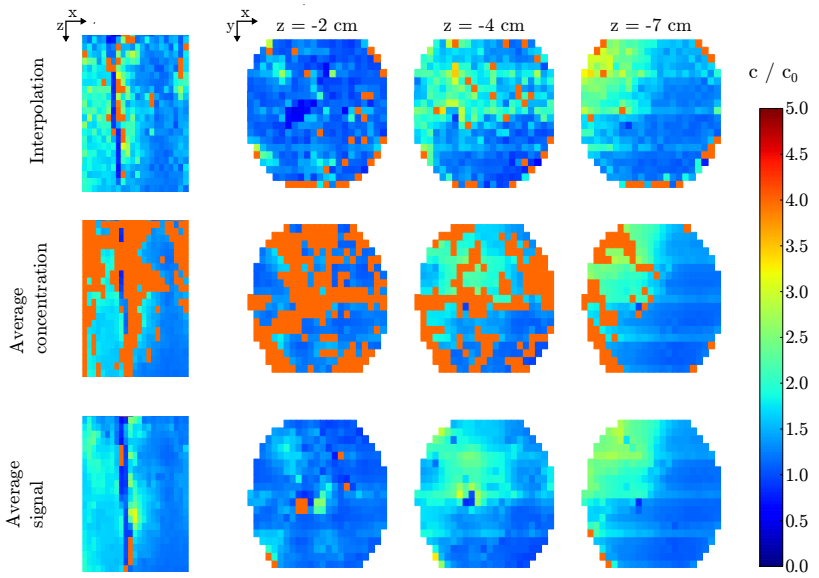

Figure 5.9: Two-dimensional x-z-slice from the middle of the soil column and x-y-slices from the depth -2, -4 and -7 cm of the solute MRI data; top row - interpolation method, middle row - concentration c averaged, bottom row - signal S/S_{ref} averaged

pared to the other two methods. Therefore, the obtained mass from these concentration-averaged MRI data is closer to the one from the simulation ($M_{avC} \approx 93$ μmol cm^{-3}). Contrary, less voxels with large values can be found by the interpolation and the signal-averaging method and thus less mass could be calculated from these data (signal-averaging: $M_{avS} \approx 58$ μmol cm^{-3}, interpolation: $M_{Int} \approx 65$ μmol cm^{-3}).

The pattens that are obtained by the data analysis and shown in Figure 5.9 are compared to the simulation results from both RSAs (a) and (b). Figure 5.10 shows the x-z-planes from the middle of the soil column for both RSAs and all four simulation scenarios (A,B,C,D), Figure 5.11 and Figure 5.12 show the x-y-planes from the depth -2, -4 and -7 cm for the RSA (a) and RSA (b), respectively, again for all for scenarios (A,B,C,D). All slices are from day 9 - at that time the steady-state was reached.

The spatial solute distributions leading to the very similar BTCs (Figure 5.8) are not unique and depend strongly on the hydraulic plant parameters. In all simulation runs, a high root water uptake spot is created by the plant in the upper soil part between

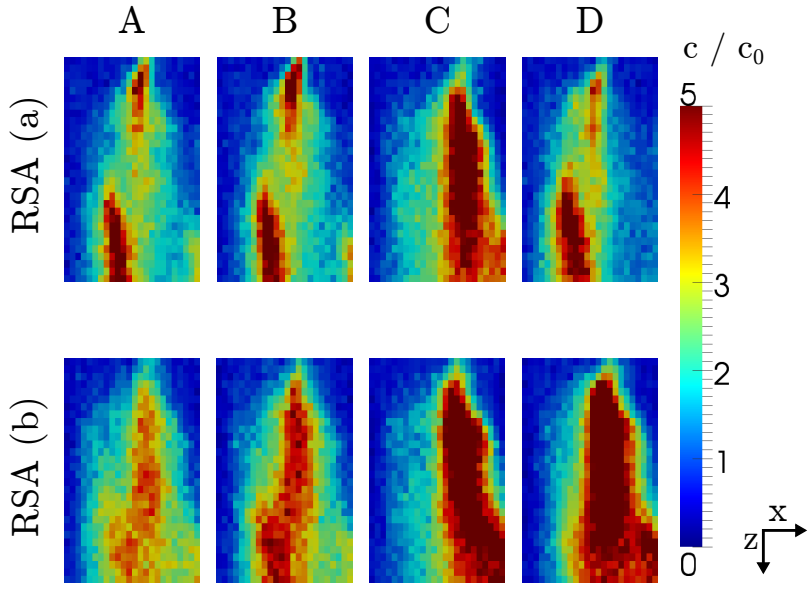

Figure 5.10: Two-dimensional x-t-slices of the simulated solute distribution in the middle of the soil column ($y = 0$) from day 9 (steady-state) for the RSAs (a) and (b) and all simulation scenarios (A, B, C, D)

$z = -1$ cm and $z = -3$ cm (compare also Figure 5.14) just below the turn of the taproot (Figure 5.6). This leads to a high tracer accumulation in this region and causes below this spot a solute 'shadow', which is a solute plume with higher concentrations downstream form the location where high water uptake and therefore strong solute concentration occurs. The amount of the tracer accumulation there and the shapes of the shadow are different between the two RSAs and depend also on the hydraulic plant parameters, which lead to different water uptake behaviors. These 3D root water uptake distributions spread the solutes differently, cause additional smaller spots of concentration accumulation in lower soil layers, and thus create different solute patterns. The solute accumulation can be also seen in the MRI data, again just below the turn of the taproot, but the concentration values are not as large as obtained by the simulations.

Except for the solute accumulation below the taproot, the simulated and monitored concentration patterns are not in a good agreement, no matter which interpolation or averaging methods were used (Figure 5.9). For example, a tracer accumulation at the

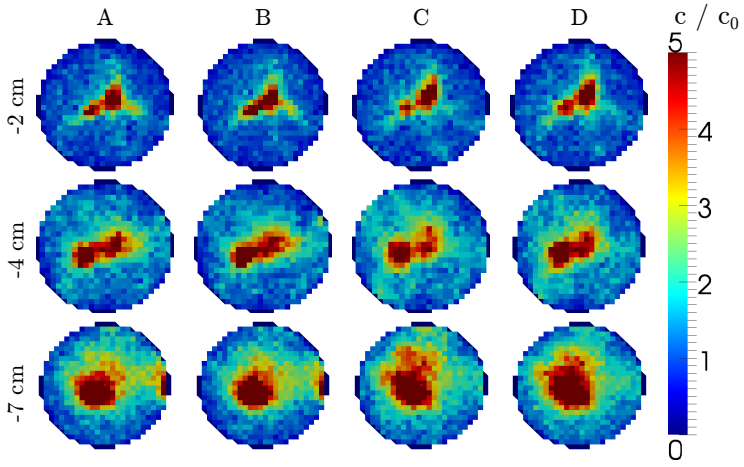

Figure 5.11: Two-dimensional x-y-slices of the simulated solute distribution from the depth -2, -4 and -7 cm for the RSA (a) and all scenarios (A, B, C, D) at day 9

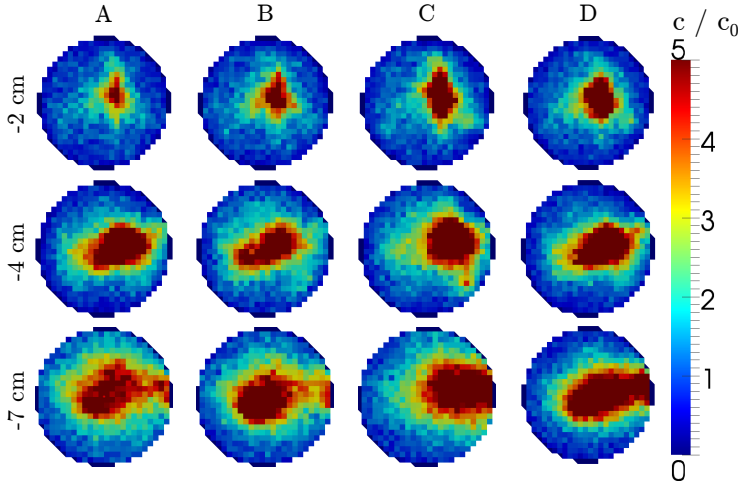

Figure 5.12: Two-dimensional x-y-slices of the simulated solute distribution from the depth -2, -4 and -7 cm for the RSA (b) and all scenarios (A, B, C, D) at day 9

left soil column boundary, measured by MRI, could not be obtained by any simulation run. In addition, the typical solute shadow effects, created by water sink locations close to the column top and observed in all simulation runs, cannot be seen in the MRI data. Finally, the maximal simulated local concentration values in a soil voxel are much larger than in the experimental local concentration values obtained by MRI. This could not be compensated by the mass correction and the high concentration gradients could not be reached. Reasons for the mismatching and possible solutions are discussed in Section 5.4. However, the differences in simulated concentration patterns between the different root architectures are after all not so large when compared with the uncertainty of the MRI derived concentration patterns.

5.3.3 Concentration depth profiles

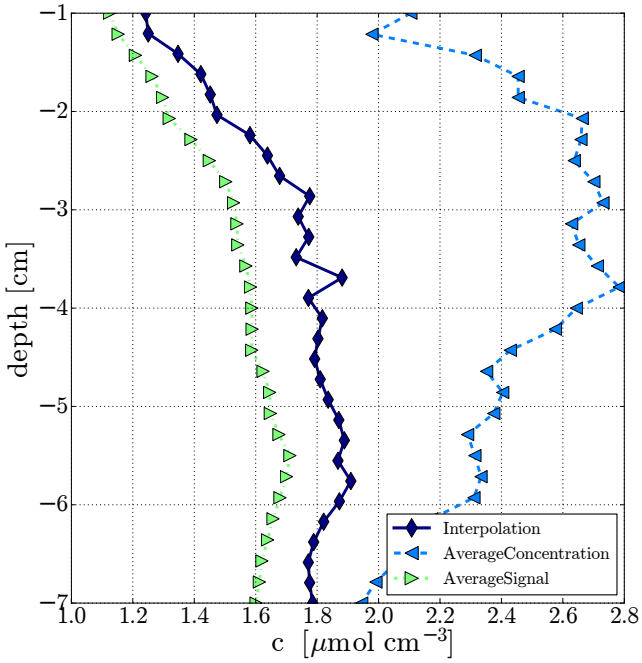

Figure 5.13: 1D observed concentration profiles per depths for the coarsen MRI data: signal-averaged (left), concentration-interpolation (middle) and concentration-averaged (right)

The 1D averaged concentration profiles from the three coarsen MRI data (Figure 5.9) are shown in Figure 5.13. For the interpolation and the signal averaging method, a mostly increasing and smooth concentration profile is obtained. However, the expected concentration value at -7 cm depth is $c \approx 2.8$ μmol cm^{-3} (see Fig. 5.8), but the missing tracer mass in both methods lead to too low concentration values. The concentration averaging method represents the expected mass inside the soil column better, thus the obtained 1D concentration values are larger. The profile is, however, more noisy and decreasing from -4 cm with depth, which is physically not possible when not tracer is taken up by the plant.

5.3.4 Determination of the water sink distribution

The 1D sink term profile (in z-direction) is linked to the 1D averaged concentration profile (Fig. 5.13) and can be calculated from it (see Section 5.2.2). This is done for the averaged MRI data obtained the three different averaging methods and the obtained normalized 1D water sink is plotted against depth in Fig. 5.14a (interpolation method), Fig. 5.14b (average concentration method) and Fig. 5.14c (average signal method). These 1D water sink profiles are compared to 1D averaged water sink term distributions from all simulation runs, given in Figure 5.14d.

In the sink profiles obtained from interpolation (Fig. 5.14a) and the average-signal method (Fig. 5.14c) the most water uptake occurs between depth -1 and -3 cm, similar to the the simulation results (Fig. 5.14d). In addition, a small decrease of the sink profile at -2 cm can be seen for these methods and in the simulations results, which leads to a similar shape of the root water uptake profiles at these soil layers. At lower depth (-4 until -7 cm) negative sink values are obtained from the MRI data due to an decrease in the concentration depth profiles (Fig. 5.13). However, the obtained 1D water sink values are again too low because of the missing mass obtained by the averaging methods.

The sink profile obtained by the averaging-concentration data (Fig. 5.14b) is mainly negative due to the large decreasing 1D concentration profile (Fig. 5.13) and has no similarity with the simulation results.

In the obtained sink profiles from the simulations, the additional finer roots of RSA (b) lead to higher root water uptake in the upper soil and to less water uptake in the lower soil layers compared to the basic RSA (a). This effect is more visible for the scenarios C and D where the radial conductivity K_r^* varied with root order and smaller roots were parametrized with larger values of K_r^*. In contrast, the lowest water uptake in the upper and maximal uptake in the lower soil layers was obtained with RSA (a) and scenario A and B, where K_r^* was defined constant.

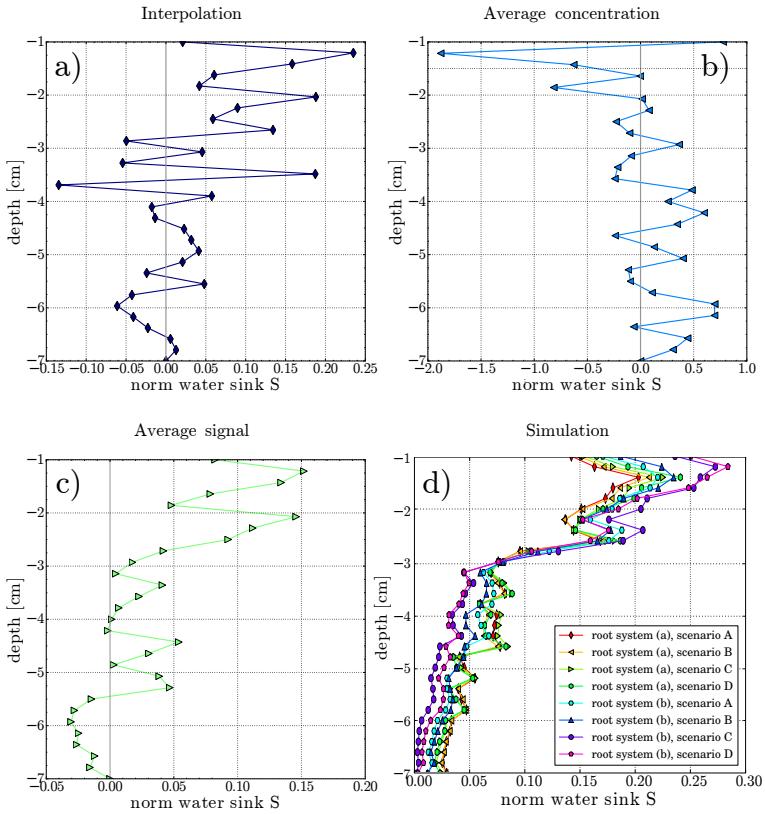

Figure 5.14: Normalized water sink term 1D-depth distribution calculated from the averaged MRI data by the three different averaging methods: (a) interpolation method, (b) average concentration method, (c) average signal method.
(d) Normalized water sink term 1D-depth distribution from all simulation runs (scenarios A, B, C, D, and RSAs (a) and (b)

Although the different scenarios show high variability in the two-dimensional concentration patterns (Figure 5.10, Figure 5.11 and Figure 5.12), the difference in terms of the 1D depth water sink profile (horizontally averaged) is small (Figure 5.14) considering the noise in the MRI data. This emphasizes the potential of experimental 3D tracer images for discriminating root properties.

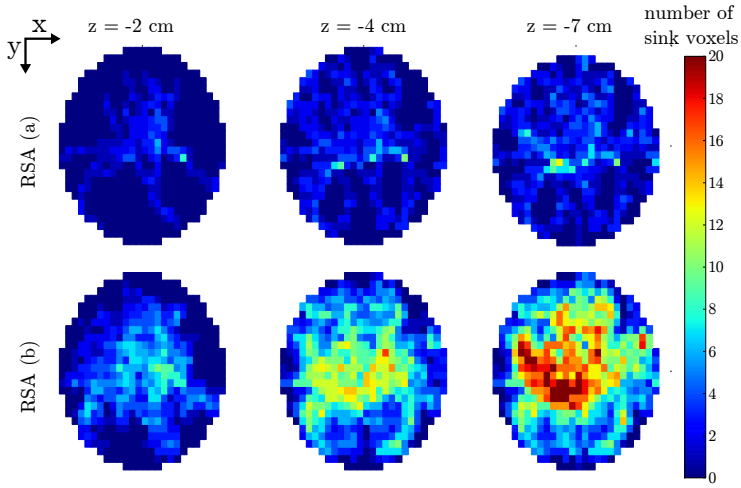

Figure 5.15: Simulated horizontal cumulative water sink pattern for the RSAs (a) and (b) and for the depths −2, −4 and −7 cm

The simulated water sink term distributions lead already to first estimations of the solute behavior in the simulation. The equilibrium concentration level of the BTCs is directly related to the cumulative water uptake by the plant in the soil volume between the top boundary and the depth where the BTC is measured when no solute is taken up by the roots [Schröder et al., 2012]. As a consequence, the concentration levels of the scenarios with RSA (b) are higher compared to the scenarios with the RSA (a) and differ also between the scenarios, especially between (A,B) compared to (C,D). In contrast, the basic RSA (a) does not cause very different BTC concentration plateaus since the 1D profile of water uptake distribution is very similar (Figure 5.14).

The importance of the location of root water uptake and the root conductivities, which define the local root water amount, on the solute distribution patten can be extracted from Figure 5.15, where the sink term is calculated as a cumulative number for the different depths −2, −4 and −7 cm. For these depths, the sink voxels are summed up from the top to the defined depth, and thus indicate how much sink voxels are located

above until this depth. The solute "'shadow"' effect, which occurs due to root water uptake on upper locations, is therefore also included in theses patterns.

If the concentration distribution is only linked to the location of root water uptake, and thus to the root architecture, the obtained sink number pattern of Figure 5.15 could be perfectly linked to the concentration pattern from Figure 5.11 and Figure 5.12. However, the concentration pattern show variations between the different scenarios with varied root conductivities and the sink number pattern can not be linked to any specific scenario. This shows the large influence of the local root water uptake amount, which is linked to the axial and radial root conductivities. However, the higher tracer concentration occurs mostly where the most horizontal, cumulative sink terms are located.

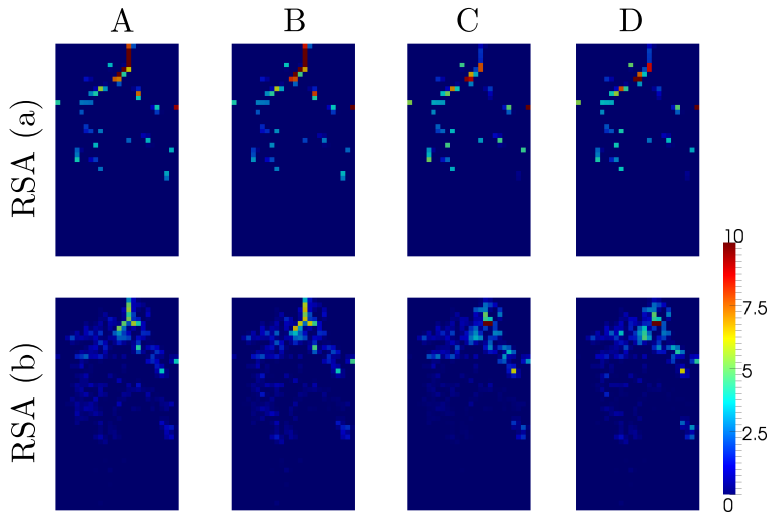

Figure 5.16: Two-dimensional x-z-slices of the simulated water sink term distribution [d^{-1}] for the RSA (a) and (b) and all scenarios (A,B,C,D) at day 2; no change afterwards due to a quasi steady-state water flow

The distribution of the water sink terms in a vertical slice is shown in Figure 5.16 (same location as in Figure 5.10). The spatial locations of root water uptake are similar for each RSA, which is expected since the root water uptake is directly linked to the plant root architecture. The RSA (b) creates more water sink voxels due to its additional finer roots, but the pattern obtained by the basic RSA (a) can also be recognized inside the pattern caused by RSA (b).

Although the locations of the sink terms are similar for each RSA, the amount of root water uptake at a certain location depends on the hydraulic parameters of the plant roots. The scenarios A and B cause similar water uptake amounts at a given location for the same RSA. The same is true for the scenarios C and D. The connection between these scenarios is the radial conductivity, which is defined equally for the scenarios A and B as well as for the scenarios C and D. Thus, the spatial sink term distribution is much more sensitive to the radial conductivity as to the axial conductance [Javaux et al., 2008, Fig. 4].

However, the spatial concentration patterns do also vary between scenarios with equal radial conductivity (Figure 5.10). Hence, the concentration distribution is not only sensitive to radial but also to axial plant hydraulic parameters, even if this cannot be seen in the averaged 1D and spatial water sink terms. Matching the same concentration pattern of the MRI with the numerical model could therefore provide significant information about the plant hydraulic parameters and of the importance of the finer roots on root water uptake.

5.4 Discussion

The result show that the measured BTC can be obtained by the simulations. In addition, both RSAs show less variability in the 1D water sink term profiles within the different simulation runs and some similarities to the 1D sink profiles obtained by the MRI data. Considering the wide range of root conductance and and conductivities as and the two different RSAs in the simulations, as well as the noise in the MRI data, the root water uptake dynamic can be considered to be very close to the 1D sink term profiles obtained by the simulation tool.

However, the spatial solute pattern from the MRI images could not be obtained by any simulation scenario. For this mismatching between simulated and monitored cross-sectional data, several possibilities are conceivable and these hypotheses are discussed in the next section.

5.4.1 Physical processes

The main difference between the measured and simulated spatial concentration patterns is the high tracer accumulation at the left boundary area (Figure 5.9), which is seen in the MRI but not in the simulated data (Figure 5.10). One possibility to cause this accumulation could be a high water uptake at the left side by a root (branch) that is missed in the reconstructed RSA. An indication for this is that only in this area a pronounced solute shadow can be seen, which is usually observed where high water

uptake by roots takes place. However, this missing root must have been quite large to cause such high concentration values and should have caused a high signal when the RSA was measured. Missing this root during the manual reconstruction is therefore unlikely.

However, no signal would be obtained by the MRI if this root branch died before the RSA was measured. This would fit to the concentration distribution development after day 5, where the concentration is decreasing again with time in this soil part. By stopping root water uptake here, the tracer would be flushed out downwards. In this case, the dead root branch should at least been found in the soil column after digging out the RSA at the end of the experiment, which was not the case.

Another option is a heterogeneous water flow that directed the tracer into this area. This might have been possible due to packing artifacts of the sand, since a homogenous soil distribution can hardly be obtained in reality. Furthermore, heterogeneous irrigation could increase this effect. Covering the upper surface with a 3 mm thick layer of coarse sand should have prevented a heterogeneous irrigation through the pump driven drop system. This could have failed to distribute the irrigated water homogeneously. Though, this cannot explain why tracer enrichment is seen in this soil region as MRI is supposed to measure concentration in the water solution. Packing artifacts should be filtered out in the concentration images by dividing with the signal intensity S by the reference signal S_{ref}.

5.4.2 Model

The processes considered above can be described by the numerical model and should be tested by including them into the simulation setups. Nevertheless, processes might have occurred that cannot be simulated by this particular model. For example, the physical presence of the plant in the used model is not seen by the soil, only the water sink is considered. The assumption in the model definition is that the water sink term distribution is disturbing the velocity field in relation to the plant root architecture and thus physical barriers by the plant are negligible. In such a small plant-soil system as studied here, however, this might not be the case. We also considered that all the roots where alive and that the conductances remained constant. However, bio-chemical reactions between plant roots and tracer Gd-DPTA^{2-} might arise. This could influence the tracer behavior. The negative charge of Gd-DPTA^{2-} should prevent adsorption at the soil matrix [Haber-Pohlmeier et al., 2010], but the interaction between Gd-DPTA^{2-} and plant roots, in particular in the rhizosphere, is not clear and needs further investigation.

5.4.3 MRI data

Finally, the obtained MRI data has to be questioned. The calibration curve in Figure 5.2 links the MRI signals S/S_{ref} to concentration values. This calibration curve is nonlinear and an increase of signal intensity to higher concentration values is only assured to concentration values of $4 - 5$ μmol cm^{-3}. The simulation results show that local concentration values larger than 5 μmol cm^{-3} can be easily obtained in such a coupled soil-plant system. These spots of high concentrations would have caused the same S/S_{ref} values and thus are not related to higher concentrations. This cannot explain why the measured concentration decreases with depth, as seen in the depth-averaged concentration profiles (Figure 5.13) and also in the 2D concentration slices obtained by MRI (Figure 5.9). This decrease cannot be explained by any physical process.

To obtain also information about the early days of the measurement, one should consider using the tracer sensitive data S of the MRI measurements only. This data is available for all measurement days and therefore might provide important information of the tracer behavior and its breakthrough in the first days. To this end, the concentration dependencies of the MRI signal has to be decoupled from the S_{ref} data, describing the maximum signal intensity. Using the difference between S data only, by subtracting one S data set by the S data from the day before, or by subtracting all temporal S data sets by the one form day 0, one might obtain further useful information.

5.5 Summary, conclusion and outlook

In this study, we compared monitored tracer movement in a planted soil by MRI with simulation results of a 3D high-resolution model. The chosen model is an extended version of R-SWMS [Javaux et al., 2008] describing water flow in soil and roots, and coupled to a particle tracking algorithm that solves the CDE. The experimental data were obtained by MRI, monitoring Gd-DTPA^{2-} over nine days and the root architecture at the middle of the measurement period.

By manual reconstruction of the measured RSA of the lupine plant, a basic root structure was obtained. In addition, a second RSA containing also virtually added smaller roots was created. Both RSAs were compared in various simulation runs. It was shown, that the measured outlet BTC matched all simulated BTCs well. By using different plant hydraulic parameters and the two different RSAs, various 3D solute patterns were created and it was shown that the spatial solute spreading is very sensitive to the RSA and its plant hydraulic parameters. However, these simulated patterns were very different from the measured MRI patterns. Several reasons for this were discussed above.

The high sensitivity of the spatial solute distribution to the root hydraulic parameters show the high potentials in these MRI experiments connected to the three-dimensional high-resolution model. If the concentration patterns from MRI could be matched by the simulation tool by estimating the right range of axial and radial conductances or conductivities, valuable information about the root water uptake behavior, the location of root water uptake, and the plant response of environmental effects affecting root water uptake could be obtained. An one-dimensional concentration profile could be used to obtain an one-dimensional water sink term profile and thus important information about the root water uptake distribution in the soil column.

In future work, the involved bio-physical processes have to be analyzed carefully from the data and missing aspects need to be implemented into the numerical model. However, as long as the uncertainty of the MRI data is unclear, a reliable interpretation of the MRI data is not possible and the numerical model cannot be improved. The data of the calibration linking concentration and MRI signal S/S_{ref} should be used for further noise analysis.

In addition, a new, simplified measurement setup could be defined and new MRI data obtained. Here, a lower input concentration should be used to enlarge the concentration range measurable by MRI. Using a younger root system with less root branches and a less moist soil, the root system could be obtained more clearly from the virtual reality. Finally, we suggest to stop the irrigation of the soil column after an equilibrium concentration is reached by the bottom BTC and measure the concentration distribution while the tracer movement is only dependent of the root water uptake and the water flow to the root. Therewith, downwards transport of the tracer by the irrigation is avoided and the solute shadow effects can me minimized because the solute accumulation depends mainly on the local tracer transport to the roots.

Chapter 6

General conclusion

The mutual effects of root water uptake and solute spreading are still under debate. Since these soil-root interactions are difficult to measure *in situ*, a wide selection of numerical models with different complexity are available. However, processes at the soil-root boundary, involving solutes, are often neglected or not explicitly defined, e.g. in 1D models. In this thesis, the model of Javaux et al. [2008] was extended by adding a stable and comprehensive solute transport module. With this extended version, soil-plant interactions considering water flow and solute transport on plant scale were analyzed in three different projects.

6.1 Summary

In Chapter 3, the impacts of root architecture, plant solute uptake mechanisms (passive, active and solute exclusion), and plant transpiration rate on the water flow field in the soil and on solute spreading were investigated. The simulation results showed that the apparent dispersivity length is affected by the heterogeneous flow field, caused by root water uptake. The apparent dispersivity length changed in a range of $\pm 50\%$, depending on solute redistribution in the root zone that depends on solute uptake type and soil dispersivity length. In addition, simulation results indicate that local concentration gradients within the root zone have an impact on apparent solute uptake rate parameters. These parameters are commonly used in 1D models to calculate uptake rates from spatially averaged concentrations. This shows the importance of small scale 3D water and solute fluxes induced by root water and nutrient uptake.

Contrary to the first study, the effect of solute concentrations on root water uptake was included in Chapter 4. Here, the concentration distribution was converted to osmotic heads and considered in the total water potential that drives the radial water flow into roots. After validation of the model by comparing simulated data with results form Hamza and Aylmore [1992], a suitable functional form of the uptake reduction function was identified. The simulations demonstrated that the local total water head

at the soil-root interface (e.g., the sum of the pressure and osmotic pressure heads), controls root water uptake, indicating that reduction functions cannot be factorized in terms that account for pressure and osmotic heads, respectively. It was shown that upscaling of the local to bulk water potential, which is mostly measured in experimental studies, leads to non-unique relations between root water uptake and upscaled water potential and explains the scatter observed in experimental response functions. This difference between bulk soil average and soil-root interface water potential is greater for combined salinity and matric potential stress and for low root length densities, because larger gradients of the matric potential lead to larger deviations between total soil water potential near roots and the bulk or upscaled water potential. Furthermore, the global stress response, which is integrated over time and the root-zone, was found to be different to the local response in time and (root zone) space. Comparing with global stress response functions, the results were in good agreement with the usually used empirical s-shaped function for salt stress [van Genuchten and Hoffman, 1984].

In the third study, we compared measured and simulated 3D data of a tracer experiment in a planted soil column. The data were obtained from by magnetic resonance imaging (MRI) and compared to simulation results from the numerical model. Using the simulation tool, the effects of root architecture, fine roots and root conductance on solute movement were investigated and the obtained one- and three-dimensional tracer concentrations were compared to the MRI data. The measured equilibrium concentration level of the outlet BTC, as well as of BTCs at other depth, calculated from the MRI data, could be obtained by the model. In addition, spatial concentration patterns were compared, but the MRI images of the concentration distribution could not be matched by the simulation tool. However, further work on the measured and simulated data can improve this matching, and by estimating the right range of axial and radial conductances or conductivities, valuable information about the root water uptake behavior, the location of root water uptake, and the plant response of environmental effect affection root water uptake could be obtained.

All three projects show the wide capabilities of the detailed numerical model that was developed and used in this thesis. Applying this model to several individual solute-related problems, the obtained results brings us one step closer understanding the complex interplay of plants and soil solute processes.

6.2 Perspectives

In Chapter 3, the impact of plant roots on solute dispersivity length was analyzed. This results should confirmed by comparing the virtual data with BTCs obtained by similar experimental setups. These experiments can show if the same impact on apparent

dispersivity length due to plant roots can be received. Furthermore, different horizontal root length densities, caused by increasing and decreasing the soil domain but with the same root structure, can be investigated. Also, simulations with similar plants, but different potential transpiration rates that create a heterogeneous water uptake, will point out important effects on solute movements in soil.

In all simulation setups used, the soil was defined as homogeneous. In further studies, the virtual experiments should be extended to simulations in heterogeneous soil. Soil heterogeneity plays an important role and its impact on flow field heterogeneity and the magnitude and scale dependency of the apparent dispersivity have been investigated intensively (see for instance, Vanderborght et al. [2006]). The additional effect of plants roots has to be analyzed. The effects of root water and nutrient uptake and soil heterogeneity on apparent dispersivity are not expected to be additive since complex interactions between root water uptake and the spatially variable water contents and water fluxes in a heterogeneous soil are plausible. For example, the velocity and solute distribution would be dependent also by the plant response on heterogeneous soil (e.g., by compensated root water uptake due to faster drying areas [Kuhlmann et al., 2012]).

The simulations in Chapter 4 focused on salt accumulation around plant roots and the plant response due to saline stress. Future work should focus on sensitivity analyses on the parameters affecting the shift in the water potential between bulk and soil-root interface by using 1D apparent data. The parametrization of these functions could be investigated by inverse modeling, using measurement data of irrigation experiments with saline water. In addition, the simulation setups in Chapter 4 did not consider solute uptake. Though, some salts are taken up by the plant roots and the amount of uptake and the solute uptake mechanisms have a different influence on the concentration distribution around the root system [Schröder et al., 2012]. In future work, the influence of root solute uptake on transpiration reduction should be investigated. In addition, no osmotic adjustment was assumed. Defining root hydraulic properties or a reflection coefficient σ dependent on total or osmotic soil potentials at the soil-root interface could be used to simulated stress related adjustment.

Comparing simulation results with measurement data is important for the development of numerical models. Therefore, the continuing work of Chapter 5 should focus on improving simulated and measured transport results. Possible missing aspects and biophysical processes should be investigated, implemented into the numerical model and tested by additional simulation runs. In addition, the uncertainty of the MRI data has to be clarified, for example by using the calibration data set through improved experimental measurements for linking Gd concentration and MRI signal. Also, other tracers should be considered, for example deuterium oxide (D_2O), which can be measured by MRI [Pohlmeier et al., 2009] or (also inside the plant root) by neutron radiography [Zarebanadkouki et al., 2012].

As pointed out in this study, the processes at the soil-root interface are important to understand and investigate soil-plant interactions. Thus, a high resolution of the soil grid is necessary. The drawback is an usually long simulation time. Schröder et al. [2009b] introduced an *a priori* grid refinement based on the root system architecture and showed the same accuracy compared to a regular fine grid, but with less computational time. This approach was applied for water flow and root water uptake only, but could be extended to be used for solute transport and uptake.

Appendix A

Standard error for fitted apparent dispersivity length λ_{app}

Table A.1: Apparent dispersivity length (in cm) fitted with Hydrus 1D with steady-state and transient transpiration rate, and solute exclusion; plant: fibrous

$T_{pot} = 0.5$ cm d^{-1}	0,const	diurnal
$z = -10$ cm	1.033 ± 0.002 $R^2 = 0.99736$	1.467 ± 0.001 $R^2 = 0.99665$
$z = -20$ cm	1.283 ± 0.001 $R^2 = 0.99836$	1.474 ± 0.001 $R^2 = 0.97555$
$z = -40$ cm	1.449 ± 0.001 $R^2 = 0.99934$	1.368 ± 0.001 $R^2 = 0.94804$

Table A.2: Apparent dispersivity length (in cm) fitted with Hydrus 1D with steady-state and transient transpiration rate, and solute exclusion; plant: tap-rooted

$T_{pot} = 0.5$ cm d^{-1}	const	diurnal
$z = -10$ cm	1.546 ± 0.001 $R^2 = 0.99817$	1.223 ± 0.001 $R^2 = 0.98362$
$z = -20$ cm	1.333 ± 0.001 $R^2 = 0.99892$	1.372 ± 0.001 $R^2 = 0.98973$
$z = -40$ cm	1.325 ± 0.001 $R^2 = 0.99924$	1.342 ± 0.001 $R^2 = 0.98906$

Table A.3: Apparent dispersivity length (in cm) fitted with Hydrus 1D under steady-state conditions for solute exclusion, active and passive solute uptake; transpiration rate $T_{pot} = 0.5$ cm d^{-1}; plant: fibrous

Type	Exclusion	Passive	Active
-10 cm	1.033 ± 0.002 $R^2 = 0.99681$	1.374 ± 0.002 $R^2 = 0.99736$	0.920 ± 0.002 $R^2 = 0.99005$
-20 cm	1.283 ± 0.001 $R^2 = 0.99902$	1.147 ± 0.048 $R^2 = 0.99836$	0.559 ± 0.014 $R^2 = 0.99278$
-40 cm	1.449 ± 0.001 $R^2 = 0.99885$	1.084 ± 0.000 $R^2 = 0.99934$	0.853 ± 0.001 $R^2 = 0.99700$

Table A.4: Apparent dispersivity length (in cm) fitted with Hydrus 1D under steady-state conditions for solute exclusion, active and passive solute uptake; transpiration rate $T_{pot} = 0.5$ cm d^{-1}; plant: taprooted

Type	Exclusion	Passive	Active
-10 cm	1.456 ± 0.001 $R^2 = 0.99817$	1.219 ± 0.001 $R^2 = 0.99730$	1.207 ± 0.002 $R^2 = 0.99552$
-20 cm	1.333 ± 0.001 $R^2 = 0.99892$	1.058 ± 0.000 $R^2 = 0.99863$	0.982 ± 0.001 $R^2 = 0.99742$
-40 cm	1.325 ± 0.001 $R^2 = 0.99924$	1.024 ± 0.000 $R^2 = 0.99943$	0.628 ± 0.001 $R^2 = 0.99892$

Table A.5: Apparent dispersivity length (in cm) fitted with Hydrus 1D under steady-state conditions; solute exclusion with three transpiration rates; plant: fibrous

T_{pot}	0.25 cm d^{-1}	0.5 cm d^{-1}	0.667 cm d^{-1}
-10 cm	1.090 ± 0.001 $R^2 = 0.99865$	1.033 ± 0.002 $R^2 = 0.99681$	1.195 ± 0.002 $R^2 = 0.99673$
-20 cm	1.191 ± 0.001 $R^2 = 0.99937$	1.283 ± 0.001 $R^2 = 0.99902$	1.417 ± 0.002 $R^2 = 0.99836$
-40 cm	1.188 ± 0.000 $R^2 = 0.99963$	1.449 ± 0.001 $R^2 = 0.99885$	1.672 ± 0.001 $R^2 = 0.99746$

Table A.6: Apparent dispersivity length (in cm) fitted with Hydrus 1D under steady-state conditions; passive solute uptake, with three transpiration rates; plant: taprooted

T_{pot}	0.25 cm d^{-1}	0.5 cm d^{-1}	0.667 cm d^{-1}
-10 cm	1.190 ± 0.001 $R^2 = 0.99848$	1.456 ± 0.001 $R^2 = 0.99736$	1.830 ± 0.004 $R^2 = 0.99560$
-20 cm	1.180 ± 0.001 $R^2 = 0.99920$	1.333 ± 0.001 $R^2 = 0.99836$	1.525 ± 0.001 $R^2 = 0.99675$
-40 cm	1.160 ± 0.000 $R^2 = 0.99962$	1.325 ± 0.001 $R^2 = 0.99934$	1.507 ± 0.001 $R^2 = 0.99866$

Acknowledgement

Though only my name appears on the cover of this thesis, many people have contributed to its production. I owe my gratitude to all those people who have made this dissertation possible.

This thesis is a result of the cooperation between Jülich Supercomputing Center (JSC) and the Institute of Bio- and Geoscience 3 (IBG-3, Agrosphere) of the Forschungszentrum Jülich GmbH. The main subject of this thesis, investigating and modeling root-soil interaction, is a strong expertise at the Agrosphere Institute, while JSC was providing valuable support in computational and mathematical questions. I would like to thank the directors of IBG-3 and JSC, Prof. H. Vereecken and Prof. T. Lippert, for making this project possible.

During the last years, I have had the support and encouragement of my supervisor Prof. M. Javaux, who taught me to 'think like a plant'. Our discussions were always guiding, inspiring and motivating and helped me to overcome all the obstacles in the completion of this research work.

A special thanks has also to be addressed to Prof. J. Vanderborght for the illuminating discussions and a lot of help at all fronts of my thesis. His constructive comments and patient explanations made enormous contribution to this work.

I want to thank the head of the math department Prof. J. Grotendorst and my supervisor within the math department Dr. B. Steffen for their support over the last three years.

I have greatly benefited from my stay in Israel, where I received support and enthusiasm from Prof. N. Lazarovitch. Also, I'm very thankful to Prof. H. Vereecken for making these three months abroad possible.

Colleagues and friends (at work) brought lots of fun, help and support in my everyday research life. Thanks go here to the 'Academic Powerhouse' of the JSC: Benedikt, Christina, Ivo, Mathias, Robert, Sonja and Stefan, and to my 'girls' from the IBG-3: Anja, Daniela, Laura, Maria, Markus, Katrin, Katrina, Sonja, and Sebastian. Thanks, Katrin, for our running-root-discussions and for pushing my social activity, Anja, for cooking-evenings and entertaining conferences, and Daniela, for the 'Tschaka'-motivation.

Special thanks to my office-husband Mathias, who fought a large number of compiler, algorithms and indices battles with and for me, and made our office time as enjoyable, funny and challenging as only a physicist could do. Another special thanks to Robert, whose friendship and encouragement shaped by daily conversations and/or chocolate I will miss so much.

I thank my family for being there for me over all the years in every possible way, especially my sister, who showed me the possibilities in the world of research.

And Bo, for his patience, support and love.

Bibliography

Assenmacher, I. and Kuhlen, T. (2010). The ViSTA Virtual Reality Toolkit.

Bathe, K. (2001). *Finite-Elemente-Methoden (German Edition)*. Springer.

Bear, J. (1972). *Dynamics of Fluids in Porous Media*. Dover Pubn Inc.

Bechtold, M., Haber-Pohlmeier, S., Vanderborght, J., Pohlmeier, A., Ferré, T. P. a., and Vereecken, H. (2011a). Near-surface solute redistribution during evaporation. *Geophysical Research Letters*, 38:L17404.

Bechtold, M., Vanderborght, J., Ippisch, O., and Vereecken, H. (2011b). Efficient random walk particle tracking algorithm for advective-dispersive transport in media with discontinuous dispersion coefficients and water contents. *Water Resources Research*, 47:W10526.

Bechtold, M., Vanderborght, J., Weihermüller, L., Herbst, M., Günther, T., Ippisch, O., Kasteel, R., and Vereecken, H. (2012). Upward Transport in a Three-Dimensional Heterogeneous Laboratory Soil under Evaporation Conditions. *Vadose Zone Journal*, 11(2).

Cardon, G. and Letey, J. (1992). Plant water uptake terms evaluated for soil water and solute movement models. *Soil Science Society of America Journal*, 32:1876–1880.

Couvreur, V., Vanderborght, J., and Javaux, M. (2012). A simple three-dimensional macroscopic root water uptake model based on the hydraulic architecture approach. *Hydrology and Earth System Sciences*, 16:2957–2971.

Darcy, H. (1856). *Les fontaines publiques de la ville de Dijon.* Dalmont, Paris.

de Jong van Lier, Q., Metselaar, K., and van Dam, J. C. (2006). Root Water Extraction and Limiting Soil Hydraulic Conditions Estimated by Numerical Simulation. *Vadose Zone Journal*, 5:1264–1277.

de Jong van Lier, Q., van Dam, J. C., and Metselaar, K. (2009). Root Water Extraction under Combined Water and Osmotic Stress. *Soil Science Society of America Journal*, 73:862–875.

de Wilding, L. P. and van Noordwijk, M. (1994). Mass Flow and Diffusion of Nutrients to A Root With Constant or Zero-Sink Uptake II. Zero-Sink Uptake. *Soil Science*, 157(3):171–175.

de Wit, C. (1958). *Transpiration and crop yields*. PhD thesis, Universtity Wageningen.

Demidchik, V., Davenport, R. J., and Tester, M. (2002). Nonselective cation channels in plants. *Annual review of plant biology*, 53:67–107.

Dirksen, C., Kool, J. B., Koorevaar, P., and van Genuchten, M. T. (1993). HYSWASOR - Simulation Model of Hysteretic Water and Solute Transport in the Root ZoneNo Title. In *Water Flow and Solute Transport in Soils*, pages 99–122. Springer Berlin Heidelberg.

Doussan, C., Pagès, L., and Vercambre, G. (1998). Modelling of the hydraulic architecture of root systems: an integrated approach to water absorption - model description. *Annals of Botany*, 81:213–223.

Doussan, C., Pierret, A., Garrigues, E., and Pagès, L. (2006). Water Uptake by Plant Roots: II - Modelling of Water Transfer in the Soil Root-system with Explicit Account of Flow within the Root System - Comparison with Experiments. *Plant and Soil*, 283:99–117.

Draye, X., Kim, Y., Lobet, G., and Javaux, M. (2010). Model-assisted integration of physiological and environmental constraints affecting the dynamic and spatial patterns of root water uptake from soils. *Journal of experimental botany*, 61(8):2145–2155.

Dudley, L. M. and Shani, U. (2003). Modeling Plant Response to Drought and Salt Stress Reformulation of the Root-Sink Term. *Vadose Zone Journal*, 2:751–758.

Dunbabin, V. M., Diggle, A., and Rengel, Z. (2002). Simulation of field data by a basic three-dimensional model of interactive root growth. *Plant and soil*, 239:39–54.

Ehlers, W. (1996). *Wasser in Boden und Pflanze: Dynamik des wasserhaushalts als Grundlage von Pflanzenwachstum und Ertrag*. Eugen Ulmer, Stuttgart.

Esser, H. G., Carminati, A., Vontobel, P., Lehmann, E. H., and Oswald, S. E. (2010). Neutron radiography and tomography of water distribution in the root zone. *Journal of Plant Nutrition and Soil Science*, 173:757–764.

Feddes, R., Kowalik, P., Kolinska-Malinka, K., and Zaradny, H. (1976). Simulation of field water uptake by plants using a soil water dependent root extraction function. *Journal of Hydrology*, 31:13–26.

Feddes, R., Kowalik, P., and Zaradny, H. (1978). *Simulation of field water use and crop yield*. Halsted Press.

Feddes, R. and Raats, P. (2004). Parameterizing the soil-water-plant root system. In *Unsaturated-zone modeling: progress, challenges and applications*, pages 95–141.

Fick, A. (1855). Ueber diffusion. *Annalen der Physik*, 94:59–86.

Gallardo, M., Eastham, J., Gregory, P. J., and Turner, N. C. (1996). A comparison of plant hydraulic conductances in wheat and lupins. *Journal of experimental botany*, 47(295):233–239.

Gardner, W. (1960). Dynamic aspects of water availability to plants. *Soil Science*, 89(2):63–73.

Gish, T. and Jury, W. (1983). Effect of plant roots and root channels on solute transport. *Transactions of the ASAE*, pages 440–444.

Green, S. R., Kirkham, M., and Clothier, B. E. (2006). Root uptake and transpiration: From measurements and models to sustainable irrigation. *Agricultural Water Management*, 86:165–176.

Gregory, P. (2006). *Plant roots. Growth, activity and interaction with soils.* Blackwell Publishing Ltd.

Groenveld, T., Ben-Gal, A., Yermiyahu, U., and Lazarovitch, N. (2013). Climate determined relative sensitivity of plants to salinity: quantification and simulation. *Vadose Zone Journal in press.*

Haber-Pohlmeier, S., Bechtold, M., Stapf, S., and Pohlmeier, A. (2010). Water Flow Monitored by Tracer Transport in Natural Porous Media Using Magnetic Resonance Imaging. *Vadose Zone Journal*, 9:835–845.

Hainsworth, J. and Aylmore, L. (1986). Water extraction by single plant roots. *Soil Science Society of America Journal*, 50:841–848.

Hammel, K., Gross, J., Wessolek, G., and Roth, K. (1999). Two-dimensional simulation of bromide transport in a heterogeneous field soil with transient unsaturated flow. *European journal of soil science*, 50:633–647.

Hamza, M. and Aylmore, L. (1992). Soil solute concentration and water uptake by single lupin and radish plant roots. *Plant and soil*, 145:187–196.

Hillel, D. (2003). *Introduction to environmental soil physics.* Elsevier Academic Press.

Homaee, M., Dirksen, C., and Feddes, R. a. (2002a). Simulation of root water uptake: I. Non-uniform transient salinity using different macroscopic reduction functions. *Agricultural Water Management*, 57:89–109.

Homaee, M., Feddes, R., and Dirksen, C. (2002b). Simulation of root water uptake: III. Non-uniform transient combined salinity and water stress. *Agricultural water management*, 57:127–144.

Homaee, M., Feddes, R. a., and Dirksen, C. (2002c). A macroscopic water extraction model for nonuniform transient salinity and water stress. *Soil Science Society of America Journal*, 66:1764–1772.

Hopmans, J. and Bristow, K. (2002). Current capabilities and future needs of root water and nutrient uptake modeling. *Advances in Agronomy*, 77:104–175.

Jarvis, N. J. (2011). Simple physics-based models of compensatory plant water uptake: concepts and eco-hydrological consequences. *Hydrology and Earth System Sciences*, 15:3431–3446.

Javaux, M., Draye, X., Doussan, C., Vanderborght, J., and Vereecken, H. (2011). Root water uptake: towards 3-D functional approaches. In Glinski, J., Horabik, J., and Lipiec, J., editors, *Encyclopaedia of Agrophysics*, pages 717–721.

Javaux, M., Schröder, T., Vanderborght, J., and Vereecken, H. (2008). Use of a Three-Dimensional Detailed Modeling Approach for Predicting Root Water Uptake. *Vadose Zone Journal*, 7(3):1079–1088.

Javaux, M., Vanderborght, J., Kasteel, R., and Vanclooster, M. (2006). Three-Dimensional Modeling of the Scale- and Flow Rate-Dependency of Dispersion in a Heterogeneous Unsaturated Sandy Monolith. *Vadose Zone Journal*, 5:515–528.

Jury, W., Fluhler, H., and Stolzy, L. (1977). Influence of soil properties, leaching fraction, and plant water uptake on solute concentration distribution. *Water Resources Research*, 13(3):645–650.

Jury, W., Gardner, W., Saffigna, P., and Tanner, C. (1976). Model for predicting simultaneous movement of nitrate and water through a loamy sand. *Soil Science*, 122(1):36–43.

Kasteel, R., Pütz, T., Vanderborght, J., and Vereecken, H. (2009). Solute Spreading under Transient Conditions in a Field Soil. *Vadose Zone Journal*, 8:690–702.

Knipfer, T. and Fricke, W. (2010). Root pressure and a solute reflection coefficient close to unity exclude a purely apoplastic pathway of radial water transport in barley (Hordeum vulgare). *The New phytologist*, 187:159–170.

Kochian, L. and Lucas, W. (1982). Potassium transport in corn roots I. Resolution of kinetics into a saturable and linear component. *Plant Physiology*, 70:1723–1731.

Kreft, A. and Zuber, A. (1978). On the physical meaning of the dispersion equation and its solutions for different initial and boundary conditions. *Chemical Engineering Science*, 33:1471–1480.

Kroes, J., van Dam, J., Groenendijk, P., Hendriks, R., and Jacobs, C. (2008). SWAP version 3.2. Theory description and user manual. Technical report.

Kuhlmann, A., Neuweiler, I., van der Zee, S. E. a. T. M., and Helmig, R. (2012). Influence of soil structure and root water uptake strategy on unsaturated flow in heterogeneous media. *Water Resources Research*, 48:W02534.

LaBolle, E. M., Quastel, J., and Fogg, G. E. (1998). Diffusion theory for transport in porous media: Transitionprobability densities of diffusion processes correspondig to advection-dispersion equations. *Water Resources Research*, 34(7):1685–1693.

Lichtner, P. C., Kelkar, S., and Robinson, B. (2002). New form of dispersion tensor for axisymmetric porous media with implementation in particle tracking. *Water Resources Research*, 38(8):1146.

Maas, E. and Hoffman, G. (1977). Crop Salt Tolerance -Current Assessment. *Journal of the Irrigation and Drainage Devision*.

Mairhofer, S., Zappala, S., Tracy, S. R., Sturrock, C., Bennett, M., Mooney, S. J., and Pridmore, T. (2012). RooTrak: automated recovery of three-dimensional plant root architecture in soil from x-ray microcomputed tomography images using visual tracking. *Plant physiology*, 158:561–569.

Metselaar, K. and de Jong van Lier, Q. (2007). The Shape of the Transpiration Reduction Function under Plant Water Stress. *Vadose Zone Journal*, 6:124–139.

Millington, R. and Quirk, J. (1961). Permeability of porous solids. *Transactions of the Faraday Society*.

Nassar, I. N. and Horton, R. (1997). Heat , Water , and Solute Transfer in Unsaturated Porous Media : I - Theory Development and Transport Coefficient Evaluation. *Transport in Porous Media*, 27:17–38.

Nimah, M. N. and Hanks, R. J. (1973). Model for estimating soil water, plant, and atmospheric interrelations: I. Description and sensitivity. *Soil Science Society of America Journal*, pages 522–527.

Pagès, L., Vercambre, G., and Drouet, J. (2004). Root Typ: a generic model to depict and analyse the root system architecture. *Plant and Soil*, 258:103–119.

Parker, J. and van Genuchten, M. (1984). Flux-averaged and volume-averaged concentrations in continuum approaches to solute transport. *Water Resour. Res*, 20(7):866–872.

Pitman, M. G. and Läuchli, A. (2004). Global Impact of Salinity and Agricultural Ecosystems. In Läuchli, A. and Lüttge, U., editors, *Salinity: Environment - Plants - Molecules*, chapter 1, pages 3–20. Springer Netherlands.

Pohlmeier, A., Javaux, M., Vereecken, H., and Haber-Pohlmeier, S. (2013). Magnetic Resonance Imaging Techniques for Visualization of Root Growth and Root Water Uptake Processes. In Anderson, S. H. and Hopmans, J. W., editors, *Soil-Water-Root Processes:Advances in Tomography and Imaging*, pages 137–156. The Soil Science Society of America, Inc.

Pohlmeier, A., Oros-Peusquens, A., Javaux, M., Menzel, M., Vanderborght, J., Kaffanke, J., Romanzetti, S., Lindenmair, J., Vereecken, H., and Shah, N. J. (2008). Changes in soil water content resulting from Ricinus root uptake monitored by magnetic resonance imaging. *Vadose Zone Journal*, 7(3):1010–1017.

Pohlmeier, A., van Dusschoten, D., Weihermüller, L., Schurr, U., and Vereecken, H. (2009). Imaging water fluxes in porous media by magnetic resonance imaging using D2O as a tracer. *Magnetic resonance imaging*, 27:285–292.

Porporato, A., D'Odorico, P., Laio, F., and Rodriguez-Iturbe, I. (2003). Hydrologic controls on soil carbon and nitrogen cycles. I. Modeling scheme. *Advances in Water Resources*, 26:45–58.

Radcliffe, D. E. and Simunek, J. (2010). *Soil Physics With Hydrus: Modeling and Applications*. Water science technology and engineering. Taylor & Francis Group.

Rausch, R., Schäfer, W., Therrien, R., and Wagner, C. (2005). *Solute Transport Modelling*. Schweizerbart'sche Verlagsbuchhandlung, Stuttgart.

Richards, L. A. (1931). Capillary Conduction of Liquids Through Porous Mediums. *Physics*, 1(5):318.

Roose, T. and Kirk, G. J. D. (2009). The solution of convection diffusion equations for solute transport to plant roots. *Plant and Soil*, 316:257–264.

Russo, D., Zaidel, J., Fiori, A., and Laufer, A. (2006). Numerical analysis of flow and transport from a multiple-source system in a partially saturated heterogeneous soil under cropped conditions. *Water Resources Research*, 42:W06415.

Russo, D., Zaidel, J., and Laufer, A. (1998). Numerical analysis of flow and transport in a three-dimensional partially saturated heterogeneous soil. *Water resources research*, 34(6):1451–1468.

Russo, D., Zaidel, J., and Laufer, A. (2004). Numerical Analysis of Transport of Interacting Solutes in a Three-Dimensional Unsaturated Heterogeneous Soil. *Vadose Zone Journal*, 3:1286–1299.

Salamon, P., Fernàndez-Garcia, D., and Gómez-Hernández, J. J. (2006). A review and numerical assessment of the random walk particle tracking method. *Journal of contaminant hydrology*, 87:277–305.

Schneider, C. L., Attinger, S., Delfs, J.-O., and Hildebrandt, A. (2010). Implementing small scale processes at the soil-plant interface - the role of root architectures for calculating root water uptake profiles. *Hydrology and Earth System Sciences*, 14:279–289.

Schröder, N., Javaux, M., Vanderborght, J., Steffen, B., and Vereecken, H. (2012). Effect of Root Water and Solute Uptake on Apparent Soil Dispersivity: A Simulation Study. *Vadose Zone Journal*, 11.

Schröder, T., Javaux, M., Vanderborght, J., Körfgen, B., and Vereecken, H. (2008). Effect of Local Soil Hydraulic Conductivity Drop Using a Three-Dimensional Root Water Uptake Model. *Vadose Zone Journal*, 7:1089–1098.

Schröder, T., Javaux, M., Vanderborght, J., Körfgen, B., and Vereecken, H. (2009a). Implementation of a Microscopic Soil-Root Hydraulic Conductivity Drop Function in a Three-Dimensional Soil-Root Architecture Water Transfer Model. *Vadose Zone Journal*, 8:783–792.

Schröder, T., Tang, L., Javaux, M., Vanderborght, J., Körfgen, B., and Vereecken, H. (2009b). A grid refinement approach for a three-dimensional soil-root water transfer model. *Water Resources Research*, 45:W10412.

Shani, U. and Ben-Gal, A. (2005). Long-term response of grapevines to salinity: osmotic effects and ion toxicity. *American journal of enology and viticulture*, 52:148–154.

Shani, U., Ben-Gal, A., Tripler, E., and Dudley, L. M. (2007). Plant response to the soil environment: An analytical model integrating yield, water, soil type, and salinity. *Water Resources Research*, 43:W08418.

Shiklomanov, I. (1993). *World fresh water resources*. Oxford University Press [for] Pacific Institute in Development, Environment, and Security [and] Stockholm Environment Institute.

Siebert, S., Burke, J., Faures, J. M., Frenken, K., Hoogeveen, J., Döll, P., and Portmann, F. T. (2010). Groundwater use for irrigation - a global inventory. *Hydrology and Earth System Sciences*, 14(10):1863–1880.

Simunek, J., Genuchten, M. V., and Sejna, M. (2005). The HYDRUS-1D software package for simulating the one-dimensional movement of water, heat, and multiple solutes in variably-saturated media. Technical Report April.

Simunek, J. and Hopmans, J. W. (2009). Modeling compensated root water and nutrient uptake. *Ecological Modelling*, 220:505–521.

Simunek, J., Huang, K., and van Genuchten, M. T. (1995). The SWMS_3D code for simulating water flow and solute transport in three-dimensional variably-saturated media. Technical report.

Skaggs, T. H., Shouse, P. J., and Poss, J. A. (2006a). Irrigating Forage Crops with Saline Waters. *Vadose Zone Journal*, 5:824–837.

Skaggs, T. H., van Genuchten, M. T., Shouse, P. J., and Poss, J. a. (2006b). Macroscopic approaches to root water uptake as a function of water and salinity stress. *Agricultural Water Management*, 86:140–149.

Somma, F., Hopmans, J. W., and Clausnitzer, V. (1998). Transient three-dimensional modeling of soil water and solute transport with simultaneous root growth, root water and nutrient uptake. *Plant and Soil*, 202:281–293.

Steudle, E. (2000). Water uptake by roots: effects of water deficit. *Journal of experimental botany*, 51(350):1531–1542.

Stingaciu, L. R., Schulz, H., Pohlmeier, A., Behnke, S., Zilken, H., Vereecken, H., and Javaux, M. (2013). In Situ Root System Architecture Extraction from Magnetic Resonance Imaging for Application to Water Uptake Modeling. *Vadose Zone Journal*.

Taiz, L. and Zeiger, E. (2002). *Plant Physiology*. Sinauer Associates, Inc., Publishers, Sunderland, Massachusetts, 3 edition.

Tardieu, F. (1996). Drought perception by plants Do cells of droughted plants experience water stress? *Plant Growth Regulation*, 20:93–104.

Tompson, A. F. B. and Gelhar, L. (1990). Numerical simulation of solute transport in three-dimensional, randomly heterogeneous porous media. *Water Resources Research*, 26(10):2541–2562.

van Genuchten, M. (1980). A closed-form equation for predicting the hydraulic conductivity of unsaturated soils. *Soil Science Society of America Journal*, 8:892–898.

van Genuchten, M. (1987). *A numerical model for water and solute movement in and below the root zone*. United States Department of Agriculture Agricultural Research Service U.S. Salinity Laboratory.

van Genuchten, M. and Hoffman, G. (1984). Analysis of crop salt tolerance data. In *Soil Salinity under Irrigation. Processen and Management*, volume 51, chapter 8, pages 251–271. Springer Verlag, New York.

van Genuchten, M., Leij, F., and Yates, S. (1991). The RETC code for quantifying the hydraulic functions of unsaturated soils. Technical Report December.

Vanderborght, J., Kasteel, R., Herbst, M., Javaux, M., Thiery, D., Vanclooster, M., Mouvet, C., and Vereecken, H. (2005). A Set of Analytical Benchmarks to Test Numerical Models of Flow and Transport in Soils. *Vadose Zone Journal*, 4:206–221.

Vanderborght, J., Kasteel, R., and Vereecken, H. (2006). Stochastic Continuum Transport Equations for Field-Scale Solute Transport. *Vadose Zone Journal*, 5:184–203.

Vanderborght, J., Mallants, D., and Feyen, J. (1998). Solute transport in a heterogeneous soil for boundary and initial conditions: Evaluation of first-order approximations. *Water resources research*, 34(12):3255–3270.

Vanderborght, J. and Vereecken, H. (2007). Review of Dispersivities for Transport Modeling in Soils. *Vadose Zone Journal*, 6:29–52.

Vaughan, J. and Griffiths, J. (2012). *RF Coils for MRI*. John Wiley & Sons Inc, 1 edition.

Vereecken, H., Kamai, T., Harter, T., Kasteel, R., Hopmans, J. W., and Vanderborght, J. (2007). Explaining soil moisture variability as a function of mean soil moisture: A stochastic unsaturated flow perspective. *Geophysical Research Letters*, 34(L22402):1–6.

Vogeler, I., Green, S. R., Scotter, D., and Clothier, B. E. (2001). Measuring and modelling the transport and root uptake of chemicals in the unsaturated zone. *Plant and soil*, 231:161–174.

Wienke, S. (2009). *Entwicklung einer Software zur Bestimmung morphologischer Informationen von Wurzelsystemen mit Virtual Reality Techniken Masterarbeit*. PhD thesis, Fachhochschule Aachen.

Yang, J., Zhang, R., Wu, J., and Allen, M. B. (1996). Stochastic Analysis of Adsorbing Solute Transport in Two-Dimensional Unsaturated Soils. *Water Resources Research*, 32(9):2747–2756.

Yeo, A. and Flowers, T. (2007). *Plant Solute Transport*. Blackwell Publishing Ltd, Oxford, UK.

Zarebanadkouki, M., Kim, Y., Moradi, A., Vogel, H.-J., Kaestner, A., and Carminati, A. (2012). Quantification and Modeling of Local Root Water Uptake Using Neutron Radiography and Deuterated Water. *Vadose Zone Journal*, 11.

Schriften des Forschungszentrums Jülich
IAS Series

---

1. **Three-dimensional modelling of soil-plant interactions: Consistent coupling of soil and plant root systems**
   by T. Schröder (2009), VIII, 72 pages
   ISBN: 978-3-89336-576-0
   URN: urn:nbn:de:0001-00505

2. **Large-Scale Simulations of Error-Prone Quantum Computation Devices**
   by D. B. Trieu (2009), VI, 173 pages
   ISBN: 978-3-89336-601-9
   URN: urn:nbn:de:0001-00552

3. **NIC Symposium 2010**
   Proceedings, 24 – 25 February 2010 | Jülich, Germany
   edited by G. Münster, D. Wolf, M. Kremer (2010), V, 395 pages
   ISBN: 978-3-89336-606-4
   URN: urn:nbn:de:0001-2010020108

4. **Timestamp Synchronization of Concurrent Events**
   by D. Becker (2010), XVIII, 116 pages
   ISBN: 978-3-89336-625-5
   URN: urn:nbn:de:0001-2010051916

5. **UNICORE Summit 2010**
   Proceedings, 18 – 19 May 2010 | Jülich, Germany
   edited by A. Streit, M. Romberg, D. Mallmann (2010), iv, 123 pages
   ISBN: 978-3-89336-661-3
   URN: urn:nbn:de:0001-2010082304

6. **Fast Methods for Long-Range Interactions in Complex Systems**
   Lecture Notes, Summer School, 6 – 10 September 2010, Jülich, Germany
   edited by P. Gibbon, T. Lippert, G. Sutmann (2011), ii, 167 pages
   ISBN: 978-3-89336-714-6
   URN: urn:nbn:de:0001-2011051907

7. **Generalized Algebraic Kernels and Multipole Expansions for Massively Parallel Vortex Particle Methods**
   by R. Speck (2011), iv, 125 pages
   ISBN: 978-3-89336-733-7
   URN: urn:nbn:de:0001-2011083003

8. **From Computational Biophysics to Systems Biology (CBSB11)**
   Proceedings, 20 - 22 July 2011 | Jülich, Germany
   edited by P. Carloni, U. H. E. Hansmann, T. Lippert, J. H. Meinke, S. Mohanty, W. Nadler, O. Zimmermann (2011), v, 255 pages
   ISBN: 978-3-89336-748-1
   URN: urn:nbn:de:0001-2011112819

9. **UNICORE Summit 2011**
Proceedings, 7 - 8 July 2011 | Toruń, Poland
edited by M. Romberg, P. Bała, R. Müller-Pfefferkorn, D. Mallmann (2011), iv, 150 pages
ISBN: 978-3-89336-750-4
URN: urn:nbn:de:0001-2011120103

10. **Hierarchical Methods for Dynamics in Complex Molecular Systems**
Lecture Notes, IAS Winter School, 5 – 9 March 2012, Jülich, Germany
edited by J. Grotendorst, G. Sutmann, G. Gompper, D. Marx (2012), vi, 540 pages
ISBN: 978-3-89336-768-9
URN: urn:nbn:de:0001-2012020208

11. **Periodic Boundary Conditions and the Error-Controlled Fast Multipole Method**
by I. Kabadshow (2012), v, 126 pages
ISBN: 978-3-89336-770-2
URN: urn:nbn:de:0001-2012020810

12. **Capturing Parallel Performance Dynamics**
by Z. P. Szebenyi (2012), xxi, 192 pages
ISBN: 978-3-89336-798-6
URN: urn:nbn:de:0001-2012062204

13. **Validated force-based modeling of pedestrian dynamics**
by M. Chraibi (2012), xiv, 112 pages
ISBN: 978-3-89336-799-3
URN: urn:nbn:de:0001-2012062608

14. **Pedestrian fundamental diagrams: Comparative analysis of experiments in different geometries**
by J. Zhang (2012), xiii, 103 pages
ISBN: 978-3-89336-825-9
URN: urn:nbn:de:0001-2012102405

15. **UNICORE Summit 2012**
Proceedings, 30 - 31 May 2012 | Dresden, Germany
edited by V. Huber, R. Müller-Pfefferkorn, M. Romberg (2012), iv, 143 pages
ISBN: 978-3-89336-829-7
URN: urn:nbn:de:0001-2012111202

16. **Design and Applications of an Interoperability Reference Model for Production e-Science Infrastructures**
by M. Riedel (2013), x, 270 pages
ISBN: 978-3-89336-861-7
URN: urn:nbn:de:0001-2013031903

17. **Route Choice Modelling and Runtime Optimisation for Simulation of Building Evacuation**
by A. U. Kemloh Wagoum (2013), xviii, 122 pages
ISBN: 978-3-89336-865-5
URN: urn:nbn:de:0001-2013032608

18. **Dynamik von Personenströmen in Sportstadien**
by S. Burghardt (2013), xi, 115 pages
ISBN: 978-3-89336-879-2
URN: urn:nbn:de:0001-2013060504

19. **Multiscale Modelling Methods for Applications in Materials Science**
by I. Kondov, G. Sutmann (2013), 326 pages
ISBN: 978-3-89336-899-0
URN: urn:nbn:de:0001-20130902

20. **High-resolution Simulations of Strongly Coupled Coulomb Systems with a Parallel Tree Code**
by M. Winkel (2013), xvii, 196 pages
ISBN: 978-3-89336-901-0
URN: urn:nbn:de:0001-2013091802

21. **UNICORE Summit 2013**
Proceedings, 18th June 2013 | Leipzig, Germany
edited by V. Huber, R. Müller-Pfefferkorn, M. Romberg (2013), iii, 94 pages
ISBN: 978-3-89336-910-2
URN: urn:nbn:de:0001-2013102109

22. **Three-dimensional Solute Transport Modeling in Coupled Soil and Plant Root Systems**
by N. Schröder (2013), xii, 126 pages
ISBN: 978-3-89336-923-2
URN: urn:nbn:de:0001-2013112209

Many environmental and agricultural challenges rely on the proper understanding of water flow and solute transport in soils, for example the carbon cycle, crop growth, irrigation scheduling or fate of pollutants in subsoil. Current modeling approaches typically simulate plant uptake via empirical approaches, which neglect the three-dimensional (3D) root architecture. Yet, nowadays 3D soil-root water and solute models on plant-scale exist, which can be used for assessing the impact of root architecture and root and soil hydraulic resistances on the root uptake pattern and solute transport and water flow in soil. In this thesis, we used a numerical model, which offers the possibility to describe soil and root interaction processes in a mechanistic manner avoiding empirical descriptions of root water uptake as a function of averaged water potential and root length density. Water flow is simulated along water potential gradients in the soil-root continuum and the model accounts for solute movement and root solute uptake. Solute movement in soils is modeled with a particle tracking algorithm. With this model, three research questions are investigated. The first study investigates how root water uptake affects the velocity field, and thus the dispersivity length. The solute breakthrough curves from the three-dimensional results and different simulation setups were fitted with an equivalent one-dimensional flow and transport model. The obtained results of the apparent soil dispersivities show the effect of the plant roots on solute movement, and illustrate the relevance of small scale 3D water and solute fluxes, induced by root water and nutrient uptake. Second, we show how local matric and osmotic potentials affect root water uptake. We analyze the difference between upscaled time and root-zone integrated water potentials, as often measured in experimental studies, and local water potentials at the root-soil interface. In addition, we demonstrate the relation between the shape of local stress function and the global (time-integrated) plant stress response to salinity. The last part explores how water uptake could be deduced from tracer concentration distribution monitored in a soil-plant system by Magnetic Resonance Imaging (MRI). We show the effects of root system architecture, fine roots, and root conductance on solute and compare numerical and measured data. This shows the capabilities and limitations of both, the model prediction and the MRI measurement methodology. Furthermore, it points out the extensive effect of root architecture and its conductance parameters on solute spreading.

This publication was written at the Jülich Supercomputing Centre (JSC) which is an integral part of the Institute for Advanced Simulation (IAS). The IAS combines the Jülich simulation sciences and the supercomputer facility in one organizational unit. It includes those parts of the scientific institutes at Forschungszentrum Jülich which use simulation on supercomputers as their main research methodology.

IAS Series
Volume 22
ISBN 978-3-89336-923-2

JÜLICH
FORSCHUNGSZENTRUM